/
Article / Book Information

(　　)	
Title(English)	Centrifuge Modeling and Reliability Assessment of Liquefaction Mitigation Techniques for Shallow Foundations
(　　)	KUMARRITESH
Author(English)	Ritesh Kumar
(　　)	:　(　　), :　　　　, :　　11663　, :2020　9　25　, :　　　, :　　　,　　　,　　　,　　　,
Citation(English)	Degree:Doctor (Academic), Conferring organization: Tokyo Institute of Technology, Report number:　　11663　, Conferred date:2020/9/25, Degree Type:Course doctor, Examiner:,,,,
(　　)	
Type(English)	Doctoral Thesis

Centrifuge Modeling and Reliability Assessment of Liquefaction Mitigation Techniques for Shallow Foundations

Ritesh Kumar

DISSERTATION

Submitted in partial fulfillment of the requirements for the degree of

DOCTOR OF PHILOSOPHY

at

TOKYO INSTITUTE OF TECHNOLOGY

2020

Acknowledgements

I would like to express my sincere gratitude to my supervisor Professor Akihiro Takahashi for his continuous support and guidance. The door to Prof. Takahashi is always open whenever I have questions or obstacles. He consistently allowed me to expand the horizon in my way with great patience and steered me in the right direction whenever required. I could not ask for a better supervisor. I am also grateful for the critical insights he has put into my work, and the role he plays in this dissertation can never be overemphasized.

I am also grateful to the committee members Prof. Masaki Kitazume, Associate Prof. Jiro Takemura, Associate Prof. Kiyonobu Kasama, and Associate Prof. Shuji Tamura for their valuable suggestions and helpful comments.

I would like to extend my special thanks to our lab technician, Mr Sakae Seki, for his support and guidance during experiments. The successful completion of the experiments would not have been possible without his sincere efforts. I am also obliged to Assistant Prof. Kazuki Horikoshi for his great help on numerous occasions.

I would like to thank Assistant Prof. E. Ece Bayat (ITU, Turkey), Assistant Prof. Katerina Ziotopoulou (UC Davis, USA) and Senior Lecturer Gabriele Chiaro (UC, New Zealand) for providing me many learning opportunities. I would like to extend my special thanks to Prof. Ross W. Boulanger (UC Davis, USA) for supervising my PhD internship. Working with Ross was one of the best times of my student life. I admire him, and I hope that someday I would be able to command an audience as eloquently and effortlessly as he can.

I am indebted to the Ministry of Education, Culture, Sports, Science and Technology (MEXT), Japan for granting me a Monbukagakusho scholarship for graduate study. Thanks are due to Nippon Steel and Sumikin Engineering group as significant work presented in this dissertation is part of the collaborative research with them.

I would like to thank my parents for their love, guidance and moral support. I would also like to extend my special thanks to my brothers Rajneesh and Rohtash for always backing my side. Thanks are due to my all my labmates; especially, Jenisha, Partha, Max and Wang with whom I have shared moments of deep anxiety and excitement. A warm word for my best friends; Shweta and Mitali, who always managed to cheer me up. Last but not least, thanks are due to everyone for making my PhD journey a memorable one.

Abstract

Liquefaction has caused devastating damage to the built environment on shallow foundations such as settlement, tilting, and sinking all over the world during many past earthquakes. In current practice, soil remediation measures are requisite for liquefaction prone sites. Liquefaction mitigation techniques primarily can be categorized into three categories, i.e., soil reinforcement, desaturation, and drainage improvement. The conventional liquefaction mitigation techniques perform reasonably well in case of a small earthquake. However, recent research developments and several case histories depicted the limitations of these remedial measures. Besides, their effectiveness under different strong earthquakes is still poorly understood. The presented research aims for the development and investigation of the efficacy of liquefaction mitigation techniques under different strong ground motions. Ground motion recorded at Hachinohe Port during the 1968 Tokachi-Oki earthquake (NS component) and design earthquake motion for highway bridges in Japan (2-I-I-3, NS component) recorded at the ground surface near New Bansuikyo Bridge, Tochigi during the 2011 Tohoku Earthquake are considered as different strong ground motions in this dissertation. Two temporary structures namely buffer tank (BT) and flare stack (FS) mounted on shallow foundations at an industrial process plant are considered as target structures.

Initially, liquefaction-induced effects on foundation-structure systems (BT and FS), presumably resting on a uniform deposit of liquefiable ground is investigated using the centrifuge lab facility. Centrifuge test depicted that the shallow foundations undergo severe deformation during strong ground motion. Then, a reliability assessment of the physical modeling of liquefaction-induced effects on shallow foundations considering nonuniformity in the centrifuge model is carried out using two-dimensional (2D) stochastic numerical analyses. The nonuniformity in the centrifuge model is found to have a significant impact on the deformation of the foundation-structure system. Moreover, the liquefaction extent in the model ground is found to vary with the centrifuge model's nonuniformity and is correlated with the deformation of the foundation-structure system.

Centrifuge experiments are also carried out to examine the efficacy of induced partial saturation as a liquefaction mitigation measure. The drainage-recharge method is used to induce partial saturation within the liquefiable ground. Centrifuge test results confirmed the fact that

the compressibility of pore fluid increases because of inclusion of the air voids within the partially saturated ground. Larger compressibility of pore fluid and smaller permeability of the partially saturated ground in comparison with fully saturated ground resulted in favorable evolution of excess pore water pressure (EPWP). Besides, induced partial saturation is found to minimize the deformation of the foundation-structure systems in case of partially saturated ground.

A series of centrifuge experiments are carried out to develop a unique hybrid foundation to mitigate the liquefaction-induced effects on shallow foundations. The proposed hybrid foundation is a combination of the gravel drainage system and friction piles having spiral blades devised under the footing as a hybrid mitigation technique against the liquefaction-induced effects. The presence of gravel drainage increased the dissipation rate (through radial flow towards the gravel drainage zone) of generated EPWP and reduced the post-shaking settlement. Centrifuge tests results also depicted that the proposed hybrid foundation can mitigate the liquefaction-induced effects on shallow foundations during the strong ground motion. Any structure may experience several moderate to strong earthquakes during its lifespan. The alteration of the ground condition is apparent due to induced cyclic stress, shear-induced deformation, development of excess pore water pressure (EPWP), localized drainage, post-liquefaction reconsolidation, void re-distribution, and inertial and kinematic interaction within the soil-foundation-structure system. Therefore, the effectiveness of induced partial saturation and proposed hybrid foundation under various level of earthquakes is examined to understand the long term efficacy of their performance to mitigate the liquefaction-induced effects. Besides, the implications of different strong ground motions on the alterations of the characteristics of the ground are also discussed.

The gravel drainage system is an integral part of the developed hybrid foundation which is susceptible to be affected by the nonuniformity of the ground. Therefore, the implications of the nonuniform ground on the performance of a granular column are also investigated. Stochastic analyses results demonstrated that the reliability assessment of the performance of the granular column is essential for better engineering judgment associated with a desired level of confidence. The probabilistic estimation of liquefaction-induced ground deformation possesses significant practical importance and provides useful information to assess the reliability of the performance of the granular column.

Table of contents

List of figures

List of tables

Chapter 1. Introduction

Soil liquefaction is one of the most complex phenomena in geotechnical earthquake engineering. The devastating effects of liquefaction, sprang the attention of geotechnical engineers within three months' period in 1964, because of the Good Friday earthquake in Alaska, followed by the Niigata earthquake in Japan (Kramer, 1996). Since then, much research has been done to assess and mitigate the liquefaction-induced effects on the built environment. The technological advancements in the experiment facilities (at element and system levels) and availability of the sophisticated soil-constitutive models, along with the possibility of enormous computational capacities, have helped researchers to get a better insight of liquefaction and associated effects.

Liquefaction usually occurs in the saturated loose cohesionless soil during dynamic/cyclic loading. During liquefaction, soil loses its shear strength due to the generation of excess pore water pressure (EPWP) leading to ground failure and sometimes resulting in the collapse of associated foundation-structure systems. At the microscale, soil deposit consists of an assemblage of individual soil particles, interacting with each other, and employing its strength. Loose saturated cohesionless soil tends to contract in its volume when subjected to dynamic/cyclic loading. The pore water filled in voids of saturated soil is intercepted as the ground behaves under undrained conditions. Naturally, the earthquake event is quick enough that the pore water is almost restricted to escape, which explained the rationale behind the assumption of the undrained condition. The tendency of contraction of loose soil steers pore water pressure to increase manifolds, which eventually decreases its shear strength. Sometimes, the whole process of developing the EPWP is so quick, that within a few seconds, the entire ground gets liquefied. Liquefaction said to have occurred at a particular depth within the ground if the generated EPWP reaches equal to the initial vertical effective stress. This condition makes the excess pore water pressure ratio (r_u), i.e., the ratio of EPWP to the initial vertical effective stress, being equal to one. Besides, the manifestation is associated with several other factors, as mentioned below:

1. Development of excessive shear strain within the ground
2. Void re-distribution, diffusion, and localization of volumetric strain
3. Development of cracks, boils, and lateral spreading
4. Post-earthquake reconsolidation strains

Soil liquefaction and related ground failure have been extensively studied by many researchers, e.g., Seed et al., 1989; Ishihara et al., 1992; Bardet et al., 1995; Sugito et al., 2000; Green et al., 2008; Nakai and Sekiguchi, 2011 and Cubrinovski and McCahon, 2012. Liquefaction has caused severe damage to the built environment. History has witnessed the devastating consequences of liquefaction all over the world. For instance, a significant part of Christchurch city in New Zealand was devastated by soil liquefaction during the 2011 earthquake with the structural settlement, tilting, and lateral spreading (Green et al., 2011 and Cubrinovski and McCahon, 2012). The surface manifestations of level grounds, lateral spreading, failure of superstructures because of loss of bearing capacity, differential settlement, sand boils, slumping, failure of port facilities have been witnessed from time to time during many past earthquakes (Figs. 1.1-1.6; Note: these Figs. are taken from various open sources on internet).

1.1 Liquefaction-induced effects on shallow foundations

Numerous instances of damage to the built environment on shallow foundations such as settlement, tilting, and sinking, have been witnessed all over the world during many past earthquakes. In the 1964 Niigata and 1990 Luzon (Philippines) Earthquakes, most of the damaged buildings were two to four stories founded on shallow foundations and relatively thick and uniform deposits of clean sand (Liu and Dobry, 1997; Olarte et al., 2017). Surprisingly, many of the damaged structures were influenced by liquefaction of thin deposits of silt and silty sand (Seed and Idriss, 1977; Bray et al., 2000; and Bird and Bommer, 2004) in the 1999 Kocaeli (Turkey) Earthquake. Reports presented by many researchers (Nakai and Sekiguchi, 2011; Bhattacharya et al., 2011; Tokimatsu and Katsumata, 2012; and Yamaguchi et al., 2012) described the role of liquefaction to the damage of buildings, specifically in the reclaimed land during Tohoku 2011 earthquake. Numerous sand boils, and large ground settlement up to 60 cm, as well as the settlement/tilting of the wooden and reinforced concrete buildings mounted on spread foundations, was seen throughout the affected area.

Sand boils erupted during 2011
Christchurch Earthquake

Sand boils erupted during 1989
Loma Prieta Earthquake

Fig. 1.1.   Examples of sand boil during different earthquakes (Courtesy of UW College of Engineering, USA)

Fig. 1.2.   The collapse of buildings due to loss of bearing capacity during the 1964 Niigata Earthquake (Courtesy of the National Information Service for Earthquake Engineering, EERC, University of California, Berkeley, USA)

Fig. 1.3.   Damage to Lower San Fernando Dam during 1971 San Fernando Earthquake (Courtesy of the National Information Service for Earthquake Engineering, EERC, University

of California, Berkeley, USA)

Fig. 1.4.   The collapse of the bridge due to liquefaction induced lateral movement of the foundation during the 1964 Niigata Earthquake (Courtesy of the National Information Service for Earthquake Engineering, EERC, University of California, Berkeley, USA)

Fig. 1.5.   Damage to port facilities during the 1995 Kobe Earthquake (Courtesy of UW College of Engineering, USA)

Fig. 1.6.   Soil liquefaction and lateral spreading in Tumwater, WA after the 2001 Nisqually Earthquake (Courtesy of UW College of Engineering, USA)

The development of cyclic stress because of strong shaking is one of the vital factors causing liquefaction-induced deformations (Dashti et al., 2010). However, the overall deformation mechanism of shallow foundation resting on the liquefiable ground is a complex phenomenon and presumed to be affected by several factors, e.g., induced cyclic stress, foundation configuration, ground condition, development of EPWP, localized drainage, post-liquefaction reconsolidation, void re-distribution, and inertial and kinematic interaction within the soil-foundation-structure system. The well-known procedures to evaluate the liquefaction-induced settlement in the free field by Tokimatsu and Seed (1987), Ishihara and Yoshimine (1992) do not incorporate the combined effects of deviatoric and volumetric-induced building settlement due to cyclic soil softening/stiffening under static and dynamic loading. Many researchers found that the foundation width, and height/width ratio is one of the governing factors to influence the building settlement and tilt along with bearing failure (Yoshimi, 1977; Liu and Dobry, 1997; and Sancio et al., 2004). It is proposed that the 3D drainage affects the overall settlement behavior of shallow foundation as the partial drainage is shown to set up simultaneously along with the generation of EPWP because of the migration of pore fluid towards the top surface (Liu and Dobry, 1997). However, a well-accepted settlement mechanism because of drainage has not been set up so far. The void re-distribution mechanism is believed to influence the shear-induced settlement mechanism by many researchers (Elgamal et al., 1989; Dobry and Liu, 1992 and Kokusho 1999). The post-earthquake settlement behavior of shallow foundation is believed to be affected by the alteration in density, development of volumetric strains and the permeability of the ground (Ishihara and Yoshimine, 1992; Liu and Dobry, 1997, Shamoto et al., 1998; and Zhang and Wang, 2012).

1.2 Liquefaction mitigation

Soil remediation measures are requisite for liquefaction prone sites. Over the past few decades, extensive efforts and contributions have been made by geotechnical earthquake engineering society to grasp the physics behind the liquefaction and for the development of the remedial measures for the liquefaction-induced effects. Liquefaction mitigation techniques primarily can be categorized into three categories, i.e., soil reinforcement, desaturation, and drainage improvement. The probable vulnerability of existing structures founded on the soil, which is

prone to liquefaction, continued to be a significant concern. The challenging task is to assess the mitigation techniques which could be adopted as non-disruptive mitigation for already developed sites explicitly having important and vulnerable structures. The other essential aspects of liquefaction mitigation methods are: achieving the liquefaction mitigation in a large area at low cost; and combining the liquefaction mitigation with environmental friendliness and low carbon economy (Huang and Wen, 2015). Hausler and Sitar (2001) conducted a treatise over 90 case histories on the performance of improved sites from 14 earthquakes in Japan, Taiwan, Turkey, and the United States. They found that about 10 percent of the surveyed sites required significant post-earthquake remediation or demolition because of liquefaction. This emphasizes that even after ground improvement, the effects of liquefaction cannot be devoid entirely. Mitchell et al. (1995) explained the use of different soil mitigation methodologies to countermeasure the liquefaction. Several other excellent documented research has described the technical specifications, limitations, applicability, and design procedure of liquefaction mitigation methodologies such as Mitchell (1981), and JGS (1998).

1.2.1 Soil reinforcement

Soil reinforcement is intended to increase the liquefaction resistance of the ground. Soil replacement, soil densification, and bonding of soil grains with the binding agents are some means to employ the reinforcement within the ground. Sand compaction pile, vibration compaction, dynamic compaction, blast compaction, and compaction grouting are a few commonly used methods for soil densification (Schaefer et al., 1997). Permeation grouting, splitting grouting, jet grouting, deep mixing, and bio-cementation are a few frequently used methods to bind the soil grains altogether, which eventually increases the liquefaction resistance of the ground (Gallagher and Mitchell, 2002). The concept behind the soil reinforcement primarily relies on densification, reinforcement, cementation, or solidification by grouting, which increases the liquefaction resistance of clean sand (Thevenayagam and Martin, 2002). Besides, friction piles in the liquefiable ground, under the shallow foundation with the flexible connection can be used to minimize the differential settlement of foundation during the seismic event. Friction piles are intending to yield the frictional resistance generated along the shaft of the pile. Friction pile can be used to reduce the liquefaction-induced damage to the foundation structure system. However, many case studies show the tremendous damage to the piles and

associated structures caused by excessive liquefaction (Hamada, 1992; Tokimatsu et al., 1996; Ishihara, 1997 and Madabhushi et al., 2005).

1.2.2 De-saturation

In recent years, many researchers have explored liquefaction mitigation techniques that are different from commonly available practices as presented in reports by Mitchell et al. (1995) and Seed et al. (2001). Among those newly developed methods, de-saturation (induced partial saturation is one of the novel techniques to increase the liquefaction resistance of liquefiable ground. De-saturation of the ground to improve the liquefaction resistance has gained much credibility in recent years. Lowering the groundwater table, air injection, and biogas are few of the ways to impart the partial saturation within the ground. Several methods have been adopted to induce partial saturation within the ground such as water electrolysis (Yegian et al., 2007), drainage-recharge (Yegian et al., 2007; Takemura et al., 2008, Kumar et al., 2019), chemical sodium perborate (E-Bayat et al., 2013), biogas (He et al., 2013) and air injection (Tokimatsu et al., 1990; Okamura et al., 2003). Laboratory experiments are performed by many researchers (Yoshimi et al., 1989 and Okamura and Soga, 2006), and the results depict that even small change in the degree of saturation can increase the liquefaction resistance of liquefiable soil considerably. The inclusion of air voids within the saturated ground (partial saturation) tends to decrease the overall bulk modulus and increase the compressibility of the air-water mixture. The change in bulk modulus of the soil-water mixture favorably affects the overall permeability of the ground. During shaking, entrapped air absorbs the significant amount of generated EPWP by reducing its volume (Okamura and Soga, 2006) and thus eventually improve the performance of the ground against liquefaction.

1.2.3 Drainage improvement

Liquefaction mitigation by stone column or gravel drainage piles is one of the pronounced techniques which is used to help quick dissipation of EPWP generated during the earthquake (Seed and booker, 1977; and Tokimatsu and Yoshimi, 1980). In addition, the other possible benefits of gravel drains include densification of surrounding soil while installation and re-distribution of earthquake-induced or pre-existing stress (Adalier et al., 2003).

Seed and Booker (1977) suggested that the permeability of the gravel drains should be at

least two orders of magnitude larger than the surrounding soil to avoid the significant generation of EPWP within the gravel drains. They proposed the design charts for the evaluation of gravel drain diameter and adequate spacing for desirable excess pore pressure ratio (r_u) during the different levels of shakings. Although many researchers have found that the pioneering design charts for gravel drain developed by Seed and Booker (1977), overestimate the performance of gravel drains (Tokimatsu and Yoshimi, 1980; Boulanger et al., 1998; and Adalier and Elgamal, 2004). Onoue (1988) designed modified design charts for the gravel drains and realistically incorporated the effects of drain resistance, while the analyses of Seed and Booker (1977) largely underestimate the range of drain permeability that adversely affects their performance.

Adalier and Elgamal (2004) performed centrifuge experiments to understand the liquefaction mitigation capabilities of stone columns and associated ground deformations. They concluded that if no attempt is made to densify the soil during installation, the performance will depend on increased drainage effects. The ancillary benefits of treating the ground with stone columns are soil densification, restriction of shear deformation and offering the containment of the encapsulated soil, and providing stiffening-matrix effects (reducing the stress in adjacent soil), though this effect is not well established yet, and more research is needed in this direction. Ashford et al. (2000a, 2000b) presented the full-scale liquefaction experiments involving gravel drainage systems for liquefaction mitigation countermeasures. They described that the presence of gravel drains reduces the EPWP and increases the dissipation rate of EPWP. Brennan and Madabhushi (2002, 2006) did extensive physical modeling investigation to understand the effectiveness of vertical drains in mitigation of liquefaction. Excess pore pressure generated during earthquakes is expected to create vertical hydraulic gradients acting to dissipate fluid upward. The authors found that the flow front (zone of drainage influence at any time) play a vital role in the performance of gravel drains. The flow front slows down with distance from the gravel drain, and hence it is highly relevant to consider the effective radius and precise spacing of the gravel drains. Yasuhara et al. (2004) performed a 1g model test on the liquefiable inclined ground and concluded that the vertical settlement is less when the ground is treated with gravel drains, and gravel drain prevents the liquefaction up to considerable extent even if the liquefaction occurs at some places. The observed lateral deformation was less due to gravel drains. They also concluded that gravel drain installed in the medium dense sand could mitigate the liquefaction effects even in case of the inclined slope.

1.3 Objectives and scope of the study

Implementation of a suitable mitigation technique is essential for any site which is prone to seismically induced liquefaction during the commencement of any project. Mitigation techniques discussed earlier performs reasonably well in case of a small earthquake. However, their effectiveness during a moderate or strong earthquake is still poorly understood (Hausler and Sitar, 2001). The presented research aims for the development and investigation of the efficacy of liquefaction mitigation techniques under different strong ground motions. Temporary structures namely buffer tank (BT) and flare stack (FS) mounted on shallow foundations at an industrial process plant are considered as target structures. Ground motion recorded at Hachinohe Port during the 1968 Tokachi-Oki earthquake (NS component) and design earthquake motion for highway bridges in Japan (2-I-I-3, NS component) recorded at the ground surface near New Bansuikyo Bridge, Tochigi during the 2011 Tohoku Earthquake are considered as different strong ground motions in this dissertation. The explicit objectives and scope of this research are as below:

Liquefaction-induced effects and reliability assessment of centrifuge test: The technological advancements in the experiment facilities (e.g., physical modeling using centrifuge experiment) have enabled the researchers to get a better insight of liquefaction and associated induced effects. Dynamic centrifuge modeling has been widely used to understand the liquefaction–induced effects on shallow foundations resting on presumably uniform deposits of clean and loose to medium dense sand (Yoshimi and Tokimatsu 1977; Liu and Dobry 1997; Dashti et al., 2009; Olarte et al., 2017; Kumar et al., 2019a, 2019b). Several researchers have used dynamic centrifuge model test results to validate their soil constitutive models and finite element numerical models (Popescu and Prevost, 1993; Byrne et al., 2004; Elgamal et al., 2005; Rayhani and El Naggar, 2008; Montgomery and Boulanger, 2016; Macedo and Bray, 2018). In both cases, the model ground is usually considered to have uniform soil properties. However, the model ground is prone to spatial nonuniformity and may affect engineering judgment based on physical modeling. The reliability of the physical modeling of liquefaction-induced effects on shallow foundations is assessed considering the spatial variability in the centrifuge model.

Induced partial saturation as a liquefaction mitigation measure: This dissertation further explores the efficacy of induced partial saturation to mitigate the liquefaction-induced

effects on shallow foundations. Induced partial saturation is one of the novel techniques to increase the liquefaction resistance of the saturated sandy ground. Nonetheless, a limited number of experimental studies are available on the delineation of this method. The effectiveness of air voids under strong shaking, compressibility of air-fluid mixture, partial drainage effects on the evolution of EPWP, post-liquefaction behavior and inertial and kinematic interaction of soil-foundation-structure system are essential to assimilate the maximum benefits of this technique.

Development of a hybrid foundation: A unique hybrid foundation is developed to mitigate the liquefaction-induced effects on shallow foundations. The efficacy of a hybrid foundation is assessed using the centrifuge lab facility. The proposed hybrid foundation is a combination of the gravel drainage system and friction piles having spiral blades devised under the footing as a hybrid mitigation technique. Liquefaction mitigation by gravel drainage piles is one of the pronounced techniques which is used to help quick dissipation of EPWP generated during the earthquake, eventually increases the liquefaction resistance of liquefiable ground (Seed and Booker, 1977; Priebe, 1989; Baez and Martin, 1993; and Adalier et al. 2003). The satisfactory performance of gravel drainage against the small magnitude earthquakes has been corroborated by physical model tests and field studies carried out by many researchers (Priebe, 1989; Baez and Martin, 1993; Adalier et al., 2003; and Brennan and Madabhushi, 2006). However, during a moderate or strong earthquake, the build-up of EPWP due to shaking may exceed the capacity of the gravel drainage system; and apparently, the foundation ground may be liquefied. Large dissipation rate of EPWP after the liquefaction due to the presence of gravel drains may adversely increase the post-liquefaction settlement of the foundation and associated structure. To overcome the limitations of gravel drainage and to minimize the differential settlement of shallow foundation in case of liquefaction state occurred within the ground, friction piles with spiral blades are proposed under the footing as an integral part of the hybrid foundation.

Effectiveness of liquefaction mitigation techniques under different strong ground motions: Any structure may experience several moderate to strong earthquakes during its lifespan. The alteration of the ground condition is apparent due to induced cyclic stress, shear-induced deformation, development of EPWP, localized drainage, post-liquefaction reconsolidation, void re-distribution, and inertial and kinematic interaction within the soil-foundation-structure system. These may affect the effectiveness of liquefaction mitigation

techniques under next strong ground motion. Therefore, the effectiveness of these mitigation techniques under different strong ground motions are necessary to examine the long term efficacy of their performance to mitigate the liquefaction-induced effects.

Effects of nonuniformity of the ground on the performance of a granular column: The gravel drainage system is an integral part of the above mentioned hybrid foundation. A granular column facilitates the quick dissipation of EPWP generated during the dynamic event. Besides, densification during installation, increment in lateral stress, and apparent shear reinforcement presumed to increase the liquefaction resistance of the ground treated with granular columns. However, case histories and recent research development have exhibited the limitations of granular columns under strong earthquakes (Boulanger et al., 1998; Adalier et al., 2003; Adalier and Elgamal, 2004; Brennan and Madabhushi, 2002; Olarte et al., 2017; and Kumar et al., 2019b). Besides, the performance of granular column is susceptible to be affected due to the spatial nonuniformity of the ground. Moreover, the mechanism of liquefaction resistance, drainage effects, deformation pattern, and shear reinforcement due to granular columns are poorly understood. Therefore, the reliability assessment of the effectiveness of granular column is also carried out considering the spatial nonuniformity of the ground and practical physical characteristics of granular column (e.g. relative density, drainage capacity, shear reinforcement).

1.4 Outline of the dissertation

The dissertation consists of seven chapters:

Chapter 1: Introduction – this chapter comprises the background and treatise of liquefaction and its remedial measures. The objectives and scope of the dissertation are presented.

Chapter 2: Reliability assessment of centrifuge test – this chapter initially investigates the liquefaction-induced effects on shallow foundations. The reliability of the centrifuge test is evaluated considering the nonuniformity in the centrifuge model.

Chapter 3: Centrifuge modeling of induced partial saturation – this chapter discusses the experiment results of two dynamic centrifuge tests carried out to investigate the effectiveness of induced partial saturation to mitigate the liquefaction-induced effects on shallow foundations.

Chapter 4: Centrifuge modeling of hybrid foundation – this chapter discusses the modeling

scheme of the proposed hybrid foundation and explores its performance against the liquefaction-induced effects on shallow foundations.

Chapter 5: Efficacy of liquefaction mitigation techniques under different strong ground motions – this chapter explores the performance of induced partial saturation and hybrid foundation under different strong ground motions.

Chapter 6: Reliability assessment of performance of a granular column – this chapter discusses the reliability assessment of the performance of granular column in a nonuniform liquefiable ground to mitigate the liquefaction-induced ground deformation.

Chapter 7: Conclusions and recommendations – this chapter summarizes the dissertation, significant findings, and future recommendations.

Chapter 2. Reliability assessment of centrifuge test

Physical modeling has been widely used to simulate geotechnical earthquake engineering-related problems and to validate finite element numerical models. Generally, the predicted behavior of shallow foundations resting on the liquefiable ground using the centrifuge model test and the validation of numerical models are based on the assumption that the model ground has uniform soil properties. However, the centrifuge model ground is prone to spatial nonuniformity even though the model ground is intended to be uniformly reconstituted under gravity conditions (Schofield, 1980; Zhang et al., 2008). With the increasing use of centrifuge modeling for the performance prediction of shallow foundations and calibration of numerical models, it is essential to understand the reliability of centrifuge model tests. Reliability analyses provide a means of evaluating the combined effects of uncertainties in the parameters involved in the calculations, and they offer a useful supplement to traditional engineering judgment (Duncan, 2000). In this chapter, an attempt is made to evaluate the reliability of the physical modeling of liquefaction-induced effects on shallow foundations considering the spatial nonuniformity in the centrifuge model.

2.1 Physical model

A dynamic centrifuge experiment is carried out to investigate the liquefaction-induced effects on shallow foundations resting on a level deposit of liquefiable Toyoura sand. A flexible laminar container with inner dimensions of 600 x 250 x 438 mm (model scale) in length, width and height respectively, is used to frame the centrifuge model. The laminar box is composed of many aluminum rectangular alloy rings which allow its movement along with soil mass, creating a flexible boundary and establishing the uniform dynamic shear stresses within the model ground during the dynamic excitation. The centrifuge model contains two shallow foundations and associated superstructures, namely, buffer tank (BT, 4x4x1 m^3) and flare stack (FS, 4x4x2 m^3), imposing average bearing pressures of 51.2 kPa and 71.2 kPa, respectively, at 0.8 m below the surface of the model ground at the prototype scale, as shown in Fig. 2.1(a). This centrifuge test (Fig. 2.1) is used as Model 1 in Chapter 4 for the development of hybrid foundation and hence same terminology is used for consistency. The height of prototype

targeted structures BT and FS, are 15 m and 32 m respectively, having distributed mass along the height. In the model scale, the height of both BT and FS (after scaling down for $N = 40$) turned out to be quite disproportionate as per the laminar container size. To ensure the fundamental design periods of BT and FS (0.4s and 0.5 s, respectively), and to adjust the center of gravity of centrifuge model, masses are lumped at the top of both BT and FS. This improvisation reduced the height of BT and FS by 50.10 and 56.25% respectively.

Dynamic centrifuge model tests are carried out utilizing the Tokyo Tech Mark III centrifuge facility (Takemura et al., 1999) with a radius of 2.45 m, at a centrifugal acceleration of 40g (N = 40; scaling law is tabulated in Table 2.1). The centrifuge model tests simulate a prototype saturated soil deposit at a depth of 10 m, with a water table located 1.8 m below the top surface. Sides of the laminar box are covered with the polyethylene sheet to secure water tightness and to avoid any sand particles jamming between the alloy rings. Then model ground is prepared using Toyoura sand (properties are tabulated in Table 2.2) with a target relative density of 50% by the air pluviation method using a sand hopper with a nozzle outlet. The sand hopper is calibrated in terms of the falling height and pouring rate of the Toyoura sand before preparing the model ground. Multiple transducers (e.g., pore pressure transducers, accelerometers, laser displacement transducers, and potentiometers) are carefully placed at desirable locations (see Table 2.3) during the model ground preparation as shown in Fig. 2.1(b). The initial vertical effective stress is calculated by subtracting the pore water pressure from the total stress. Boussinesq's method is used to calculate the vertical stress because of foundation-structure at required depths which is further used to estimate the vertical effective stresses as tabulated in Table 2.3.

Centrifuge model is tested under the earthquake ground motion recorded at the Hachinohe Port in 1968 Tokachi-Oki Earthquake (NS component, see Fig. 2.2). Before applying the Tokachi-Oki ground motion, the models are subjected to white noise to evaluate the dynamic characteristics of the system. The model ground is saturated with the viscous fluid, i.e., a mixture of water and 2.0% Hydroxypropylmethyl cellulose solution (Metolose by Shin-Etsu Chemical Co., Ltd.; grade 60SH-50) by weight of water, to achieve a viscosity about 40-50 times that of water. It is to be noted that the series of experiments (Models 1-6, details are given in Chapter 4) were carried out within a span of almost one year. The viscosity tends to change depending on the room temperature. This solution is used to ensure the compatibility of prototype permeability of the soil to set up the affinity between dynamic and diffusion scaling

laws (Schofield, 1981).
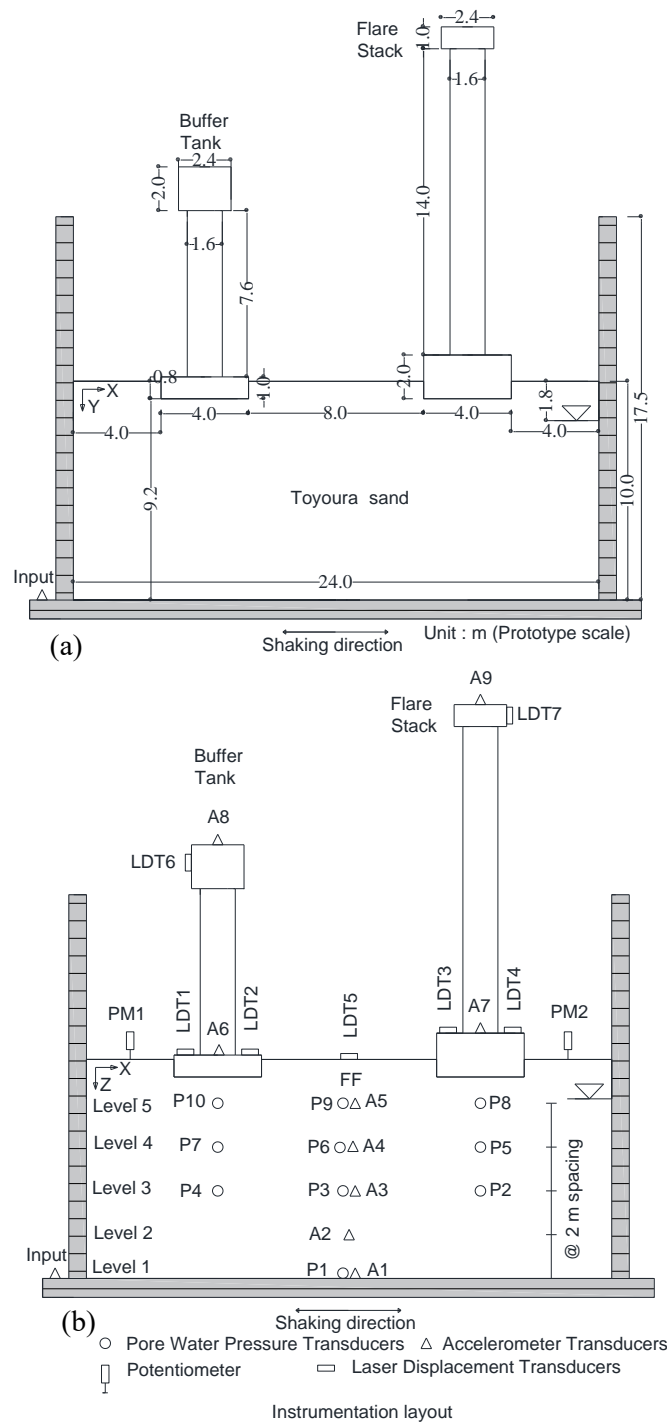
Fig. 2.1. Centrifuge model layout (Model 1): (a) model configuration at prototype scale and (b) locations of different transducers

The saturation within the model ground is achieved by dripping the de-aired Metolose

solution slowly from the top of the container under a vacuum of 760 mmHg over the sponges at the surface of the model ground. The dripped solution slowly moves downward and saturates the model ground uniformly. The saturation is continued until the water table (Metolose solution table) reaches up to the top surface of the model ground. After the saturation, superstructures are mounted over the footings. The configuration of model foundation and structure system is tabulated in Table 2.4.
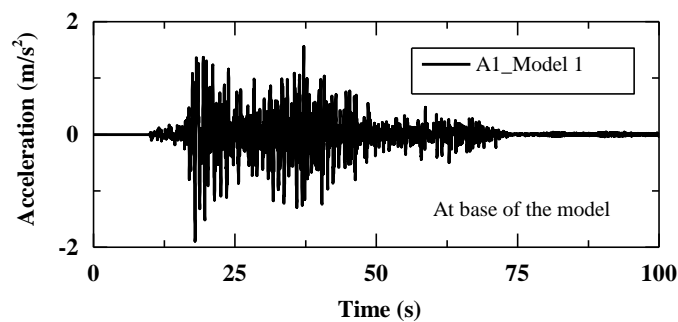
Fig. 2.2. Tokachi-Oki ground motion used as dynamic excitation

Table 2.1. Scaling law for centrifuge test (Schofield, 1981)

Parameters	Ratio of model to prototype
Length	$1/N$
Area	$1/N^2$
Volume	$1/N^3$
Acceleration	N
Stress	1
Strain	1
Time (dynamic)	$1/N$
Force	$1/N^2$
Bending moment	$1/N^3$

2.1.1   *Liquefaction-induced effects on shallow foundation*

An attempt is made to understand the behavior of shallow foundation resting on the liquefiable ground during a strong ground motion. All test results are in prototype scale unless mentioned otherwise. Evolution of excess pore water pressure (EPWP) plays a vital role in the

manifestation of liquefaction during the dynamic event. Fig. 2.3 depicts the EPWP generation and dissipation trends within the ground during Tokachi-Oki ground motion. Soils at certain depth undergo liquefaction state if the excess pore water pressure ratio (r_u), which is calculated by dividing the generated EPWP by the initial vertical effective stress at respective depth, reaches one.

Table 2.2. Index properties of Toyoura sand

Description	Toyoura sand
Specific gravity, G_s	2.65
D_{50} (mm)	0.19
D_{10} (mm)	0.14
Maximum void ratio, e_{max}	0.973
Minimum void ratio, e_{min}	0.609
Permeability, k (m/s)	2E-4
Relative density, D_R	~50%

Table 2.3. Locations of different transducers within the model grounds

Level	Transducers*	Location (prototype scale)		Initial vertical effective stress (σ'_{vo}) at different levels**	
		X	Z (depth)	Magnitude, kPa	Description
		m	m	(prototype scale)	
Level 1	P1, A1	12	10	102.40	Model centerline
Level 2	A2	12	8	73.92	Model centerline
Level 3	P2	18	6	61.22	Below FS footing
	P3, A3	12	6	65.44	Model centerline
	P4	6	6	57.52	Below BT footing
Level 4	P5	18	4	54.49	Below FS footing
	P6, A4	12	4	41.96	Model centerline
	P7	6	4	47.49	Below BT footing
Level 5	P8	18	2	53.80	Below FS footing
	P9, A5	12	2	26.16	Model centerline
	P10	6	2	41.80	Below BT footing

* P: Pore water pressure transducers, A: Accelerometers
** Including vertical stress induced by the foundation-structure systems

Table 2.4. Model foundation and superstructure configuration

Property	Model foundation and superstructure*	
	Buffer Tank	Flare Stack
Footing dimension	4 x 4 x 1 m^3	4 x 4 x 2 m^3
Material used	Aluminum	Aluminum
Mass of footing	44.8 ton	87.04 ton
Thickness of superstructure	6 cm	6 cm
Outer diameter of superstructure	1.6 m	1.6 m
Height of lumped mass	7.6 m	14 m
Flexural rigidity (EI) of the superstructure	3.15E6 kN-m^2	3.15E6 kN-m^2
Lumped mass	28.16 ton	14.08 ton
Bearing pressure @ 40g	51.2 kPa	71.2 kPa
Design period of foundation-structure system	0.4s (2.5 Hz)	0.5s (2.0 Hz)

*All units are given in prototype scale

It is evident from Fig. 2.3 that the ground liquefies (placing of pore pressure transducers in the model ground are shown in Fig. 2.1(b)) under both FS (at P2) and BT (at P4). However, at P3 the maximum magnitude of EPWP does not reach the liquefaction state ($r_u = 1$ line). The ground exhibits the liquefaction state under BT (at P7) and along the model centerline (at P6); however, the time history of P5 shows that the ground does not liquefy under FS. The induced cyclic stress ratio under FS during the shaking is relatively small as the initial vertical effective stress at P5 (see Table 2.3) is significantly large in comparison with the one at P6 and P7, which avoid the liquefaction state to be achieved under FS (at P5). In general, the whole ground liquefied or reached nearly the liquefaction state during Tokachi-Oki ground motion except in the vicinity of the FS footing. Soon after the shaking terminates, the EPWP starts dissipating at P2, P3, and P4.
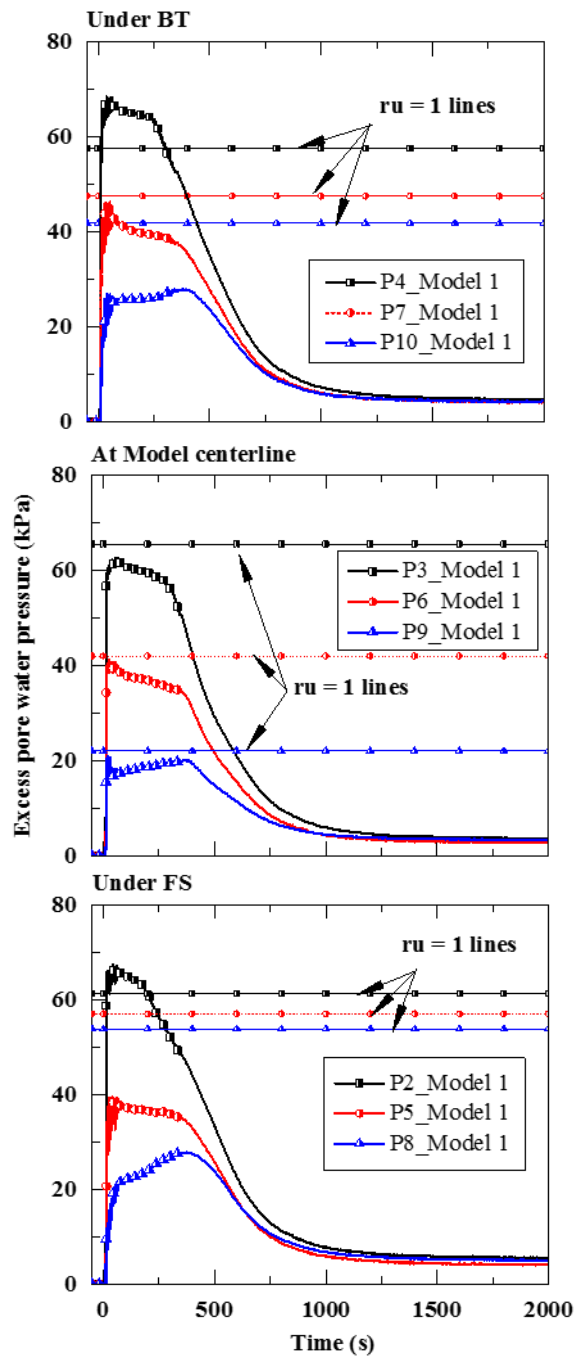
Fig. 2.3. Excess pore water pressure time histories within the model ground during Tokachi-Oki ground motion

It is apparent that at a shallower depth (at Levels 4 and 5, see Fig. 2.1(b)), the pore pressure does not show the trace of dissipation even after shaking approximately until 400 s. The reason for delayed dissipation of EPWP at shallower depths is the availability of migrated pore fluid from deeper locations even after shaking for quite a long time. The drainage is only

possible through the top surface of the ground, and hence sufficient upward hydraulic gradient is set up during the shaking. The EPWP at shallower depth starts dissipating as soon as the migrated pore fluids recede from the deeper portion. All the graphs in Fig. 2.3 show the marginal magnitude of residual EPWP in dissipation phase (e.g., at 2000 s). This is associated with the fact that the pore pressure transducers (PPTs) undergo a marginal settlement during Tokachi-Oki ground motion along with changed in the overall void ratio (probably decreased) due to ground deformation and slightly rise of the water table.

Four laser displacement transducers (LDTs) as shown in Fig. 2.1(b) are used to record the settlement time histories of BT (using LDT1 and 2) and FS (using LDT3 and 4) footings, and the results are plotted in Fig. 2.4. It is to be noted that BT and FS impose bearing pressure of 51.2 and 71.2 kPa, respectively at 0.8 m below the surface of the ground. Initially, it was hypothesized that the taller structure (FS) might depict the traces of rocking motion. However, Fig. 2.4 depicted no evidence of rocking motion for both the BT and FS foundation-structure system even though they undergo excessive settlement and tilt during the dynamic event. This might be associated with the mass distribution and configuration of the foundation-structure system of BT and FS. The height of FS is significantly larger than the height of BT (see Fig. 2.1); however, the height of center of gravity from the surface of the model ground is larger for BT (3.3 and 2.3 m, respectively for BT and FS). It is evident that both BT and FS footings undergo significant settlement and tilt (specifically for FS) during Tokachi-Oki ground motion. The foundations begin to settle immediately after the shaking starts and continues even after the shaking ceases. Relatively large differential settlement of FS footing is observed in comparison with that of BT footing.
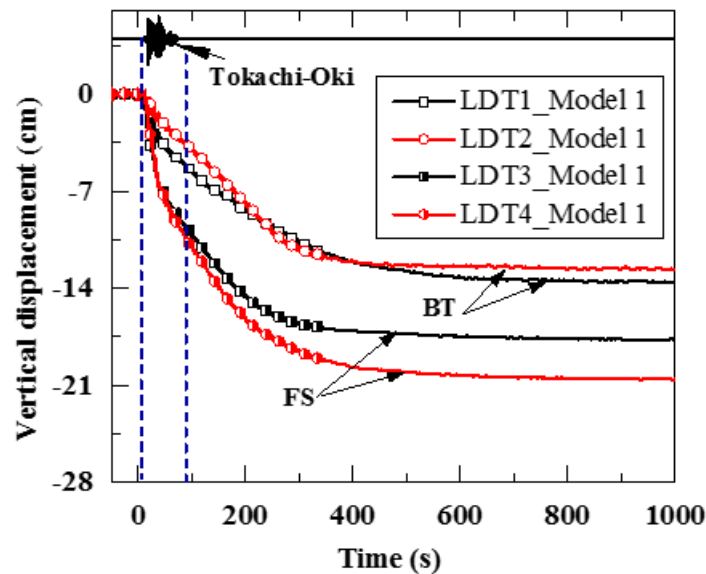
Fig. 2.4.   Settlement time histories of BT (LDT1 and 2) and FS (LDT3 and 4) during Tokachi-Oki ground motion

The assumption of the undrained condition is not valid during the dynamic event as the partial drainage starts to happen through the top surface of the ground as soon as the shaking begins. The shear strength of soil in the vicinity of the foundation begin to mobilize because of the generation of EPWP (reduction in mean vertical effective stress) and hence shear-induced settlement during shaking is apparent. The excessive settlement of both BT and FS, which cumulatively took place during both co-shaking and post-shaking period, demonstrate that the shallow foundation resting on the liquefiable ground is prone to undergo severe liquefaction-induced deformation during the earthquake. Shear-induced deformation is the governing factor for settlement during the shaking (co-shaking settlement from t =10 to t =74 s), and it can be seen from Fig. 2.5 as the co-shaking vertical settlement of FS is almost twice to the vertical settlement of BT. A significant amount of post-shaking settlement of both BT and FS is also apparent from Fig. 2.5.
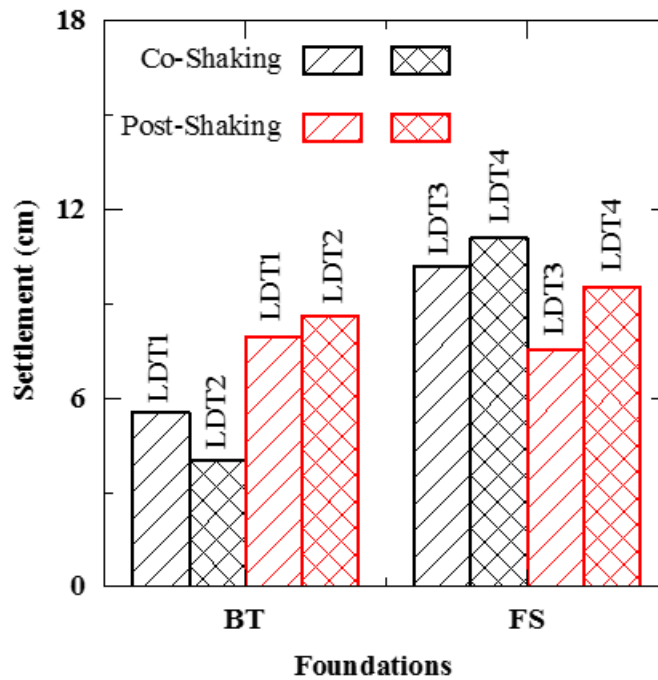
Fig. 2.5. Co-shaking and post-shaking settlement of BT (LDT1 and 2) and FS (LDT3 and 4) for Model 1

Fig. 2.6 shows the recorded acceleration time histories within the ground and at the foundation-structure system for Model 1 during Tokachi-Oki ground motion. All the observed acceleration records at Levels 2-5 (see Fig. 2.1(b)) show significant de-amplification (attenuation) in acceleration amplitude after 20 s (10 s from the beginning of shaking) and acceleration records for Levels 1 and 5 (see Fig. 2.1(b)) are shown in Fig. 2.6. The reason for this considerable de-amplification is soil softening because of the mobilization of shear strength during the seismic event. This is also attributed to the development of liquefaction state; specifically, at the shallower depth, except in the vicinity of the footings. Acceleration transducers at the foundation-structure systems (A6-A8) show amplified traces of acceleration records from 10 to 15 s (initial 5 s of shaking); however, later on, also exhibited the de-amplified records because of less seismic demand transferred due to the fact of liquefaction caused during the shaking within the ground.
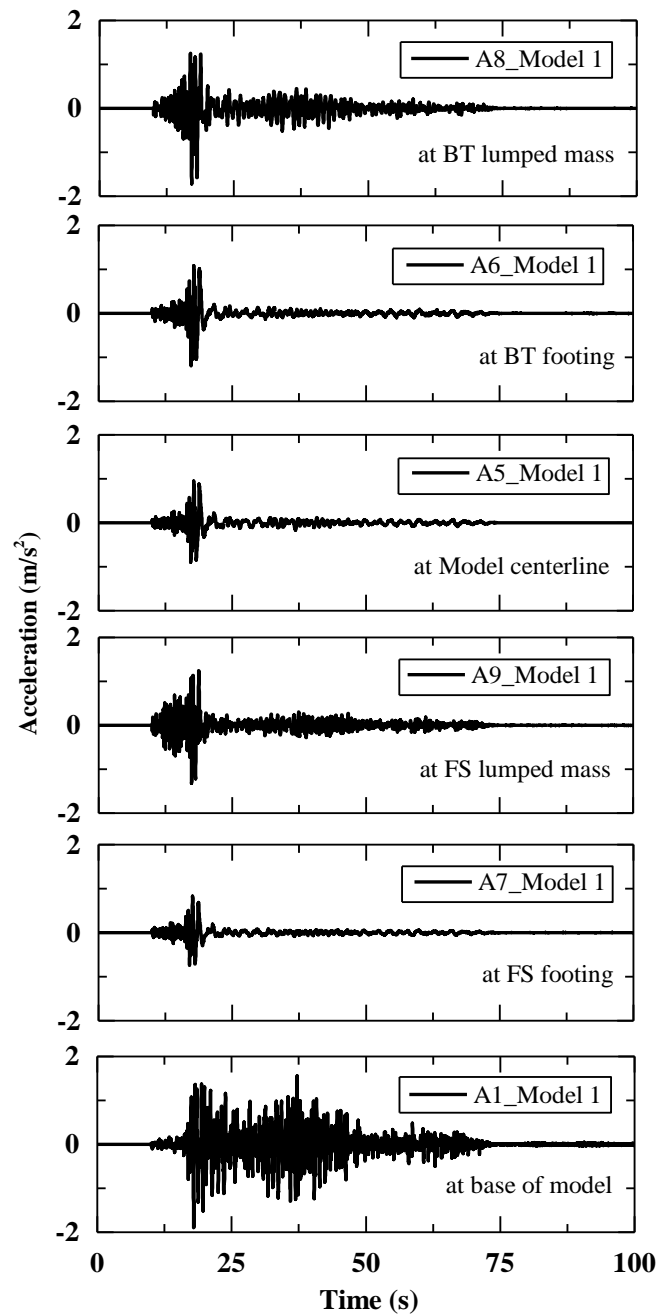
Fig. 2.6.   Acceleration response of Model 1 during Tokachi-Oki ground motion

2.2 Numerical model

Half of the centrifuge model configuration, i.e., the BT and the associated foundation, is considered for the numerical simulations, as shown in Fig. 2.7. Numerical simulations are carried out with a 2D plane strain solid-fluid fully coupled analysis approach. Rayleigh damping

of 1% at a frequency of 1 Hz, corresponding to the first-mode of a typical nonlinear ground response, is used in the analyses.
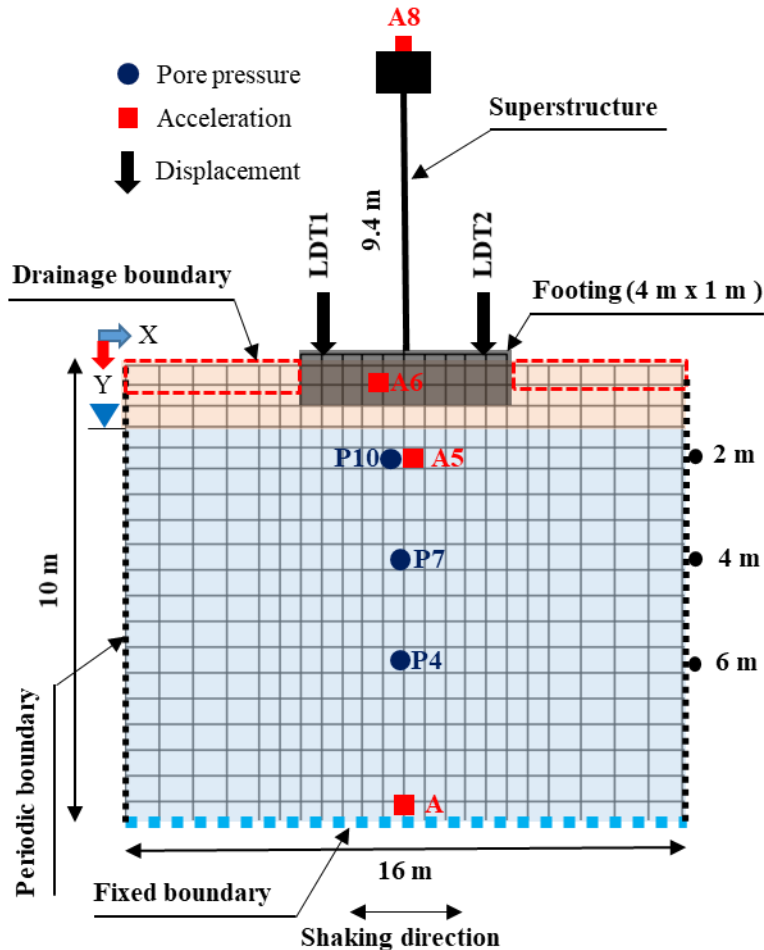
Fig. 2.7. Two-dimensional (2D) numerical model

The model ground is modeled using quadrilateral u-p (quadUP) elements (Yang, 2000). The footing is modeled using quadrilateral (quad) elements. The bottom nodes of the model ground are kept fixed in both degrees of freedom. The displacement time series of the Tokachi-Oki ground motion (NS component of the recorded shaking at the Hachinohe Port in 1968) is imposed on the bottom nodes of the model ground during dynamic analyses using the multiple support excitation technique. The footing elements are connected to the model ground using the equal degrees of freedom (equalDOF) technique in OpenSees. The side nodes of the model ground are connected using equalDOF to ensure laminar behavior during the dynamic analyses. All the nodes above the water table are assigned a pore water pressure of zero. The efficacy of mesh size is ensured before performing the numerical analyses. The maximum size of the

element at any depth is calculated to ensure the proper wave propagation with respect to the minimum wavelength corresponding to the small-strain shear wave velocity profile of the ground and the maximum frequency of the input ground motion after filtration (bandpass 0.10 Hz – 15 Hz) and baseline correction. The reduction in shear wave velocity due to soil-softening during liquefaction is accommodated with a factor of safety equal to five. In addition, the numerical results (average settlement and tilt of footing) for 50% coarser and finer mesh (by length) do not show the significant change in the results corresponding to the adopted mesh.

The PM4Sand soil constitutive model is used to capture the dynamic behavior of the model ground during shaking. PM4Sand is a stress-ratio controlled, critical state compatible, bounding surface plasticity model developed for earthquake engineering applications (Boulanger and Ziotopoulou, 2017). This constitutive model requires the specification of three primary input parameters, all of which are dimensionless: the apparent relative density (D_R), which controls the dilatancy and stress-strain response characteristics; the shear modulus coefficient (G_0), which controls the small strain shear modulus; and the contraction rate parameter (h_{po}), which is used to adjust the contraction rate to achieve the target cyclic resistance ratio. The calibrated values of G_0 and h_{po} for the deterministic analysis (with uniform ground) with $D_R = 50\%$ are 347.2 and 0.03, respectively. A detailed description of the secondary parameters and their default values can be obtained from Boulanger and Ziotopoulou (2017).

2.2.1 Parameters calibration

The parameters of the PM4Sand Model are calibrated to achieve a single-amplitude shear strain of 3% during cyclic undrained simple shear loading with an initial static shear stress ratio of zero on a horizontal plane at a single element level within 14.5 - 15.5 cycles. It is to be noted that the model's parameters are calibrated at a single element level, and the response is accepted at the system level. The primal reason for this is that the soil response change with the density which has to be properly modeled in the calculation. In addition, the parameters are calibrated to ensure that the model exhibits similar cyclic mobility, a similar accumulation rate of the shear strain, and a small strain shear modulus at a single element level, as observed in the laboratory tests. Laboratory test results from Chiaro et al. (2012, 2013) are considered for the dynamic behavior of saturated Toyoura sand with a relative density of 50% at a single element level for the generalized calibration of the PM4sand model's parameters.
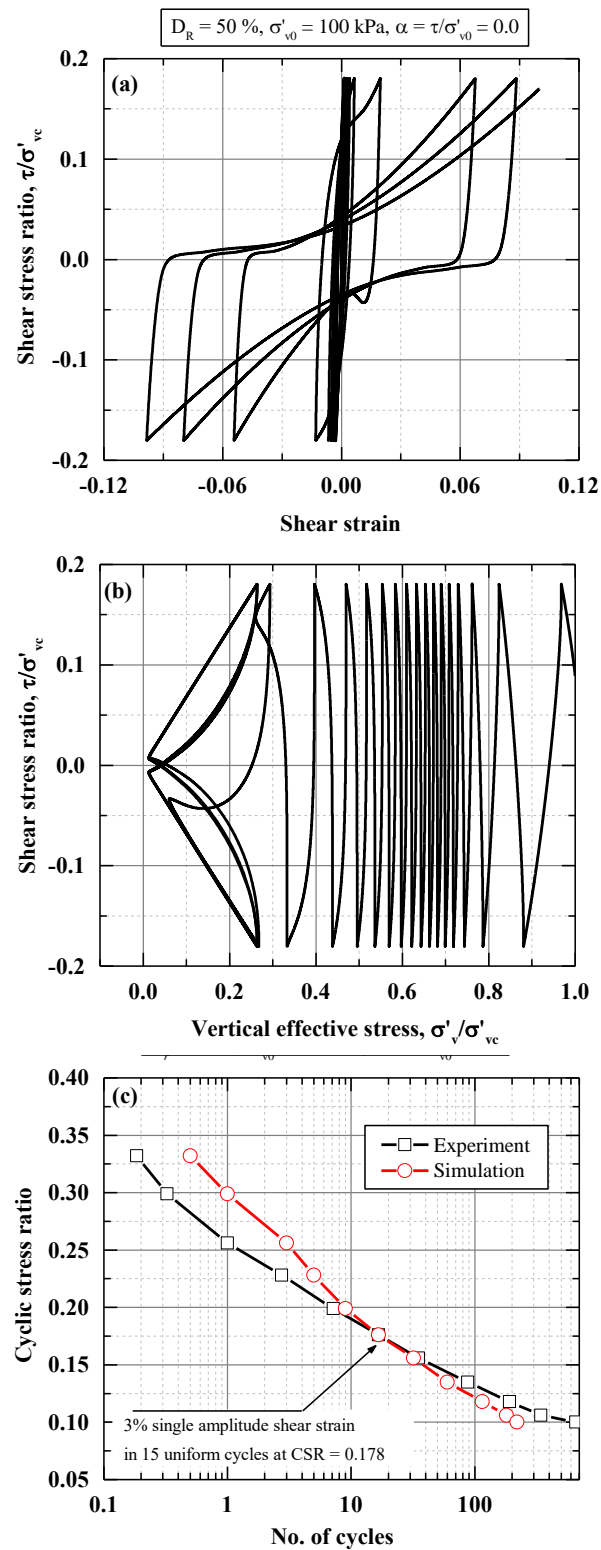
Fig. 2.8.   The response of the calibrated PM4Sand model: (a) stress-strain curve, (b) stress path, and (c) liquefaction resistance curves

Fig. 2.8(a) shows a typical response of the calibrated PM4Sand Model for a cyclic stress ratio of (CSR) = 0.178, D_R = 50%, and σ'_{vc} = 100 kPa during cyclic undrained simple shear loading with an initial static shear stress ratio of zero on a horizontal plane. The PM4Sand model exhibits the ability of shear strain accumulation commonly referred to as cyclic mobility, which is evident from the stress-strain behavior. The stress path is shown in Fig. 2.8(b). In the first cycle of loading, the vertical effective stress ratio quickly decreases to 80%. After the vertical effective stress ratio decreases to 40%, large shear strains are triggered (as shown in Fig. 2.8(a)), and the vertical effective stress ratio decreases to nearly zero within a few cycles. The numerically simulated cyclic response at the single element level is obtained after calibrating the parameters of the PM4Sand model to achieve a similar response as observed in the experiment in terms of the cyclic mobility, initial shear modulus, and accumulation rate of the shear strain. Fig 2.8(c) shows the CSR curves corresponding to single-amplitude shear strains of 3% with an initial static shear stress ratio of zero. It should be noted that each loading cycle is divided into four quarters. For instance, the 10, 10.25, 10.50, and 10.75 cycles mean that the single-amplitude shear strain of 3% is achieved in the first, second, third, and fourth quarters of the 10th cycle, respectively, for a corresponding CSR. It is evident from Fig. 2.8(c) that the PM4Sand model can map the CSR behavior of Toyoura sand as obtained in the experiment with good agreement.

2.2.2   Validation of numerical model

The ability of the numerical model is examined through the simulation of the liquefaction-induced effects on a shallow foundation at the system level. The capabilities of the PM4Sand model for simulating the dynamic behavior of saturated liquefiable ground at the single element level have been validated using Fig. 2.8. Time histories of the measured pore pressure, acceleration, and displacement at several locations (as shown in Fig. 2.7) are compared with the respective numerically simulated time histories. Fig 2.9 shows the measured and simulated time histories of the excess pore pressure. PM4Sand model can map the measured trend of the excess pore pressure evolution at all locations except that the model exhibits a relatively slower rate of generation of the excess pore pressure in the early phase of shaking. Moreover, the PM4Sand model is also able to capture the maximum magnitude of the excess pore pressure with good agreement.
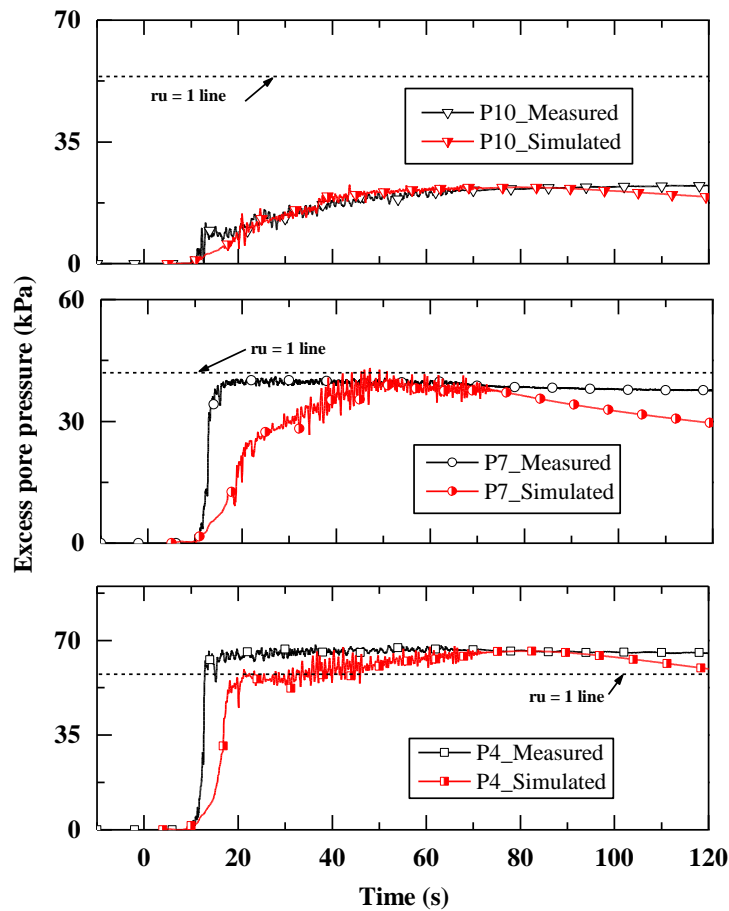
Fig. 2.9. Measured and simulated excess pore pressure during Tokachi-Oki ground motion

Fig. 2.10 shows the measured and simulated acceleration time histories along with the computed spectral acceleration ratio. The PM4Sand model shows the marginal attenuation in the acceleration time history at A8 in comparison with the trend observed in the centrifuge model test in the early phase of shaking (before 20 s). The seismic performance of the foundation-structure system on the liquefiable ground significantly depends on the low-frequency component of input shaking. The attenuation or amplification of input wave primarily governed by the liquefaction extent of the ground which is influenced by the nonuniformity in the centrifuge model. Although the numerical model shows somewhat larger spectral acceleration ratio for the high-frequency content, the Fourier amplitude of the input shaking in that frequency range is small from the beginning and the difference in the acceleration ratio for the high-frequency range has less impact on the settlement behavior of the structure for liquefaction-related problems. The spiky behavior in the later stage of shaking

is caused by the soil dilation and re-stiffening mechanism of the Model.
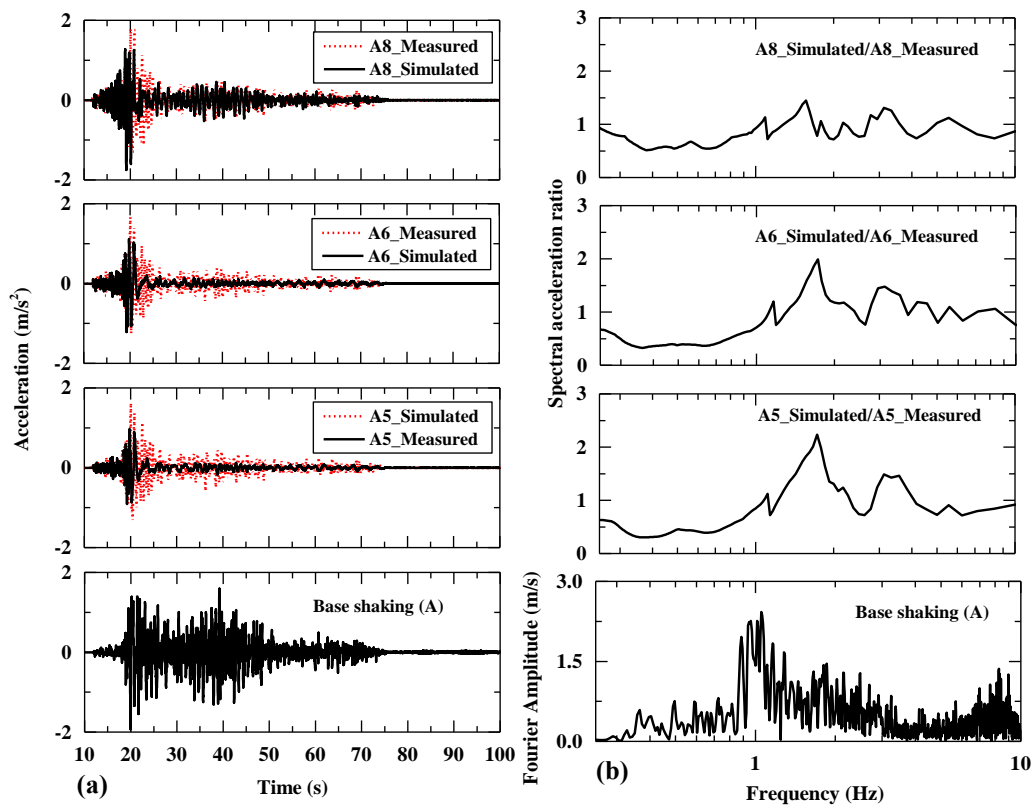
Fig. 2.10. Acceleration response (a) measured and simulated acceleration time histories during Tokachi-Oki ground motion and (b) computed spectral acceleration ratio and Fourier spectrum of applied base shaking

The simulated and measured displacement time histories of the footing are compared in Fig. 2.11. The simulated rate of the vertical displacement of the footing before 40 s is relatively large in comparison with the measured rate in the centrifuge model test. The settlement progression after shaking is evident for the case of the measured footing settlement, whereas the numerical model does not show such a tendency. The shear-induced settlement and the settlement caused by reconsolidation strains due to simultaneous partial drainage govern the overall evolution of the footing settlement and tilt measured in the centrifuge model test. However, the numerical model seems to overestimate the shear-induced settlement and significantly underestimate the settlement caused by reconsolidation. Several researchers have made similar observations, e.g., Taibet et al. (2007), Dashti and Bray (2013), and Karimi and Dashti (2015, 2016). The numerical models typically exhibit limitations in capturing the

settlement caused by partial drainage and reconsolidation during and after shaking because of the characteristics of their constitutive formulations, as reported by Shahir et al. (2012), Boulanger and Ziotopoulou (2017), Karimi and Dashti (2016), and Adamidis and Madabhushi (2019). In general, it can be said that the simulated displacement time histories are comparable to the measured ones. In addition, the numerical model can capture the total settlement and the tilt of the footing at the end of the shaking, which is further used for the stochastic investigation.
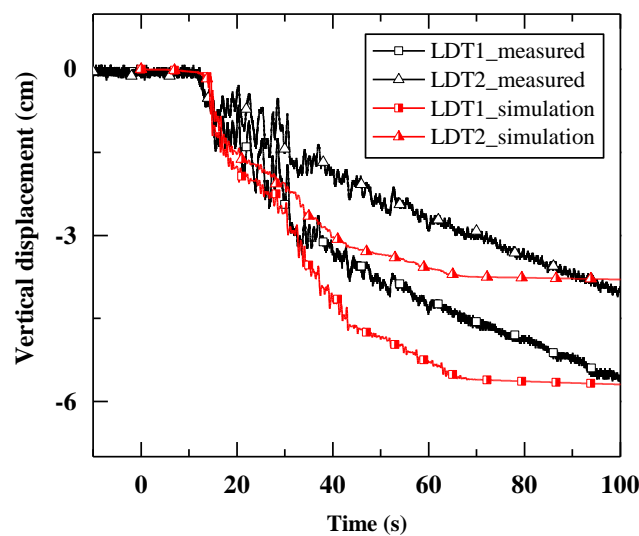
Fig. 2.11. Measured and simulated footing settlement during Tokachi-Oki ground motion

2.3 Stochastic model

Several researchers have attempted to obtain the soil's spatial nonuniformity in the centrifuge model ground. For example, Bolton et al. (1999) used an in-flight cone penetration test at 70g to obtain insight into the model's spatial nonuniformity. They reported that the nonuniformity in the model ground (in terms of tip resistance, void ratio, and normalized cone resistance) might vary with the coefficient of variation (COV) of 2 to 15% with correlation length as low as 0.2 m in the vertical direction under a controlled environment. The image processing technique was used by White et al. (2003) based on particle image velocimetry (PIV) and close-range photogrammetry. They found the COV of dry density in the range of 1 to 8%. A high-resolution needle probe technique was adopted by Li et al. (2005) to trace the spatial nonuniformity of the centrifuge model ground. They observed the COV of porosity for loose sand and medium dense sand in the range of 1 to 4% and 1 to 6%, respectively. For a conceptual

understanding of risk and reliability analyses in geotechnical engineering, readers are suggested to read Christian et al. (1994) and Phoon and Ching (2014).

The pouring rate and falling height of Toyoura sand and the pouring direction of the sand hopper are the primary sources of uniformity in the centrifuge model. In addition, the size of the model container is limited and a nonuniform model ground along the container boundaries is inevitable. The random field approach (details can be found in Popescu and Prevost, 1995; Zhang et al., 2008) is adopted to estimate the COV and correlation lengths used in this chapter considering the random sampling error, effects of container size, and invariability due to method of preparation of the model ground. The estimated COV and the correlation length in the vertical direction are found in the range of 1 to 6% and 0.5 m to 1.0 m, respectively for the centrifuge experiments at 40g. The estimated correlation length in the horizontal direction is found in the range of 2 m to 6 m. This also reflects the observation of Phoon and Kulhawy (1999) and Phoon and Ching (2014), which suggests that the correlation length in the horizontal direction is often within an order of magnitude (10 times) larger than the correlation length in the vertical direction. Different combinations of COV and correlation lengths are considered to trace the average effects of nonuniformity in the centrifuge model, as recommended by Zhang et al. (2008). The nonuniformity in the centrifuge model is evaluated in model scale. However, units in the prototype scale are used in the presented chapter to ensure consistency.

The nonuniform relative density within the centrifuge model ground is mapped using the overburden and energy-corrected, equivalent clean sand, SPT $(N1)_{60cs}$ values as suggested by Montgomery and Boulanger (2016). A series of two-dimensional stochastic dynamic analyses are performed considering the centrifuge model ground properties based on anisotropic, spatially correlated Gaussian random fields of $(N1)_{60cs}$ values. A Gaussian correlation function is used, and the random field is generated through LU decomposition of the covariance matrix as per Constantine and Wang (2012). The PM4Sand model has three primary input parameters (D_R, G_0, h_{po}), which can be calibrated (along with the secondary input parameters) per the randomly generated $(N1)_{60cs}$ values. For a given $(N1)_{60cs}$ value, the relative density (D_R) and parameter G_0 are computed as follows:

$$D_R = \sqrt{\frac{(N1)_{60cs}}{46}} \tag{2.1}$$

$$G_0 = \left(\frac{G_{max}}{P_A}\right)\left(\frac{P_A}{P'}\right)^{0.5} \tag{2.2}$$

where $P' =$ the mean effective stress and $P_A =$ the atmospheric pressure. The value of G_{max} is computed using the correlation proposed by Andrus and Stoke (2000) for a soil shear wave velocity (V_s) with a slight modification (Montgomery and Boulanger, 2016) as follows:

$$G_{max} = \rho(V_s)^2 \tag{2.3}$$

$$V_s = 85[(N1)_{60cs} + 2.5]^{0.25} \left(\frac{P'}{P_A}\right)^{0.25} \tag{2.4}$$

where ρ is the mass density of the ground, which is assigned a uniform value of 1.92 ton/m³ in the present study. The whole model ground is assigned a uniform permeability value of 0.0002 m/s. The last primary input parameter (h_{po}) is calibrated to achieve a single-amplitude shear strain of 3% during cyclic undrained simple shear loading with an initial static shear stress ratio of zero on a horizontal plane at the single element level. The random field of $(N1)_{60cs}$ values with calibrated parameters of the PM4Sand model are implemented into the OpenSees numerical model with the help of MATLAB code. Eighteen different cases of nonuniformity in the centrifuge model are considered as tabulated in Table 2.5, and a total of forty realizations are generated for each of the cases. The number of realizations is determined based on the convergence of the mean and standard deviation of the average footing settlement and tilt. All the cases have a mean value of $(N1)_{60cs} = 12$ ($D_R \sim 50\%$) with different combinations of nonuniformity in the centrifuge model. The tabulated coefficient of variation (COV) and scale of fluctuation (θ_x and θ_y) are considered according to Bolton et al. (1999), White et al. (2003), Li et al. (2005), and Zhang et al. (2008) as described earlier.
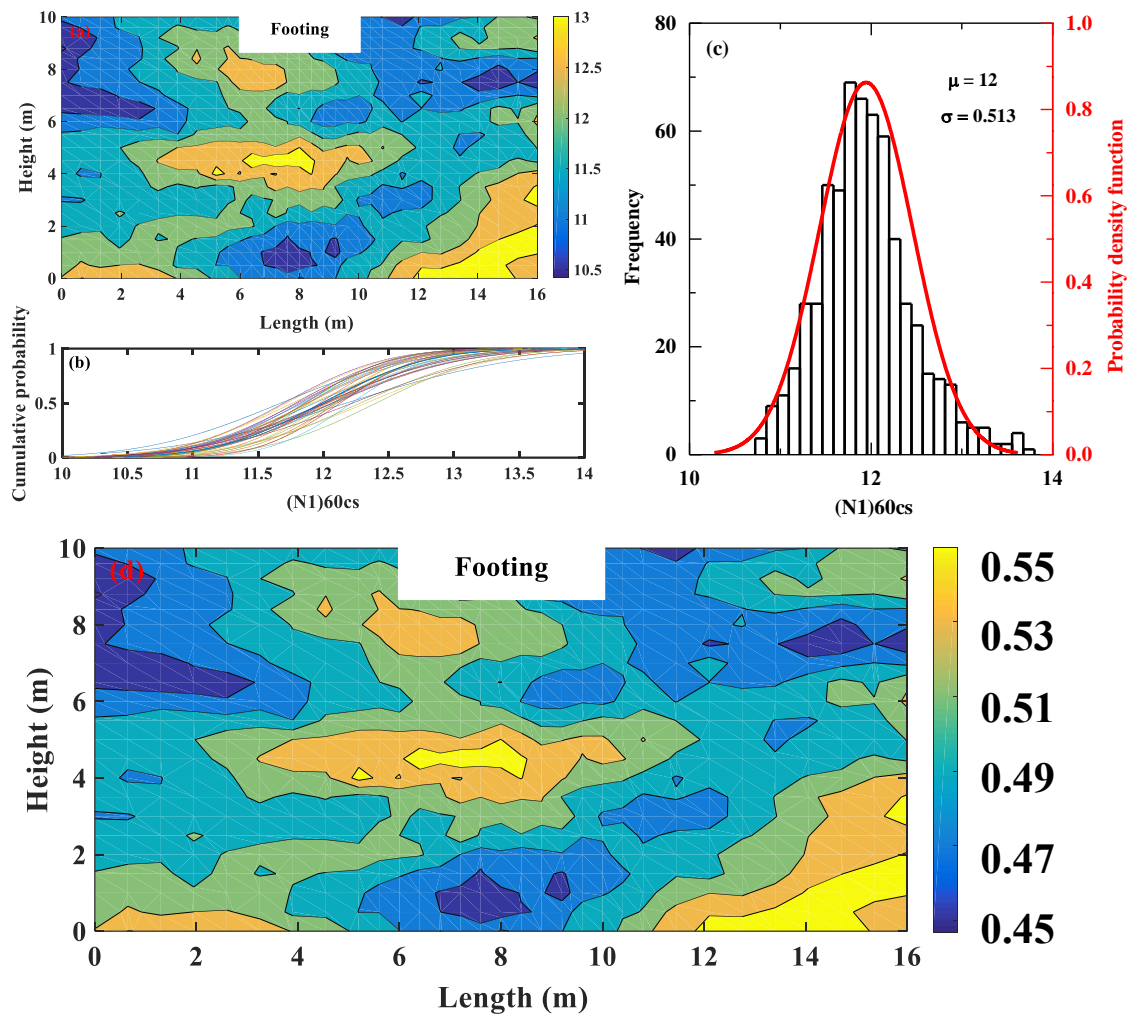
Fig. 2.12. Simulation of nonuniformity in the centrifuge model in terms of the overburden and energy-corrected, equivalent clean sand, SPT $(N1)_{60cs}$: (a) typical random field realization in SPT $(N1)_{60cs}$, (b) cumulative probability of forty realizations, (c) typical stochastic distribution of the generated random field with a fitted probability density function, and (d) typical random field realization in relative density

A typical spatial distribution of $(N1)_{60cs}$ values for COV = 6%, $\theta_x = 2$ m, and $\theta_y = 1$ m for mapping the nonuniformity in the centrifuge model is shown in Fig. 2.12. Fig 2.12(a) shows the contours of the $(N1)_{60cs}$ values within the model ground for a typical realization. The cumulative probability distributions of all forty realizations are shown in Fig. 2.12(b). The values of $(N1)_{60cs}$ vary between 10 and 14 for all realizations with different probabilities of occurrence. Fig. 2.12(c) shows that the generated spatial distribution of the $(N1)_{60cs}$ values can be fitted with a Gaussian normal distribution with a specified mean (μ) and standard deviation

(σ). Fig. 2.13 shows the typical variation of the mean and standard deviation of the average footing settlement ((LDT1+LDT2)/2) and tilt ((LDT1-LDT2)/W; W = the width of the footing). The mean and standard deviation become stable within forty realizations, and hence, a reliable statistical interpretation of the stochastic data can be obtained from the series of nonlinear dynamic numerical simulations. It should be noted that the greater the number of realizations, the better the reliability of the statistical interpretation. However, the numerical computational expense should be taken into account when selecting the total number of realizations without compromising the stability of the mean and standard deviation of the primary stochastic outcome (e.g., the average settlement and tilt of the footing presented in this chapter).
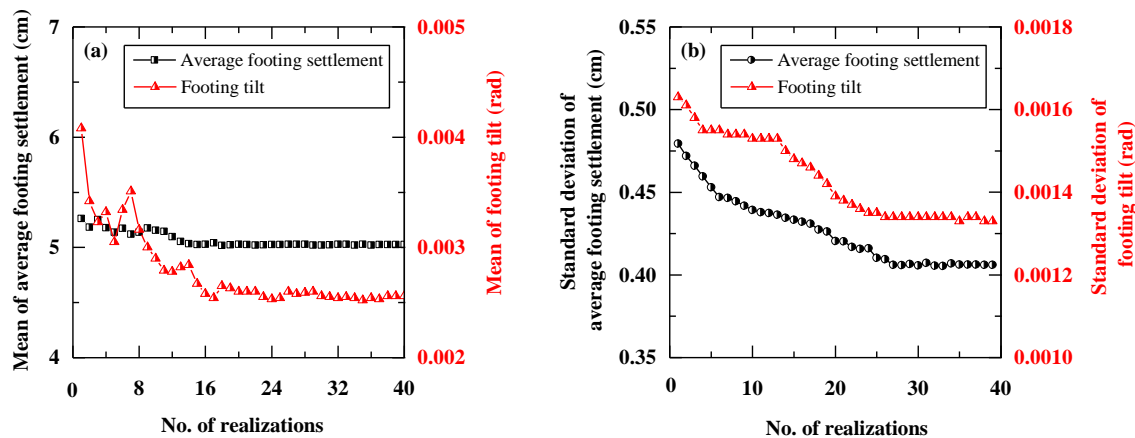
Fig. 2.13. Typical convergence checks for a total of forty realizations (for COV = 6%, θx = 4 m, and θy = 0.5 m): (a) stability of the mean of the average settlement and tilt of the footing, and (b) stability of the standard deviation of the average settlement and tilt of the footing

2.4 Results and discussion

2.4.1 *Average settlement and tilt of footing*

Two–dimensional stochastic analysis results are presented and compared with the deterministic analysis results at the prototype scale. In the case of deterministic analysis, uniform model ground is assumed with $(N1)_{60cs}$ = 12 (D_R ~50%). The deterministic analysis is initially validated with a dynamic centrifuge model test, as explained earlier. Fig. 2.14 illustrates the stochastic distribution of the average footing settlement for different combinations of

nonuniformity in the centrifuge model. The average footing settlement is calculated by taking the average of the readings of LDTs 1 and 2 at the end of the shaking. The mean (μ) and the standard deviation (σ) of the average footing settlement are found in the ranges of 4.90 cm to 5.12 cm and 0.294 cm to 0.508 cm, respectively. It is evident that the mean values of stochastic average footing settlement for different combinations of nonuniformity in the centrifuge model (as tabulated in Table 2.5) are comparable to the deterministic values of the average footing settlement. However, a relatively wide range of standard deviations cannot be ignored, and the implications of the atypical distributions of the average footing settlement (as shown in Fig. 2.14) are subsequently discussed with the help of Fig. 2.16.

Fig. 2.15 shows the stochastic distribution of the footing tilt for different combinations of nonuniformity in the centrifuge model. The footing tilt is calculated using the readings of LDTs 1 and 2 as (LDT1 - LDT2)/4.0 (the width of the footing is 4.0 m) at the end of the shaking. The mean (μ) and the standard deviation (σ) of the footing tilt are found in the range of 0.0021 rad to 0.0029 rad and 0.0011 rad to 0.0023 rad, respectively. It is evident that the mean stochastic footing tilt for different combinations of nonuniformity in the centrifuge model is significantly larger than the deterministic value of the footing tilt. This notable difference (with a maximum value of 0.0029 − 0.0013 = 0.0016 rad, which is even more than the deterministic value of 0.0013 rad) in the stochastic mean and deterministic value of the footing tilt suggests that the nonuniformity in the centrifuge model has a significant impact on the tilt of the footing. It should be noted that all of the stochastic distributions of the footing tilt with different combinations of centrifuge model nonuniformity are positively skewed from the deterministic value of the footing tilt, as shown in Fig. 2.15. This emphasizes that the deterministic numerical simulation (with uniform ground properties) substantially underestimates the tilt of the footing.

The observations from Figs. 2.14 and 2.15 echo the general notion that the deterministic analyses underestimate the settlement and tilt of the footing. However, the probability of their occurrence must be determined, as shown in Fig. 2.16. The probability of deviation of the stochastic average footing settlement and tilt from their deterministic values are evaluated and presented in Fig. 2.16 for different combinations of non-uniformity in the centrifuge model. The deviations of the average footing settlement and tilt are considered on the positive side (more than the deterministic value) and negative side (less than the deterministic value). The maximum deviation of the average footing settlement and footing tilt determined from their

deterministic values, along with the associated probability of the occurrence, are tabulated in Table 2.6 for the ease of interpreting Fig. 2.16.

Table 2.5. Different combinations of nonuniformity in the centrifuge model

Case	Mean (μ), $(N1)_{60cs}$	COV (%)	θ_x (m)	θ_y (m)
A	12	2	2	0.5
B	12	2	4	0.5
C	12	2	6	0.5
D	12	2	2	1
E	12	2	4	1
F	12	2	6	1
G	12	4	2	0.5
H	12	4	4	0.5
I	12	4	6	0.5
J	12	4	2	1
K	12	4	4	1
L	12	4	6	1
M	12	6	2	0.5
N	12	6	4	0.5
O	12	6	6	0.5
P	12	6	2	1
Q	12	6	4	1
R	12	6	6	1
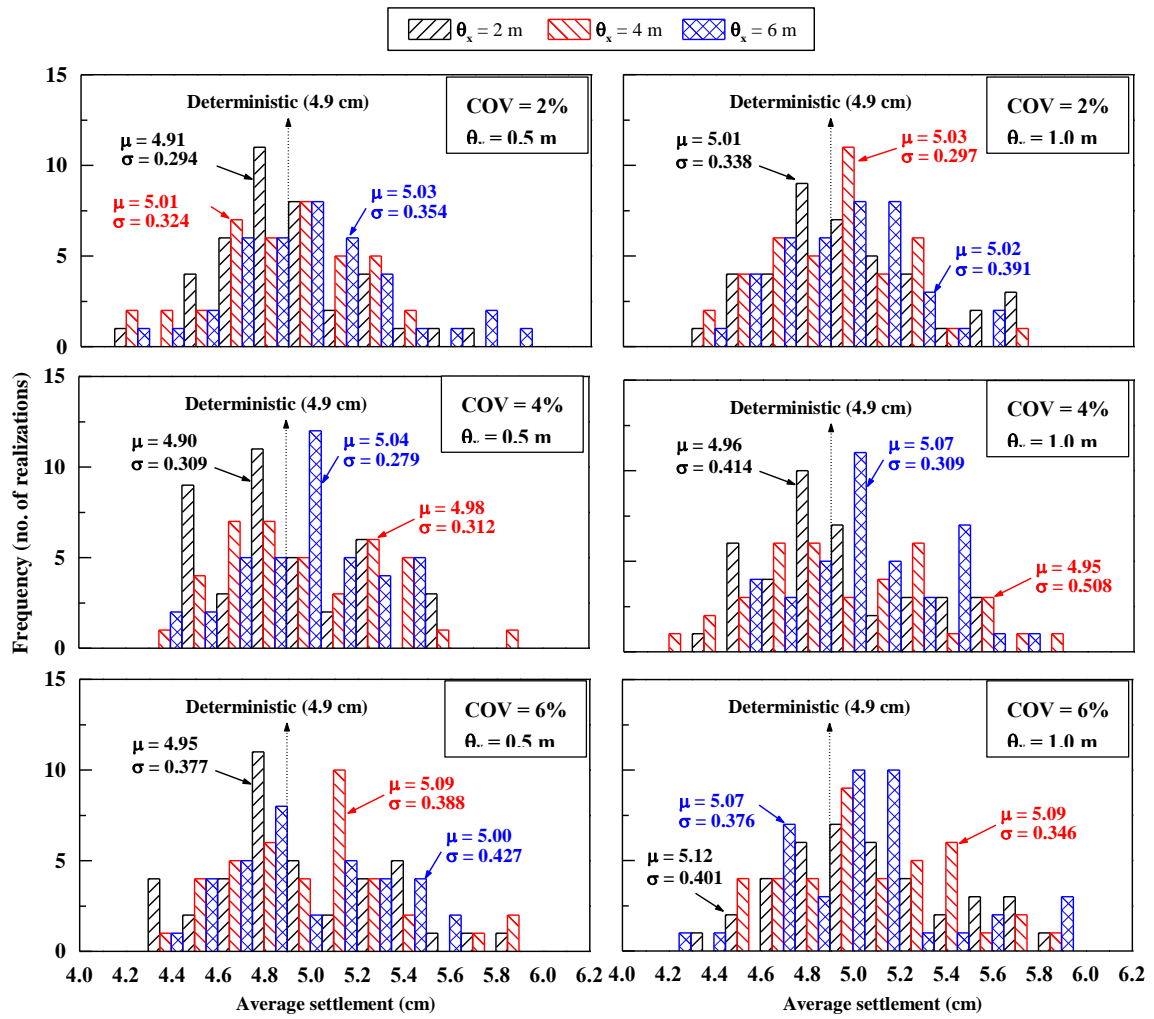
Fig. 2.14. Stochastic distributions of the average footing settlement for different combinations of nonuniformity in the centrifuge model
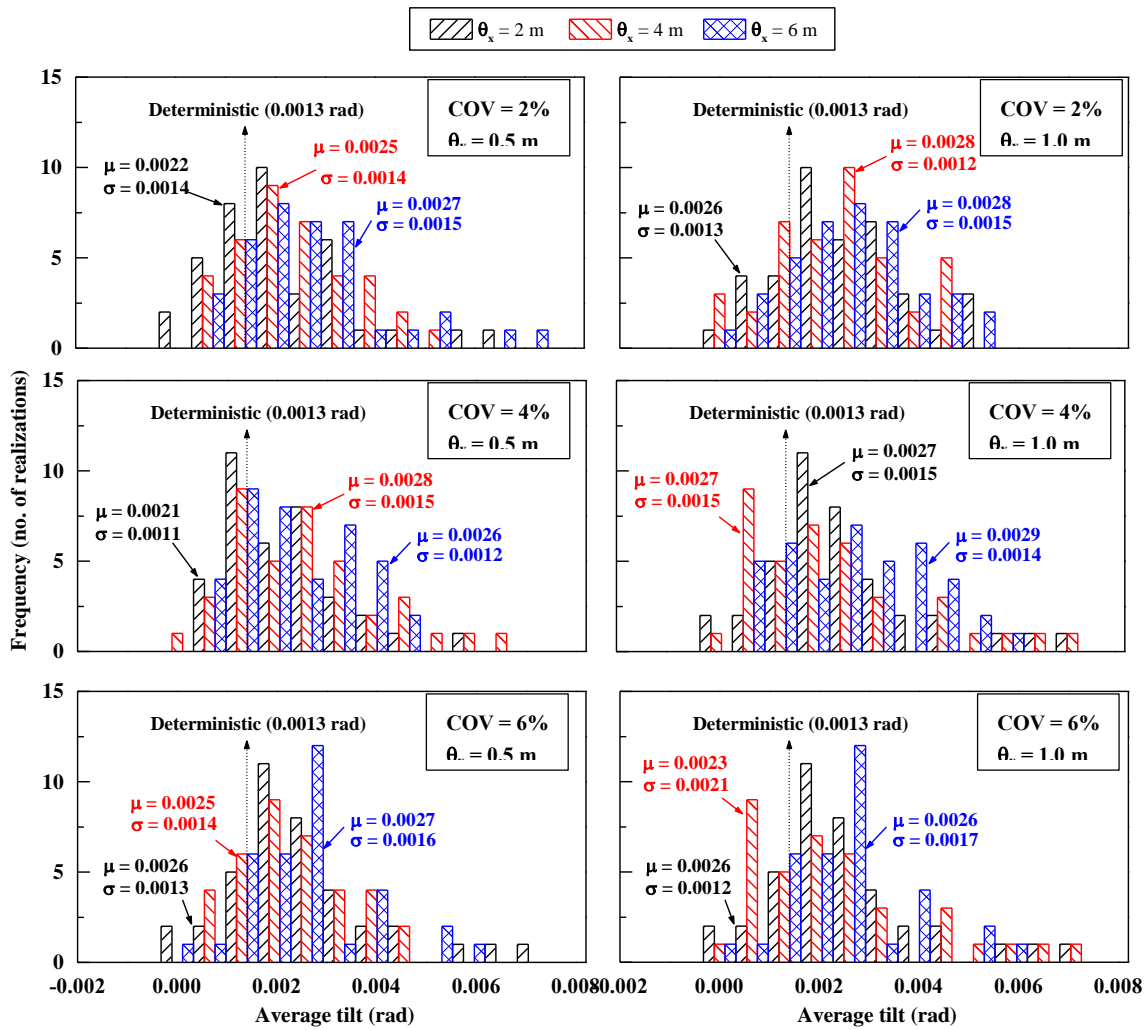
Fig. 2.15. Stochastic distributions of the footing tilt for different combinations of nonuniformity in the centrifuge model
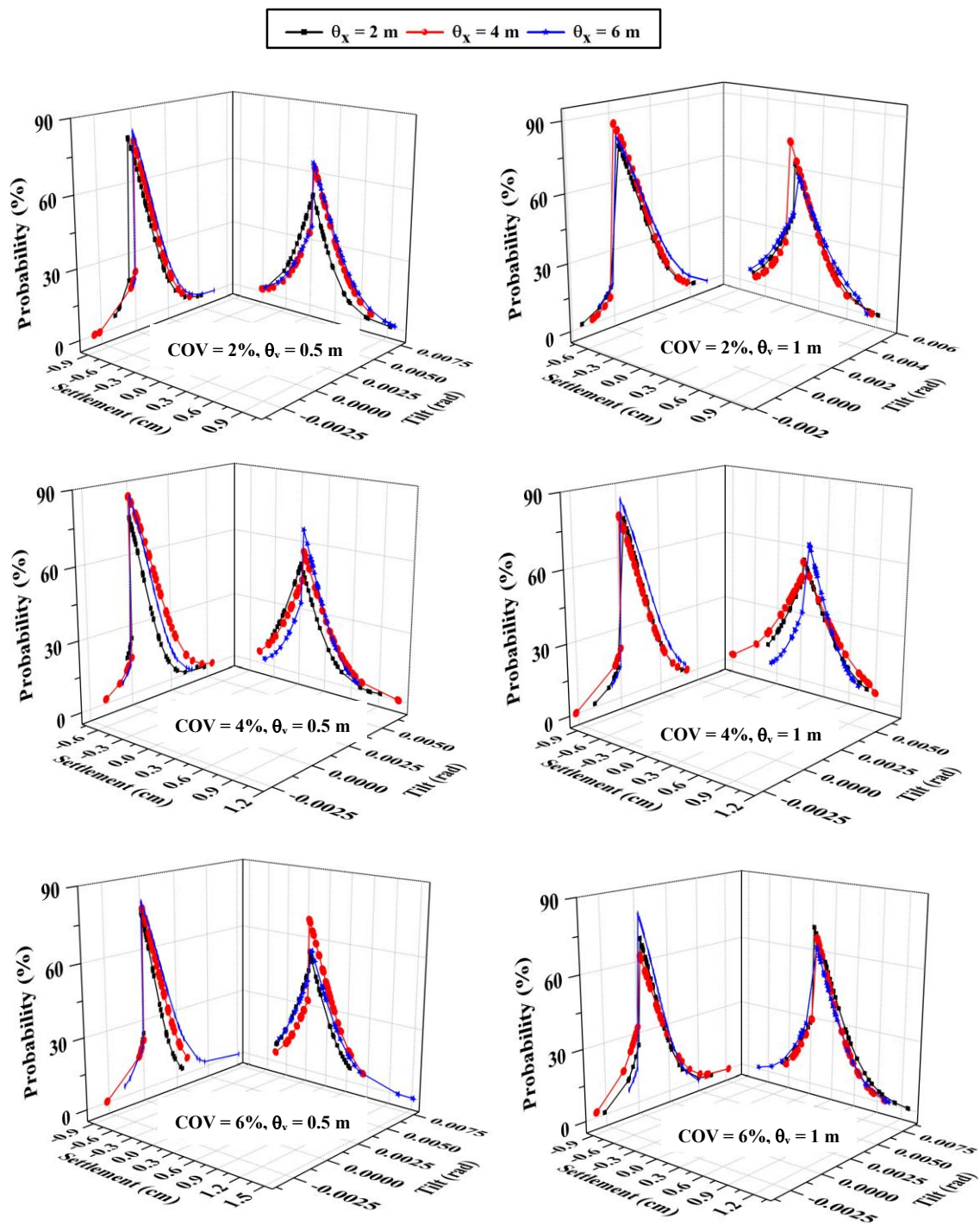
Fig. 2.16. Probability of the deviation of the average settlement and tilt of the footing from their deterministic values for different combinations of nonuniformity in the centrifuge model (the maximum deviation of the average footing settlement and footing tilt from their deterministic values along with their probability of occurrence are tabulated in Table 2.6

Table 2.6. The probability of deviation of the stochastic average footing settlement and tilt from their deterministic values. A few numbers extracted from Fig. 2.16 are tabulated in this table

Different combinations of non-uniformity in the centrifuge model$^\$$	Probability of exceedance of average footing settlement and tilt in negative side (less than the deterministic value) and positive side (more than the deterministic value)							
	Average footing settlement				Footing tilt			
	Negative* side (cm)	Probability (%)	Positive** side (cm)	Probability (%)	Negative* side (rad)	Probability (%)	Positive** side (rad)	Probability (%)
COV = 2%, θ_y = 0.5 m θ_x = 2 m, 4 m, and 6 m	-ve -0.60	38.21 1.18	+ve 0.97	61.79 0.87	-ve -0.0029	19.54 0.17	+ve 0.0063	80.46 0.05
COV = 4%, θ_y = 0.5 m θ_x = 2 m, 4 m, and 6 m	-ve -0.48	34.84 5.39	+ve 1.10	65.16 0.19	-ve -0.0016	16.27 1.80	+ve 0.0053	83.73 0.48
COV = 6%, θ_y = 0.5 m θ_x = 2 m, 4 m, and 6 m	-ve -0.47	32.40 4.37	+ve 1.51	67.60 0.04	-ve -0.0026	20.68 0.37	+ve 0.0076	79.32 0.01
COV = 2%, θ_y = 1.0 m θ_x = 2 m, 4 m, and 6 m	-ve -0.48	28.06 6.31	+ve 0.91	70.94 0.92	-ve -0.0017	14.84 1.49	+ve 0.0050	85.16 0.01
COV = 4%, θ_y = 1.0 m θ_x = 2 m, 4 m, and 6 m	-ve -0.90	39.20 3.04	+ve 0.90	60.80 2.96	-ve -0.0026	17.00 0.37	+ve 0.0043	83.00 1.57
COV = 6%, θ_y = 1.0 m θ_x = 2 m, 4 m, and 6 m	-ve -0.74	30.26 0.77	+ve 1.27	69.74 0.44	-ve -0.0032	20.71 2.20	+ve 0.0077	79.30 0.06

$\$$ Maximum values among θ_x = 2 m, 4 m, and 6 m are tabulated in this table
* -ve is less than the deterministic value
** +ve is more than the deterministic value

The probability of the average footing settlement being less than the deterministic value is found in the range of 28.06 to 39.20%. The maximum deviation of the average footing settlement on the negative side is found in the range of 0.47 cm (with a 4.37% probability of occurrence) to 0.90 cm (with a 3.04% probability of occurrence). However, the probability of the average footing settlement being more than the deterministic value is found in the range of 60.80 to 70.94%. The maximum deviation of the average footing settlement on the positive side is found in the range of 0.90 cm (with a 2.96% probability of occurrence) to 1.51 cm (with a 0.04% probability of occurrence). The probability of the footing tilt being less than the deterministic value is found in the range of 14.84 to 20.71%. The maximum deviation of the footing tilt in the negative side is found in the range of 0.0016 rad (with a 1.80% probability of occurrence) to 0.0032 rad (with a 2.20% probability of occurrence). However, the probability

of the footing tilt being more than the deterministic value is found in the range of 70.30 to 85.16%. The maximum deviation of the footing tilt in the positive side is found in the range of 0.0043 rad (with a 1.57% probability of occurrence) to 0.0077 rad (with a 0.06% probability of occurrence). These statistics signify that unlike the average footing settlement, the footing tilt is prone to have a significant deviation from the deterministic value with a relatively large probability of occurrence.

2.4.2 *Expected error*

The numerical model is an idealized abstraction of the centrifuge model. Hence, the model uncertainty may affect the reliability of stochastic analyses (Zhang et al., 2009). A non-dimensional (normalized) root-mean-square error is calculated for the average settlement and tilt of the footing to trace the severity of the error induced due to model uncertainty under the assumption of the random sampling of nonuniformity as reported by Popescu and Prevost (1995). The expected error (ε_n) for random realizations can be calculated as follows:

$$\varepsilon_n = \frac{\sigma_n}{\mu_n \sqrt{n}} \tag{2.5}$$

where σ_n and μ_n are the standard deviation and mean of the stochastic average settlement and tilt of the footing, respectively, for n realizations.

Fig. 2.17 shows the expected error magnitude in the estimation of the average settlement and tilt of the footing for different combinations of nonuniformity in the centrifuge model. The expected error is compared with the maximum allowable error ($\varepsilon_{max} = 0.35/\sqrt{n} = 0.055$, for n = 40 realizations, Popescu and Prevost, 1995). A scattered trend in expected when the error magnitude is observed until 15 and 20 realizations for the average settlement and tilt of the footing, respectively. It is evident that the expected error magnitude is significantly large for fewer realizations (n <10). The footing tilt is prone to have a large expected error magnitude in comparison with the average footing settlement. The observed trends of the expected error magnitude are consistent with those reported by Popescu and Prevost (1995) and Popescu et al., 2004. The expected error magnitude decreases with increasing number of realizations, having a notable margin from the maximum allowable error for a total of forty realizations. This also confirms that forty realizations are sufficient for the reliable statistical interpretation of stochastic data.
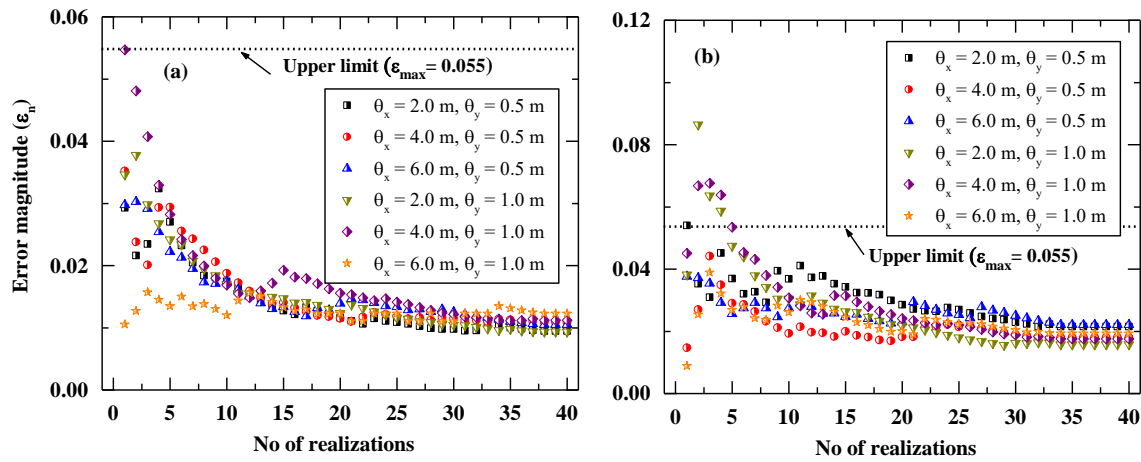
Fig. 2.17. Expected error magnitude for different combinations of nonuniformity in the centrifuge model (average values for COV = 2, 4, and 6%): (a) average footing settlement and (b) footing tilt

2.4.3 Displacement response spectra

The displacement time history of the input motion (Tokachi-Oki) is applied at the base of the numerical model. The frequency and magnitude of the input shaking fluctuate (amplify or attenuate depending upon the soil-structure interaction) as the wave propagates toward the surface of the ground. The response of the superstructure significantly depends on the characteristics of the shaking at the foundation. An attempt is made to understand the stochastic response of the foundation-structure system in terms of the spectral displacement for different combinations of nonuniformity in the centrifuge model. For each realization, the displacement time history of the footing is recorded during shaking. Then, the spectral displacement (horizontal) is calculated for a wide range of fundamental periods (T = 0.0005 - 4 s), considering a damping ratio of 5%. A liquefied ground usually filters the high-frequency content of the incident wave while amplifying the magnitude of the low-frequency content. The amplification in the magnitude of the low-frequency content of the incident wave has a significant impact on the spectral displacement of the foundation-structure system.

Fig. 2.18(a) depicts the mean spectral horizontal displacement of the footing against a wide range of fundamental periods along with the mean (μ) +/- standard deviation (σ) trends. It is found that the spectral displacement starts to deviate from its mean value for periods of

more than 0.7 s. This emphasizes that the consideration of nonuniformity in the centrifuge model is essential for structures with long fundamental periods. A total of forty realizations are carried out for each case of nonuniformity in the centrifuge model, as discussed earlier. The spectral displacement corresponding to each realization for long periods, T = 2, 3, and 4 s (for the sake of brevity, only three periods are selected) is used to exhibit the stochastic distributions of the spectral displacement as shown in Fig. 2.18(b). The spectral displacement significantly deviates from its mean value with a significant standard deviation. This emphasizes that the consideration of nonuniformity in the centrifuge model is vital to evaluate the seismic behavior of the foundation-structure system.
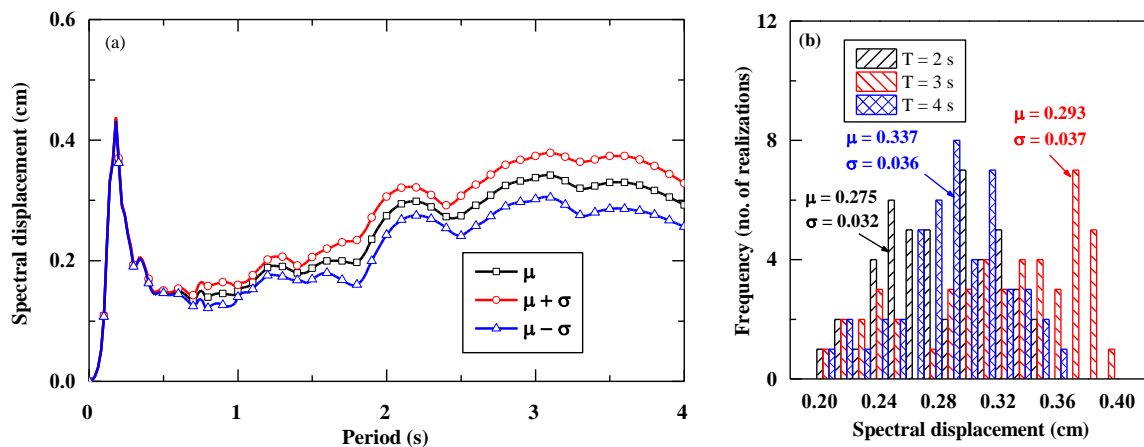
Fig. 2.18. Response of the foundation-structure system for a typical case of nonuniformity in the centrifuge model (COV = 6%, θx = 4 m, and θy = 0.5 m): (a) horizontal spectral displacement with mean (μ) +/- standard deviation (σ) and (b) distributions of the spectral displacement at periods of 2, 3, and 4 s

2.4.4 *Liquefaction potential index*

An attempt is made to evaluate the severity of the liquefaction-induced impact on the foundation-structure system in correlation with the average footing settlement and tilt for different combinations of nonuniformity in the centrifuge model. A liquefaction potential index (I_L) is calculated per Iwasaki et al. (1982) and Sonmez and Gokceoglu (2005) with a slight modification as follows:

$$I_L = \int_0^Z F(10 - 0.5Z)dz, \ Z \ \leq 20 \ m \tag{2.6}$$

where Z is the depth of the ground (= 10 m in this study), and F is defined as the ratio of the area of the liquefied elements and the total area of the elements under the footing at a depth of Z. An element (mesh is shown in Fig. 2.7) is considered to be liquefied if the excess pore pressure ratio is more than or equal to 0.9. The excess pore pressure ratio (r_u) is defined as the ratio of the excess pore pressure to the initial vertical effective stress. In the original liquefaction potential index (Iwasaki et al., 1982), F is the factor of safety against liquefaction defined as FL. Since FL cannot be obtained explicitly from the calculation, it is replaced with the proportion of the liquefied soil in this chapter.

Fig. 2.19(a) shows that the mean and the standard deviation of I_L (for a typical case of nonuniformity in the centrifuge model with COV = 6%, θ_x = 4 m, and θ_y = 0.5 m) become stable within forty realizations; hence, a reliable statistical interpretation of the impact of the severity of ground liquefaction on the behavior of the foundation-structure system can be made. Figs. 2.19(b-c) show the stochastic correlation between I_L and the average footing settlement and the tilt. Nearly 90% of the I_L values are found in the range of 8 to 18, corresponding to an average footing settlement in the range of 4.28 cm to 5.46 cm with a few (~10%) scattered values in the range of 18 to 28. However, nearly 87% of the I_L values are found in the range of 8 to 18, corresponding to a footing tilt in the range of 0.0010 rad to 0.0052 rad, with a few (~13%) scattered values in the range of 18 to 28.

Fig. 2.20 shows the overall range of the average settlement and tilt of the footing with a 95% confidence level considering the different combinations of nonuniformity in the centrifuge model. It can be observed that the stochastic mean values of average footing settlement for different combinations of nonuniformity in the centrifuge model are comparable to the deterministic values. However, the 95% confidence range of the footing tilt significantly deviates from its deterministic value. This observation signifies that the deterministic numerical simulation (with uniform ground properties) substantially underestimates the tilt of the footing, and the footing tilt is prone to be severely affected by the nonuniformity in the centrifuge model.
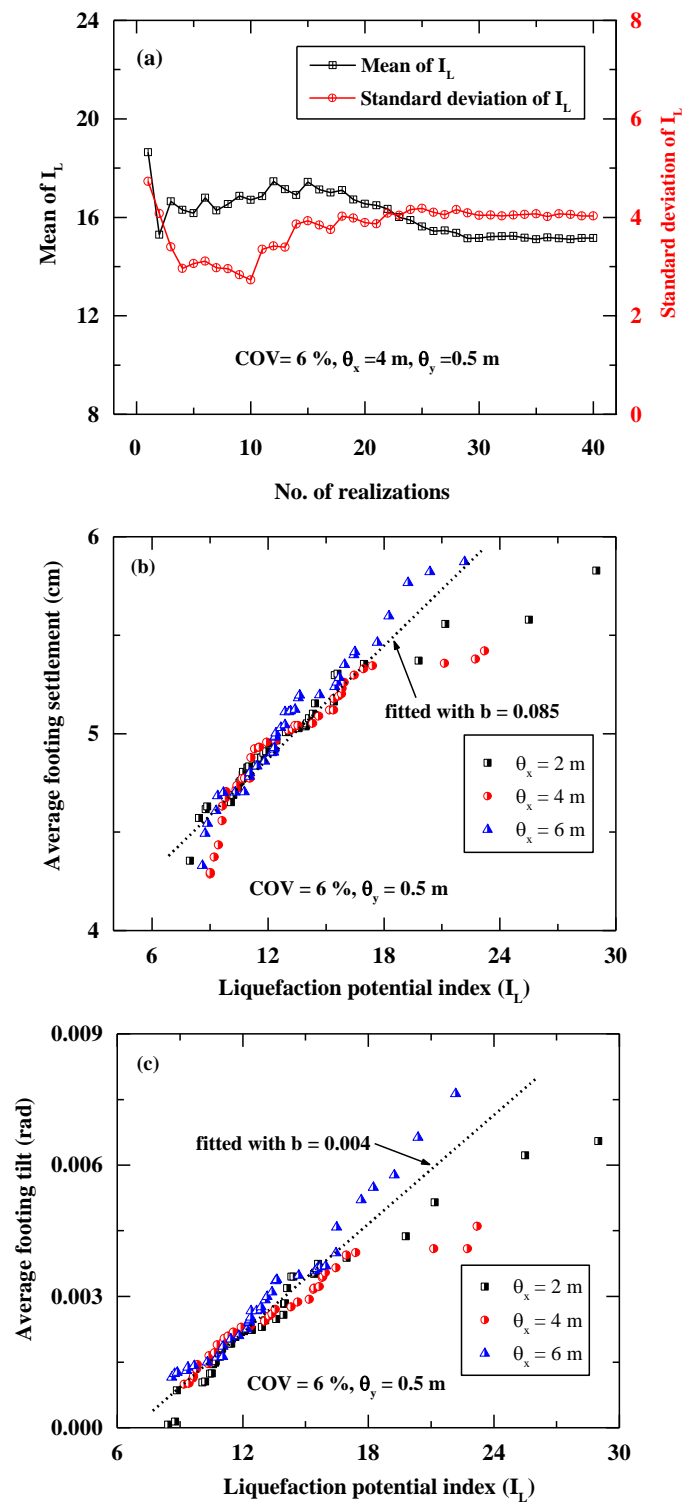
Fig. 2.19. Liquefaction severity and the response of the foundation-structure system: (a) a typical convergence check for the liquefaction potential index (I_L), (b) correlation between the

average footing settlement and I_L, and (c) correlation between the footing tilt and I_L
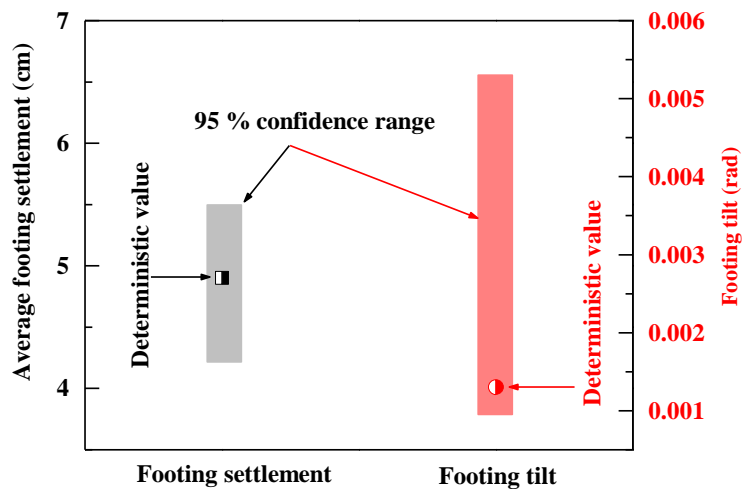
Fig. 2.20. Stochastic range (with 95% confidence level) of the average settlement and tilt of the footing

2.5 Summary

Liquefaction-induced effects on shallow foundation, presumably resting on a uniform deposit of liquefiable ground is investigated using the centrifuge lab facility. The centrifuge model contains two shallow foundations and associated superstructures, namely, buffer tank (BT, 4x4x1 m3) and flare stack (FS, 4x4x2 m3), imposing average bearing pressures of 51.2 kPa and 71.2 kPa, respectively, at 0.8 m below the surface of the model ground at the prototype scale. Centrifuge test depicted that the shallow foundations undergo severe deformation during strong ground motion. A reliability assessment of the physical modeling of liquefaction-induced effects on shallow foundations considering nonuniformity in the centrifuge model is carried out using two-dimensional (2D) stochastic numerical analyses. The numerical modeling scheme is validated at the element level and at the system level by simulating the centrifuge model test, which is performed to investigate the liquefaction-induced effects on the shallow foundation. The PM4Sand elastoplastic soil constitutive model is used to simulate the dynamic behavior of the liquefiable model ground. The nonuniformity in the centrifuge model is mapped with the stochastic realizations of the overburden and energy-corrected, equivalent clean sand, SPT $(N1)_{60cs}$ values using a spatially correlated Gaussian random field. The nonuniformity in the

centrifuge model is found to influence the engineering judgment made from the centrifuge model test for various types of problems, such as the average footing settlement and tilt, liquefaction severity of the ground, and implications of the ground-foundation-structure interaction. The stochastic average footing settlements with different combinations of centrifuge model nonuniformity are comparable to the deterministic average footing settlements. However, the nonuniformity in the centrifuge model is found to have a significant impact on the tilt of the footing. It is observed that the deterministic numerical simulation (having uniform ground properties) significantly underestimates the tilt of the footing. Stochastic results also indicated that the liquefaction extent in the model ground varies with the centrifuge model's nonuniformity and is correlated with the effects on the foundation-structure system. The stochastic displacement spectra exhibited that the nonuniformity of the centrifuge model ground should be taken into account, especially for long-period structures. The reliability assessment of the centrifuge model test results is essential for better engineering judgment associated with a desired level of confidence. The presented probabilistic correlations between nonuniformity of the centrifuge model and the response of foundation-structure system possess significant practical importance and provides useful information to assess the reliability of the physical model tests by numerical procedure. The presented work considers the scale of fluctuation which corresponds to the physical distance over which there is a correlation in the relative density of the centrifuge model ground. However, for a generalized interpretation of the reliability of the centrifuge test with respect to the configuration of the foundations and size of the centrifuge model, it is advised to consider the normalized correlation length with respect to the footing width as suggested by Griffiths et al. (2002). For a generalized framework to incorporate the reduction in the epistemic uncertainty, it is necessary to further investigate different scenarios of the applied shaking, foundation-structure system, depth of the water table, and ground conditions.

Chapter 3. Centrifuge modeling of induced partial saturation

Induced partial saturation is one of the novel techniques to increase the liquefaction resistance of the saturated sandy ground. The effectiveness of air voids under strong shaking, compressibility of air-fluid mixture, partial drainage effects on the evolution of excess pore water pressure (EPWP), post-liquefaction behavior and inertial and kinematic interaction of soil-foundation-structure system are essential to assimilate the maximum benefits of this technique. For that purpose, two dynamic centrifuge experiments (typical model layout is shown in Fig. 3.1) are carried out to examine the performance of induced partial saturation to mitigate the liquefaction effects on shallow foundation.

3.1 Modeling of induced partial saturation

Model ground preparation for centrifuge test and description of foundation-structure systems is described in Chapter 2. The index properties of model ground (Toyoura sand) and configuration of foundation structure system (see Fig. 3.1) are tabulated in Tables 2.2 and 2.4, respectively. The drainage-recharge method is used to prepare the partially saturated model ground. The preparation method for fully saturated and partially saturated model ground is shown in Fig. 3.2. To prepare the partially saturated ground, initially the Metolose solution is drained out from the saturated model ground which turns the model into moist state and entrapped some amount of the air voids inside it. Then, the drained-out Metolose solution is dripped back slowly on the sponges at the surface of the model ground in open air. The recharging is continued until the water table reaches back to the top surface of the model ground. It is to be noted that this time some amount of Metolose solution is left out because of entrapped air even though the water table reaches up to the top surface. This process is repeated three times to ensure the uniformity of air voids entrapped within the model ground. Each time it took almost 4 hours to complete the drainage-recharge cycle. The overall degree of saturation within the partially saturated model ground is estimated by W_2/W_1, where W_2 and W_1 are the amounts of Metolose solution used in preparing the partially saturated and fully saturated model ground respectively. Due

care is taken to estimate the degree of saturation for both fully saturated and partially saturated model grounds using mass, volume and densities relationships. However, it is worth noting that certain errors still happen to have a scope as mentioned by Kutter (2013). The degree of saturation for fully saturated and partially saturated are 99.1 and 88.4%, respectively. The location of the water table is estimated using pore pressure readings of many pore pressure transducers at 40g to avoid/minimize any possible error.
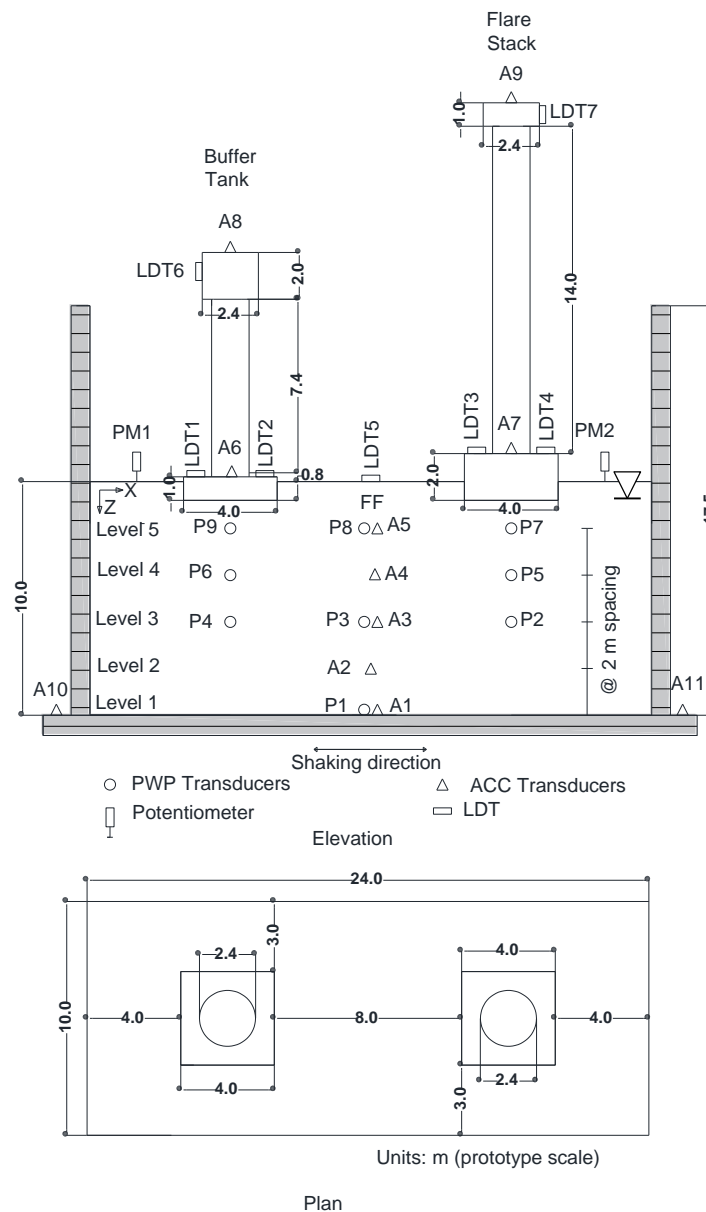
Fig. 3.1. Centrifuge model layout (note: the location of water table is 0.7 and 0.9 m below the top surface of the model ground for fully saturated and partially saturated model ground, respectively)
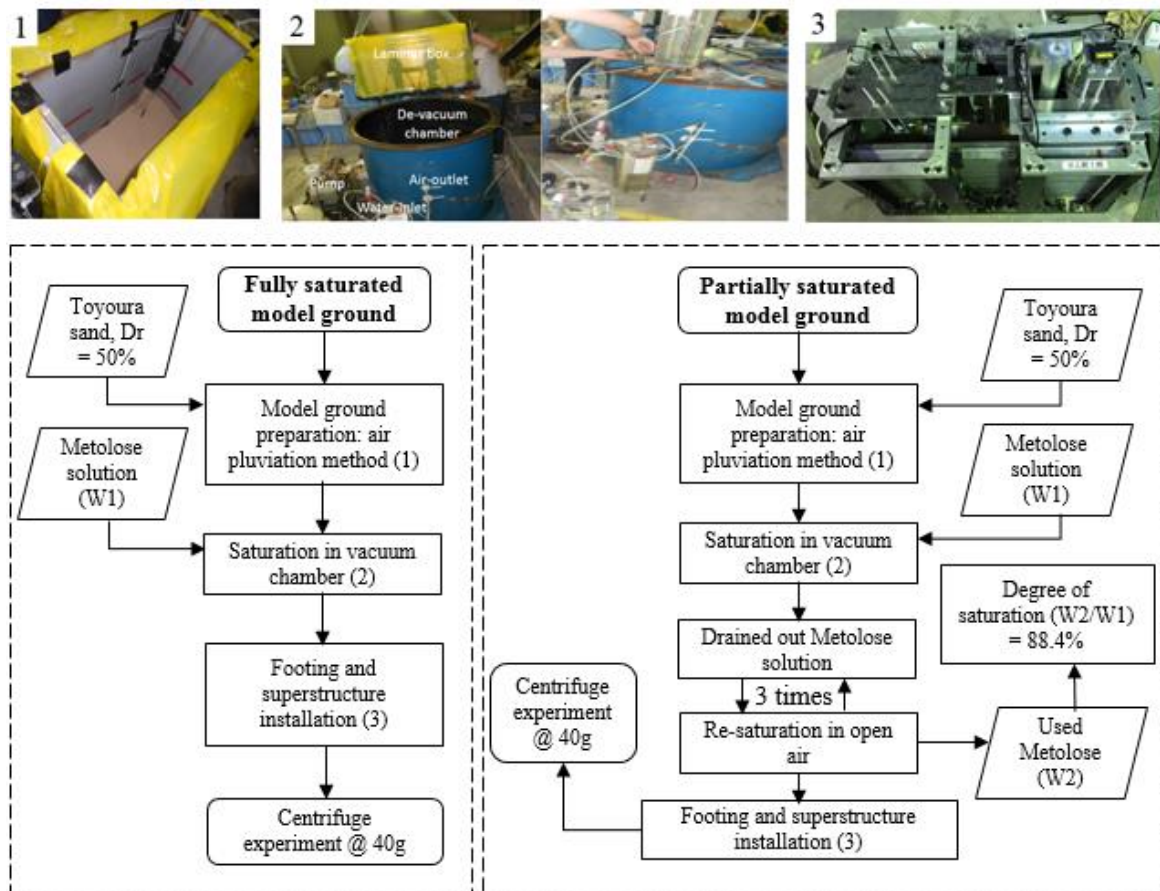
Fig. 3.2.　Flow chart for fully saturated and partially saturated model ground preparation

Estimated water tables for fully saturated and partially saturated model grounds are found to be at 0.7 m and 0.9 m respectively, below the surface of the ground in prototype scale. The vertical effective stress is one of the fundamental factors which determines the soil behavior. All measurable effects of change of stress, such as compression, distortion and a change of shearing resistance, are due exclusively to changes of effective stress (Atkinson, 2007). The initial effective stress is calculated (as tabulated in Table 3.1) by subtracting the pore water pressure from the total stress. Vertical stress at desirable depths because of foundation-structure is calculated using Boussinesq's method which further is used to evaluate the vertical effective stress distribution within the ground.

Table 3.1. Distribution of different transducers within the model ground

Level	Transducers*	Location (prototype scale)		Initial effective stress (σ'_{vo}) at different level		
		X m	Z (depth) m	Magnitude, kPa (prototype scale)		Description
				Fully saturated**	Partially saturated***	
Level 1	P1, A1	12	10	91.60	93.56	Model centerline
Level 2	A2	12	8	63.12	65.08	Model centerline
Level 3	P2	18	6	50.42	52.38	Below FS footing
	P3, A3	12	6	51.64	53.60	Model centerline
	P4	6	6	46.72	48.68	Below BT footing
Level 4	P5	18	4	43.69	45.65	Below FS footing
	A4	12	4	31.16	33.12	Model centerline
	P6	6	4	36.69	38.65	Below BT footing
Level 5	P7	18	2	43.00	44.96	Below FS footing
	P8, A5	12	2	08.36	10.32	Model centerline
	P9	6	2	31.00	32.96	Below BT footing

*A: acceleration transducers, P: pore pressure transducers

**Water table in case of fully saturated model ground is 0.7 m (17.5 mm in model scale) below the top surface of model ground

***Water table in case of partially saturated model ground is 0.9 m (22.5 mm in model scale) below the top surface of model ground

3.2 Testing scheme

After finishing the saturation process, the model is mounted on the shaking table at centrifuge lab facility. Before applying Tokachi-Oki ground motion, the centrifuge model is tested against a white noise (WN1) as shown in Fig. 3.3 to understand the dynamic characteristics of the system. Fig. 3.4 shows the transfer function which is estimated as the ratio of acceleration obtained at the top of superstructures (A8 and A9 as shown in Fig. 3.1) to the white noise acceleration recorded at the base of the centrifuge model ground (A1) in the frequency domain. The fundamental periods obtained during the experiments are 0.42 and 0.37 s for buffer tank (BT), and 0.56 and 0.58 s for flare stack (FS) corresponding, respectively, for fully saturated and partially saturated model grounds in prototype scale. Natural periods of BT and FS obtained for both the models are very close to the design periods. Ground motion recorded at Hachinohe Port during the 1968 Tokachi-Oki earthquake (NS component) is used as the dynamic excitation

after the white noise (WN 1).
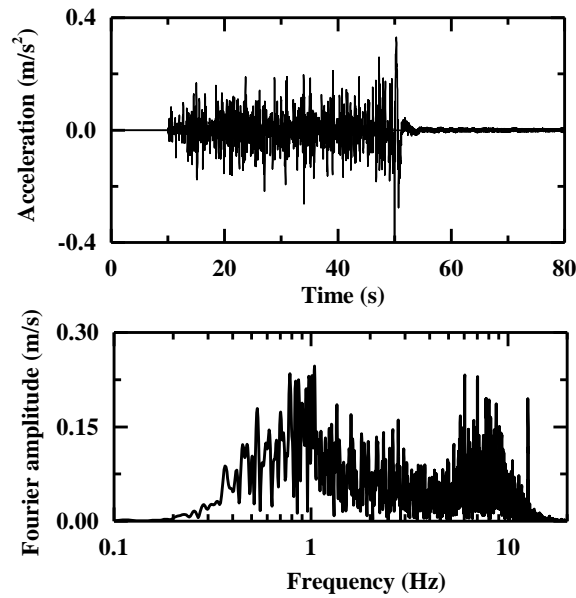
Fig. 3.3. Acceleration time history and Fourier spectra of input white noise (WN1) in prototype scale
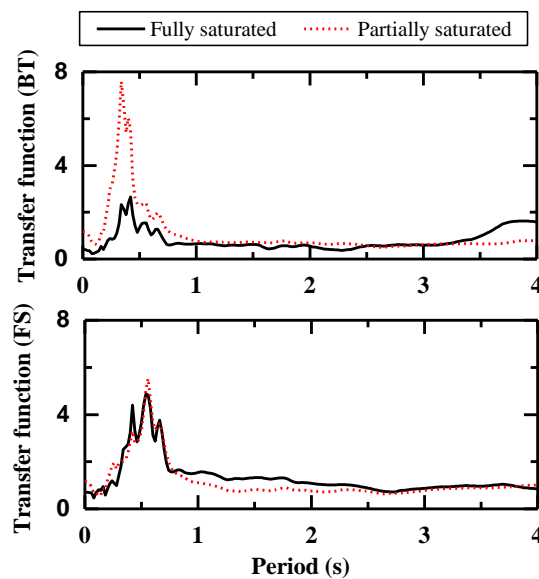
Fig. 3.4. Transfer Function obtained at top of Buffer Tank and Flare Stack in prototype scale

Fig. 3.5 shows the acceleration time histories, Fourier spectra and Arias intensity (Kayen and Mitchell, 1997) of the input base motions for fully saturated and partially saturated model

grounds. Exact simulation of ground motion in the centrifuge is quite complicated. Many trials were made to finalize the simulated shaking before performing the centrifuge experiment. It is imperative that the simulated ground motions agree well in time and frequency domain as well as depict alike Arias intensity to ensure the fair comparison between test results of fully and partially saturated model grounds. Base motions shown here are presented after having baseline correction and filtering. Filtering is performed in the frequency domain using the bandpass Butterworth filter with corner frequencies of 0.3Hz and 10 Hz respectively in prototype scale. It is evident that the simulated waveforms for both cases possesses similar intensity and are in good agreement both in time as well as frequency domain.
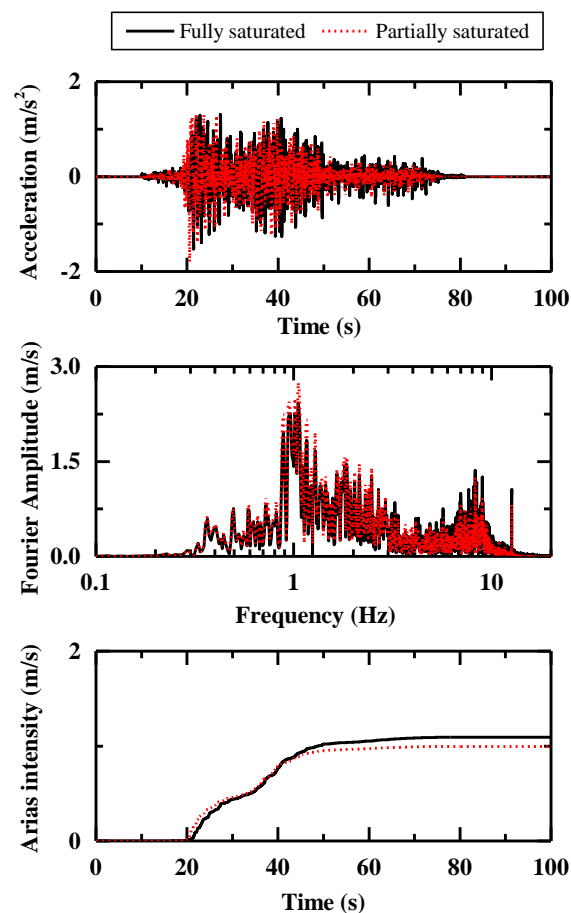
Fig. 3.5. Acceleration time histories, Fourier spectra and Arias intensity of Tokachi-Oki ground motion for both fully and partially saturated model grounds

3.3 Results and discussion

3.3.1   Evolution of excess pore water pressure

All the test results shown in the following sections are in the prototype scale unless mentioned otherwise. EPWP time histories are obtained at several desirable locations as shown in Fig. 3.1. Evolution of EPWP (generation and dissipation trend), plays a vital role in the understanding of the liquefaction phenomena. Soils at certain depth undergo liquefaction if the excess pore water pressure ratio (r_u) which is calculated by dividing the generated EPWP by the initial vertical effective stress at the respective depth, approaches to unity. Table 3.1 shows the initial vertical effective stress at all transducers locations for both fully saturated and partially saturated model grounds.

Fig. 3.6 depicts the EPWP time histories for the fully saturated and partially saturated model grounds when subjected to Tokachi-Oki ground motion. At P1 (Level 1), the EPWP time histories are almost same in both the cases in terms of maximum magnitude; though, the dissipation trend is marginally delayed in case of partially saturated model ground. As the hydrostatic pressure at Level 1 (P1, base of the model ground) is significantly high, there might be a possibility of volume change/dissolution of air voids. Therefore, both fully saturated and partially saturated model grounds exhibit similar behavior in terms of generated EPWP trends at the base of the model ground. At P2 and P4 (Level 3), the presence of air voids within the partially saturated model ground significantly delayed the generation and dissipation of EPWP in comparison with the fully saturated model ground. This behavior occurs primarily because of the increase in compressibility of the air and pore fluid mixture in case of partially saturated model ground (Yegian et al., 2007). In addition, induced partial saturation reduced the overall permeability of partially saturated ground. This also justifies the behavior of the slower rate of generation and dissipation of EPWP as shown in Fig. 3.6. At this level (Level 3), the maximum magnitude of generated EPWP has surpassed the liquefaction state line (i.e. r_u=1) in case of fully saturated model ground whereas the liquefaction state is not observed in case of the partially saturated model ground. Similar behavior of EPWP generation and dissipation is observed at P6 (Level 4). In case of fully saturated model ground, liquefaction state is achieved at P6 whereas, the maximum magnitude of EPWP in case of the partially saturated model ground is far below the liquefaction state line. Unfortunately, the pore water pressure

transducers P3 and P5 did not work correctly because of some unforeseen reasons and hence are not shown in Fig. 3.6.
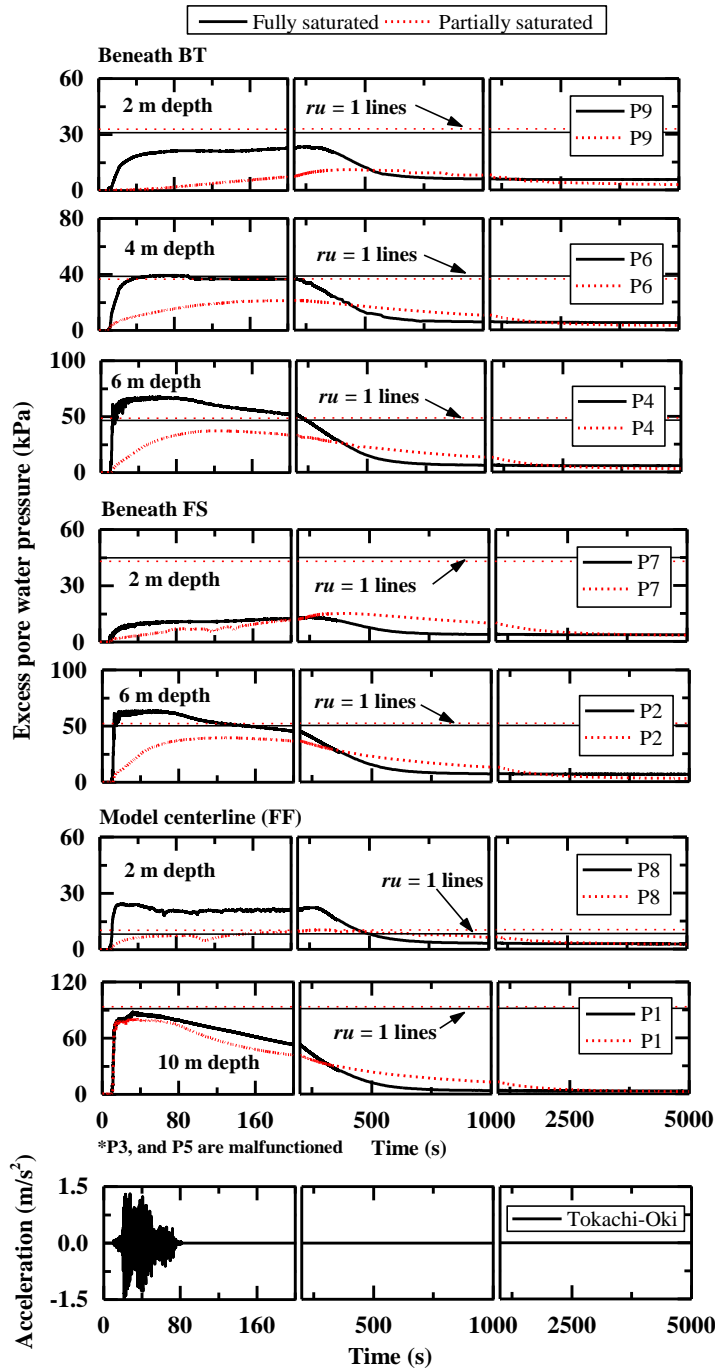
Fig. 3.6. EPWP time histories obtained during Tokachi-Oki ground motion

At shallower depth (Level 5), EPWP time histories at P7 share almost the same magnitude

of maximum EPWP for both fully saturated and partially saturated model grounds. However, the generation and dissipation rate of EPWP at P7 is delayed in case of partially saturated model ground in comparison with the fully saturated model ground. The possible explanation for this unusual behavior at P7 might be non-uniformity of partial saturation in the vicinity of Flare Stack (FS) footing. At P9 (Level 5), the maximum magnitude of generated EPWP is significantly less in case of partially saturated model ground in comparison with the fully saturated model ground.

The liquefaction state is not achieved at P7 (under FS) and P9 (under BT) because of large vertical effective stress due to the foundation-structure system. It is interesting to note that the maximum magnitude of EPWP at P8 (Level 5) in case of the fully saturated model ground is more than the one at P7 and P9, even though the vertical stress at P8 is less than P7 and P9. The reason for this is the flow of pore fluid and settlement caused under the shallow foundation (Dashti et al., 2010; Zeybek and Madabhushi, 2017). Both BT and FS foundation has influence zone of large confining stress in the vicinity of foundation, and because of vertical hydraulic gradient setup during dynamic excitation, the pore fluid is bound to flow nearby the model centerline. The availability of significant amount of migrated pore fluid for a long time resulted in more EPWP at P8 than P7 and P9. Pore pressure transducers (PPTs) at a shallower depth (P7-P9) exhibit maximum EPWP quite after the shaking period in case of partially saturated model ground as shown in Fig. 3.6. The reason for this is the slower rate of water flow from the deeper portion of the model ground in case of partially saturated ground. It is to be noted that all PPTs show a small magnitude of the residual EPWP in dissipation phase at 5000 s except at P1. This is associated with the fact that the PPTs experienced a marginal settlement during the shakings which changed the overall void ratio (probably decreased) and the marginal rise of the water table. This inevitable settlement of PPTs during white noise and Tokachi-Oki ground motion changed the initial vertical effective stress condition at the location of PPTs. However, the initial vertical effective stress is assumed to be constant at different levels in the model ground as mentioned in Table 3.1 for the sake of brevity.

3.3.2   *Air void dissolution/collapse during shaking*

Air voids are introduced using the drainage-recharge method to induce partial saturation within the model ground. The detail process of air induction is described earlier. It is to be noted that

the model grounds are prepared in 1g condition and the calculated degree of saturation is certain to change at 40g environment within the partially saturated model ground. Introducing Boyle's law and assuming air voids to be isolated and soil grains to be incompressible, the distribution of the degree of saturation is estimated within the partially saturated model ground at 40g.

Fig. 3.7 depicts that the degree of saturation increases (significantly) at the deeper portion of the model ground due to high hydrostatic pressure condition. This is also confirmed by the evolution of EPWP as explained earlier. There are two governing factors by which the induced partial saturation can increase the liquefaction resistance of the ground. The first factor is the increase in the compressibility of the pore fluid due to the air voids entrapped within the pore fluid. This mechanism helps to restrict the rate of development of EPWP during cyclic loading which is also witnessed during the EPWP build-up stage in the experiment as depicted from Fig. 3.6. The second one is matric suction which is not significant in the case of liquefiable soil as explained by Bishop and Blight (Bishop and Blight, 1963). By implementing the above stated Boyle's law, the maximum potential volumetric compressibility (strain) within the model ground (described in Chapter 5) can be estimated using the evolution of EPWP during the shaking (Okamura and Soga, 2006; Marasini and Okamura, 2015).
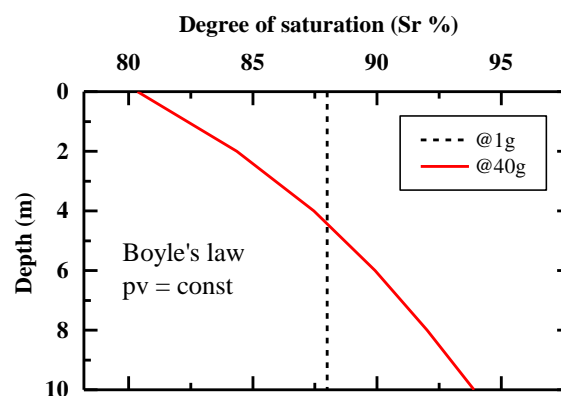
Fig. 3.7.   Degree of saturation variation within the partially saturated model ground

3.3.3   *Permeability of partially saturated ground*

Fig. 3.8 shows the soil-water characteristic curve for Toyoura sand (Unno et al., 2008). The permeability of partially saturated model ground at a different degree of saturation (along the depth as shown in Fig. 3.7) is estimated using van Genuchten model (V-Genuchten, 1980).

Initially, the van Genuchten model parameters for Toyoura sand are calculated using the experiment data retrieved from Unno et al. (2008). Then, the variation of the degree of saturation along the depth of the partially saturated model ground (Fig. 3.7) is used to estimate the volumetric water content. After that, the effective degree of saturation S_e (V-Genuchten, 1980) is determined and used to calculate the permeability coefficient.

The permeability coefficient plotted in Fig. 3.9 is the ratio of K_{P_sat} (permeability of partially saturated ground) and K_{F_sat} (permeability of fully saturated ground). For detail procedure of permeability estimation, readers are suggested to refer Unno et al. (2008) and Fredlund et al. (1993).
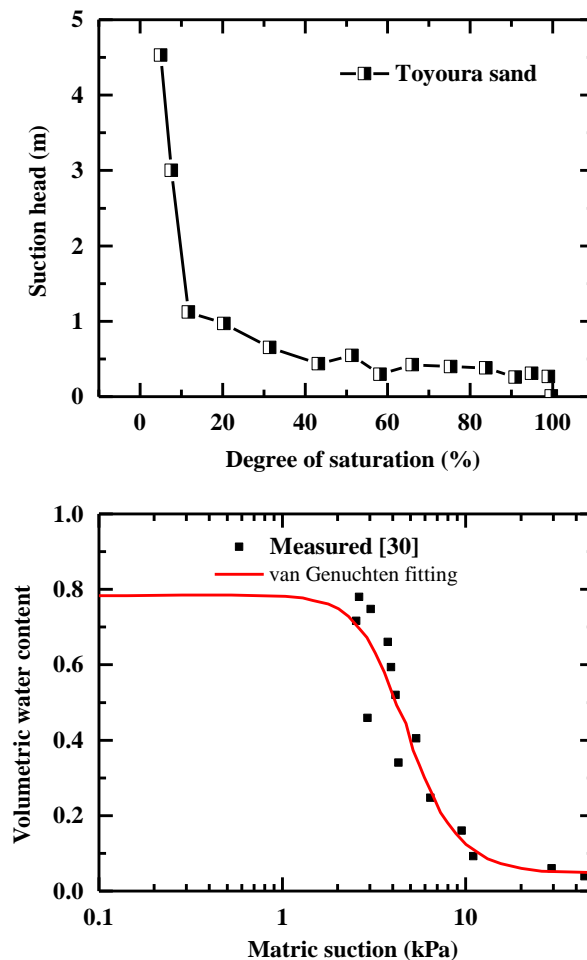
Fig. 3.8. Soil-water characteristic curve for Toyoura sand (after Unno et al., 2008)
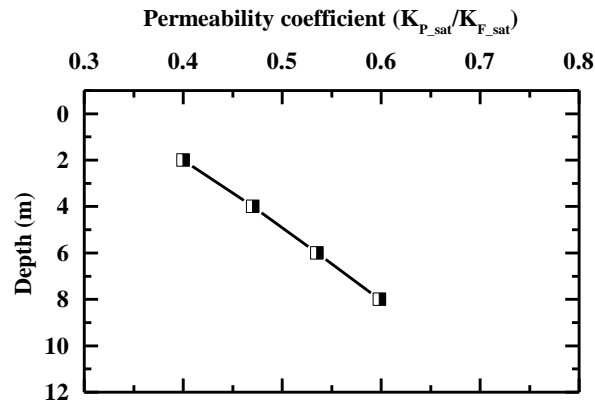
Fig. 3.9. Change in permeability because of induced partial saturation

It is evident from Fig. 3.9 that the permeability within the partially saturated model ground reduced significantly as much as up to 40 to 60% of the permeability of fully saturated model ground. 1-D consolidation analysis is also performed to estimate the overall relative permeability of the partially saturated ground. With appropriate boundary conditions and an initial value of pore water pressure at the end of the shaking (or at the beginning of dissipation phase), the dissipation curve of pore water pressure is estimated at P2 and P4 for both fully saturated and partially saturated grounds during Tokachi-Oki ground motion. The dissipation phase of pore water pressure is governed by the coefficient of consolidation which includes soil permeability, compressibility, and unit weight of pore fluid. The estimated dissipation curves of pore water pressure at P2 and P4 are fitted with the centrifuge test results by changing the permeability values (Fredlund et al., 1993). Then the average permeability coefficient (K_{P_sat}/K_{F_sat}) for P2 and P4 is obtained which is found to be 0.73 during the Tokachi-Oki ground motion. This also corroborates the fact that induced air-voids reduce the overall permeability of the partially saturated ground.

3.3.4 Settlement behavior

Fig. 3.10 depicts the settlement observed at BT and FS footings during Tokachi-Oki ground motion. Two laser displacement transducers (LDTs) are used to record the footing settlement for BT (LDTs 1, and 2) and FS (LDTs 3, and 4). It is evident that both BT and FS footings undergo excessive settlement in case of fully saturated ground. The foundations begin to settle immediately after the shaking began and continued even after the shaking ceased. BT footing

exhibits large magnitude of differential settlement (the difference between the settlements of both sides of the footing) by the side of LDT1 in case of the fully saturated ground; whereas, FS footing exhibits comparatively smaller but significant magnitude of differential settlement in case of partially saturated ground. Seismic demand, relative density, liquefaction state, foundation height/width ratio, bearing pressure and overall drainage in the vicinity of the foundation are few of the factors to mention which govern the overall liquefaction induced settlement mechanism of shallow foundation (Dashti et al., 2010). In addition, the non-uniform degree of partial saturation in the ground might be responsible for the differential settlement of foundation-structure system in case of partially saturated ground. A sudden jump in LDT2 reading (see * in Fig. 3.10) in the very beginning of shaking is apparent which might be because of movement of the sensor holder/plate as such sudden change could not be seen in all other sensors.
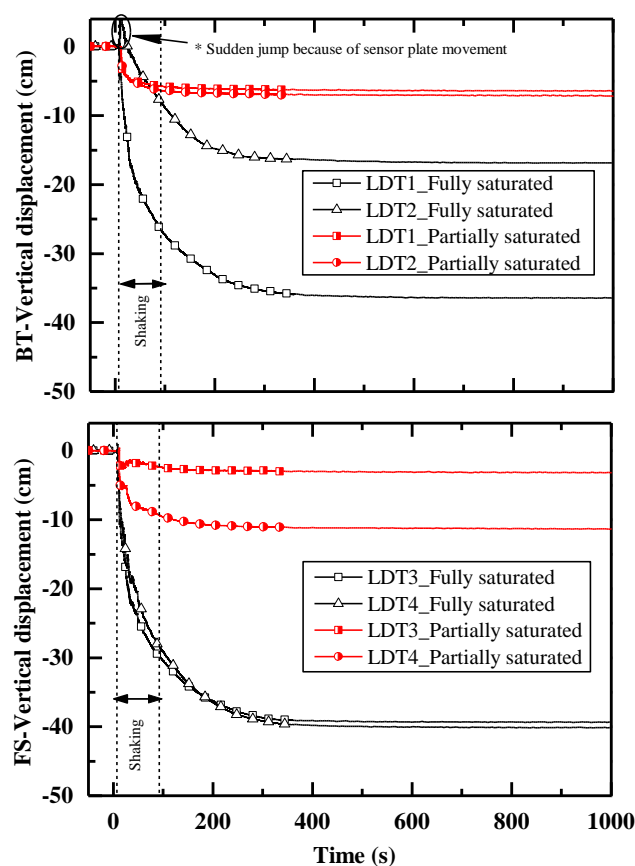
Fig. 3.10. Settlement time histories of BT (LDT1 and 2) and FS (LDT3 and 4) during Tokachi-Oki ground motion

Fig. 3.11 shows the cumulative average settlement of BT and FS footings during and after the shakings. It is evident that footings undergo significant co-shaking settlement (settlement occurred during shaking) in case of fully saturated model ground during Tokachi-Oki ground motion. Shear-induced deformation is the governing factor for co-shaking settlement, and it can be seen from Fig. 3.11 as the vertical settlement of FS is significantly large compared to the vertical settlement of BT. The shear strength of soil in the vicinity of the foundation start to mobilize because of generation of EPWP (reduction in mean vertical effective stress) and hence shear-induced co-shaking settlement is apparent. The induced partial saturation can mitigate the shear-induced deformation as the co-shaking settlement in case of the partially saturated ground is less in comparison with the fully saturated ground. Volumetric strains due to partial drainage and development of post-liquefaction/shaking reconsolidation strains are the prime responsible factors associated with the post-shaking settlement. It is evident from Fig. 3.11 that the post-shaking settlement is significantly mitigated by the presence of air voids in case of partially saturated model ground.
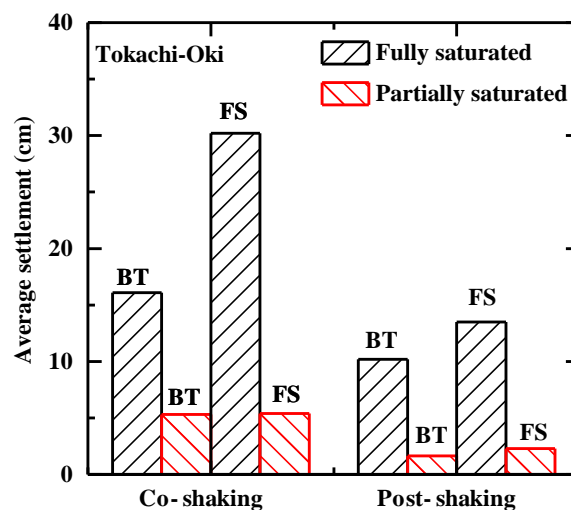
Fig. 3.11. Co-shaking and post-shaking settlement during Tokachi-Oki ground motion

3.3.5 Kinematic and inertial interaction between the model ground-foundation-structure system

It is a well-established fact that during the dynamic excitation soils undergo deformations which

are further foisted on the foundation. During the seismic loading, the wave propagates through the soil media which altered in the vicinity of the structure. This well-known phenomenon of soil-structure interaction dominatingly governs the structure behavior in the liquefiable ground. Inertial interaction is not significant in case of liquefiable ground because the soil is assumed to behave as a seismic isolator to the foundation (Karamitros et al., 2013). However, superstructure's dynamic properties that control inertial interaction (e.g., mass, stiffness, height to width ratio) have shown significant influence on the evolution of the pore water pressure, settlement trend, tilt potential, which in turn, affect the overall performance of superstructure (Sancio et al., 2004). Fig. 3.12 depicts the acceleration time histories recorded at several locations on/within foundation-superstructure and model ground (see Fig. 3.1). The position of A5 (at Level 5) along the model centerline is considered as the far-field (FF). Although A5 is placed significantly away from, and approximately at the same level of the base of the footings of both structures, some interaction is still expected to happen due to spacing constraints between the structures. Acceleration records measured at A5 showed the significant amount of de-amplification in acceleration time histories for both fully saturated and partially saturated model grounds during Tokachi-Oki ground motion. Significant de-amplified acceleration time history of A5 also consolidate the fact that the model ground exhibits considerable softened state during Tokachi-Oki ground motion. Partially saturated ground shows relatively less de-amplification in comparison with the fully saturated ground at all locations. This explains that the partially saturated model ground exhibits more liquefaction resistance (relatively less model ground softening) in comparison with the fully saturated model ground. Similar observations of acceleration records were made by Zeybek and Madabhushi (2017).
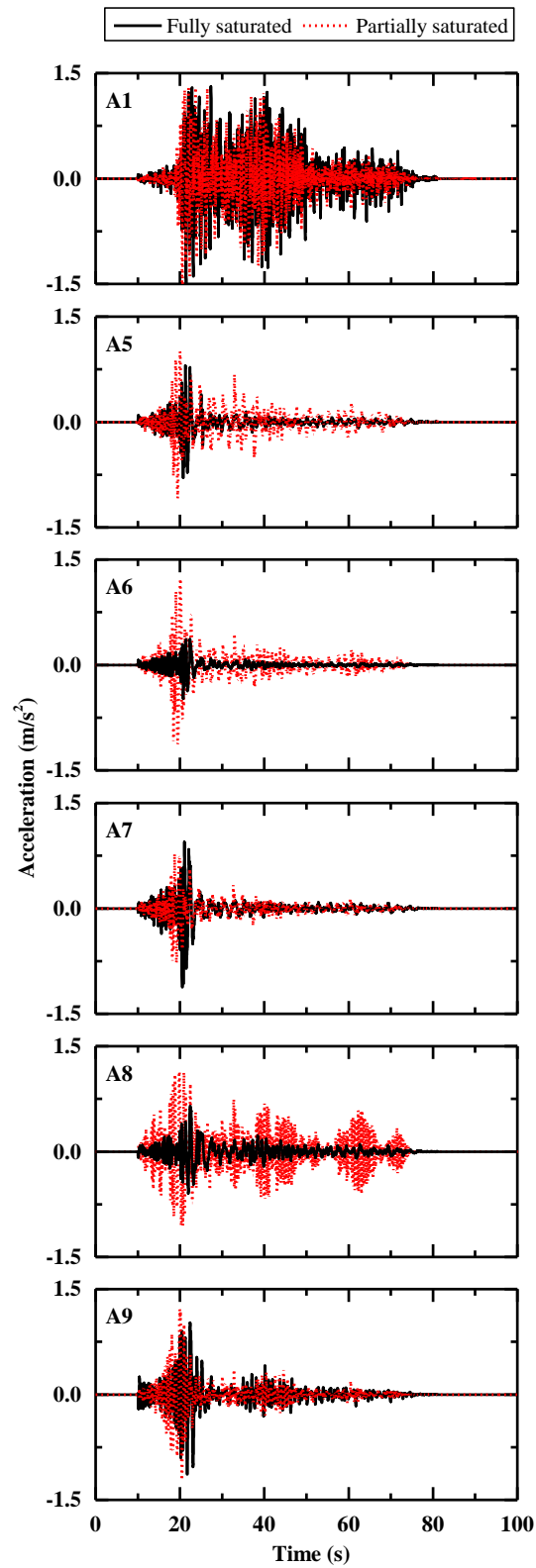
Fig. 3.12. Acceleration time histories during Tokachi-Oki ground motion

3.4 Summary

Dynamic centrifuge experiments are carried out to investigate the effects of partial saturation on shallow foundation resting on liquefiable ground. The drainage-recharge method is used to induce partial saturation within the liquefiable ground. The response of partially saturated ground is compared with the fully saturated ground in terms of the evolution of EPWP at several locations, settlement time histories of footings, and kinematic and inertial interaction between soil-foundation-structure system. The degree of saturation for fully saturated and partially saturated are 99.1 and 88.4%, respectively. The observed slower rate of generation and dissipation of EPWP in case of partially saturated ground, consolidate the fact that the compressibility of pore fluid increases because of inclusion of the air voids within the ground. Also, the partially saturated ground shows overall less permeability in comparison with the fully saturated ground. Induced partial saturation is found to minimize the settlement of foundation-structure systems in case of partially saturated ground. The kinematic seismic demand experienced by foundation-structure systems is relatively large in case of partially saturated ground in comparison with fully saturated ground. Despite that fact, centrifuge experiments show promising results in favor of induced partial saturation to mitigate the liquefaction-induced effects on shallow foundation.

Chapter 4. Centrifuge modeling of hybrid foundation

A hybrid foundation is developed to mitigate the liquefaction-induced effects on a shallow foundation. The proposed hybrid foundation is a combination of the gravel drainage system and friction piles having spiral blades devised under the footing as a hybrid mitigation technique against the liquefaction-induced effects on a shallow foundation. The hybrid foundation is tested for temporary structures namely buffer tank (BT) and flare stack (FS) at an industrial process plant. After the life span of the structure, the hybrid foundation is planned to be re-used for a different structure with keeping the gravel drains and re-installing the friction piles. For that purpose, piles are not fixed with the footing, i.e., the pile and the footing has a certain clear spacing to allow relative vertical movement and to limit the footing tilting. The diameter of the footing hole (in which friction pile passes through) is kept 1.25 times the outer diameter of friction pile. Ease of centrifuge modeling and friction pile installation sequence is also considered while selecting the minimum clear spacing between footing and friction piles. Friction piles are supposed to yield frictional resistance during the earthquake and presumed to minimize the rocking/tilting behavior of the foundation structure system. The stress of the foundation-structure system is presumed to be transferred through the ground (not through the friction piles), and hence a clear marginal spacing is kept between friction piles and footing to avoid the subsidence below the footing during the shaking.

4.1 Development scheme

The development of the hybrid foundation is carried out with the help of physical modeling using the centrifuge lab facility. The development is carried out in three phases. All the model configurations are shown in Fig. 4.1.
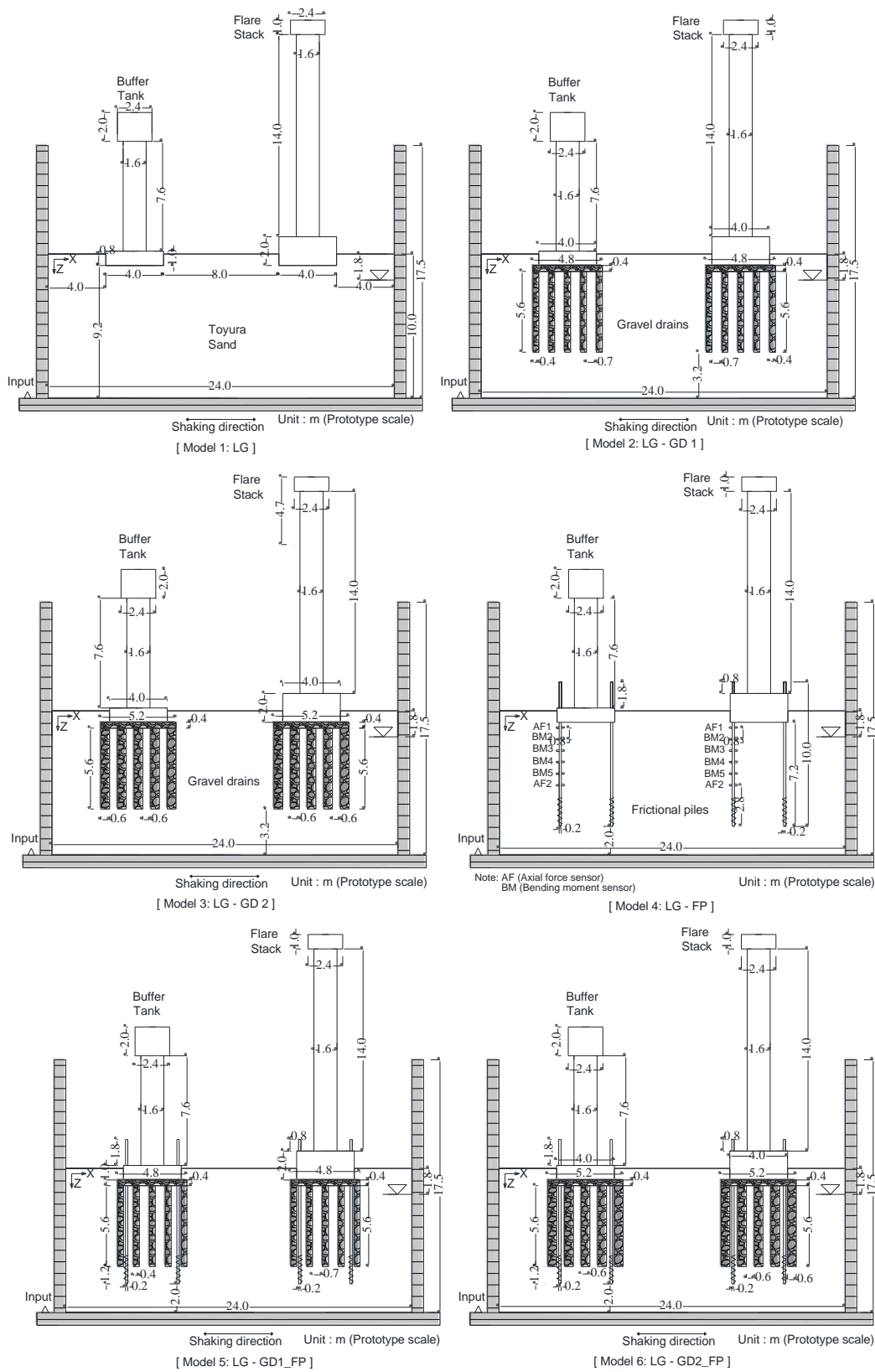
Fig. 4.1. Models configuration in prototype scale

In the first phase, an attempt is made to understand the behavior of shallow foundation resting on the liquefiable ground (using Model 1, as explained in Chapter 2) during a strong ground motion. In the second phase, the performance of gravel drainage system and friction piles are investigated. Three types of model tests are performed (using Models 2-4) in which two model tests consist of the gravel drainage system of different drainage capacities, and one model test consists of only friction pile (properties are tabulated in Table 4.1) as the liquefaction countermeasure. In the third stage, the performance of hybrid foundation is investigated using two model tests (using Models 5, and 6). Each model test consists of the friction piles and gravel drainage system of different drainage capacities as individually investigated in the second phase. The model ground is prepared using the Toyoura sand with target relative density of 50% by air pluviation method using the sand hopper as described in Chapter 2. The configuration of foundation and superstructure (buffer tank and Flare stack) is shown in Table 2.4 (Chapter 2). The location of different transducers for all the Models 1-6 are shown in Fig. 4.2 (positions are tabulated in Table 4.2).
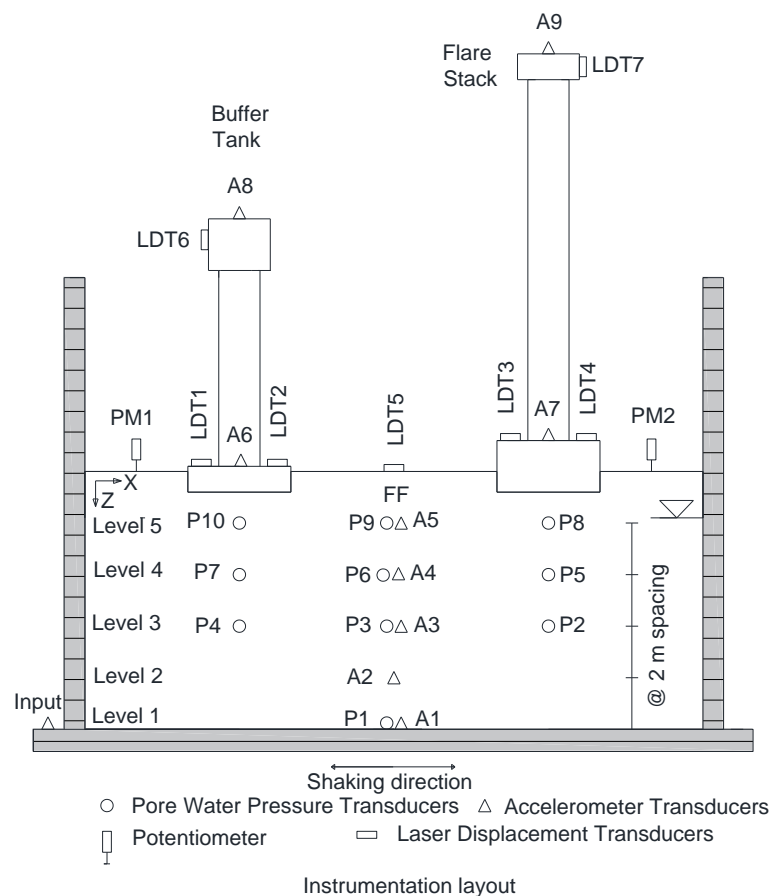
Fig. 4.2. Different transducers layout in centrifuge model

Table 4.1. Index properties of Toyoura sand and Silica no. 3 and properties of friction pile

Description	Toyoura sand	Silica no. 3	Description	Friction pile (prototype)
Specific gravity, G_s	2.65	2.63	Material	SUS304
D_{50} (mm)	0.19	1.72	Length	10 m
D_{10} (mm)	0.14	1.37	Pile outer diameter	16 cm
Maximum void ratio, e_{max}	0.973	1.009	Pile inner diameter	12 cm
Minimum void ratio, e_{min}	0.609	0.697	Length (spiral blades)	2 m
Permeability, k (m/s)	2E-4	6.6E-3	Thickness (spiral blades)	2 cm
Relative density, D_R	~50%	~30%	Pile outer diameter (with spiral blades)	32 cm
			EI at Pile head	4.178E3 kN-m^2
			EA at Pile head	1.671E6 kN

Table 4.2. Locations of different transducers within the model grounds

Level	Transducers*	Location** (prototype scale)		Initial vertical effective stress (σ'_{vo}) at different levels***	
		X	Z (depth)	Magnitude, kPa	Description
		m	m	(prototype scale)	
Level 1	P1, A1	12	10	102.40	Model centerline
Level 2	A2	12	8	73.92	Model centerline
Level 3	P2	18	6	61.22	Below FS footing
	P3, A3	12	6	65.44	Model centerline
	P4	6	6	57.52	Below BT footing
Level 4	P5	18	4	54.49	Below FS footing
	P6, A4	12	4	41.96	Model centerline
	P7	6	4	47.49	Below BT footing
Level 5	P8	18	2	53.80	Below FS footing
	P9, A5	12	2	26.16	Model centerline
	P10	6	2	41.80	Below BT footing

* P: Pore water pressure transducers, A: Accelerometers
**Locations of the transducers are identical in all the models (Models 1-6)
*** Including vertical stress induced by the foundation-structure systems

The guide frames are prepared to make the gravel drainage system as shown in Fig. 4.3. The guide frames are kept at desirable locations (under both BT and FS) while preparing the model ground. Initially, the gravel drain casings are covered with tape while pouring the Toyoura sand. The guide frame has enough opening for Toyoura sand to pass through and to

form uniform model ground in the vicinity of gravel drains. After achieving the required level of the model ground with Toyoura sand, Silica no.3 (properties are tabulated in Table 4.1) is poured inside all the gravel drain casings carefully. Then, guide frames are taken out from the model ground with due care to avoid any possible disturbance and densification within the model ground. It is to be noted that the length of gravel drain casings attached to guide plates are kept 10 mm (in model scale) longer than the required length of gravel drains in the model ground. The reason for this is to form a 10 mm deep (0.4 m in prototype scale) gravel mat over the group of gravel drain piles.

From Fig. 4.3, a little overflow of Silica no. 3 is evident which in turn is used to form the gravel mat of 10 mm (in model scale) thickness. By adding Silica no.3, the gravel mat is formed with due care to avoid any densification around the gravel drains. After finishing the model ground preparation, friction piles (properties are tabulated in Table 4.1) are inserted in the model ground by means of screw driving. Due care is taken while inserting the friction piles to avoid/minimize any possible disturbance or densification of the model ground. The saturation-process (as described in Chapter 2) for all the models took approximately 55 hours to complete. After the saturation, superstructures are mounted over the footings. Relative densities and degree of saturation (at 1g) for all the Models 1-6 are tabulated in Table 4.3. Due care is taken to estimate the degree of saturation for all the model grounds using mass, volume and densities relationships. However, it is worth noting that certain errors still happen to have a scope as mentioned by Kutter (2013).
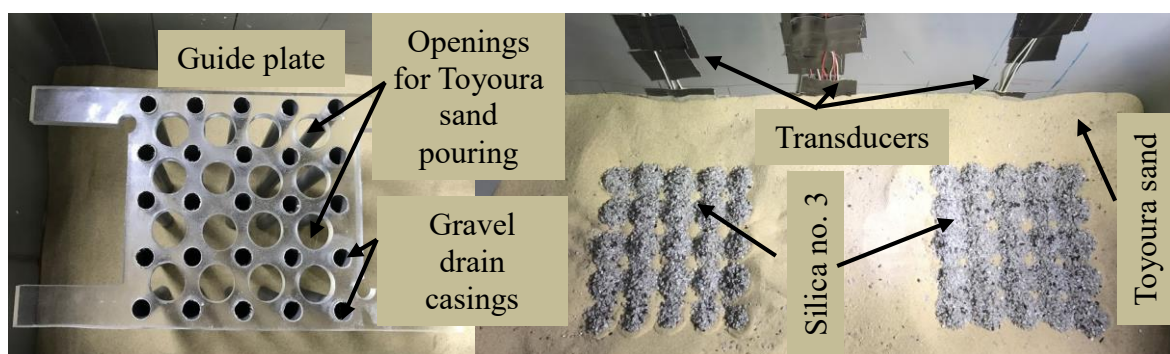
Fig. 4.3. Guide plate to form the gravel drains and typical array of gravel drains after removing the guide plates (for both BT and FS)

Table 4.3. Test description and relative density and degree of saturation (at 1g) for
Models 1-6

Test code	Model description	Relative density	Degree of saturation
Model 1	LG: Liquefiable ground	D_R = 52.8%	99.4%
Model 2	LG-GD1: Liquefiable ground with gravel drainage type 1*	D_R = 51.6%	99.2%
Model 3	LG-GD2: Liquefiable ground with gravel drainage type 2**	D_R = 54.0%	99.5%
Model 4	LG-FP: Liquefiable ground with friction piles	D_R = 53.1%	99.1%
Model 5	LG-GD1_FP: Liquefiable ground with gravel drainage type 1 and friction piles	D_R = 53.9%	99.3%
Model 6	LG-GD2_FP: Liquefiable ground with gravel drainage type 2 and friction piles	D_R = 55.2%	99.2%

*Gravel drainage type 1: Group of 5 x 5 gravel drains with 0.4 m diameter of each drain and 0.7 m clear spacing
** Gravel drainage type 2: Group of 5 x 5 gravel drains with 0.6 m diameter of each drain and 0.6 m clear spacing

After model preparation, the instrumented model is placed in the centrifuge and spun at the centrifugal acceleration of 40g. Then Metolose solution is drained out using pre-installed standpipes and a valve at the base of the container to bring down the water table at a depth of 1.8 m (in prototype scale) at 40g. For the realistic seismic response of liquefiable model ground, the simulated motion in the centrifuge should reasonably reproduce the full range of frequencies present in the recorded earthquake motion. All the models (Models 1-6) are tested under the earthquake ground motion recorded at the Hachinohe Port in 1968 Tokachi-Oki Earthquake (NS component). Before applying the Tokachi-Oki ground motion, the models are subjected to white noise to evaluate the dynamic characteristics of the system.

Fig. 4.4 shows the commanded and actual input Tokachi-Oki ground motions in the centrifuge for all the Models 1-6. All the input motions are presented after having baseline correction and filtering. Filtering is performed in the frequency domain using the bandpass Butterworth filter with corner frequencies of 0.3Hz and 10 Hz respectively. Actual input Tokachi-Oki ground motions for all the Models 1-6 are reasonably in good agreement with the commanded Tokachi-Oki ground motion. The repeatability of input motions both in frequency and time domain is satisfactory. Fig. 4.4 depicts that the Arias intensity of actual input motion is large in the case of Model 6 in comparison with Models 1-5. Although due care is taken

during all the experiments; however, this kind of inconsistency is inevitable in dynamic centrifuge experiment while simulating the ground motion.
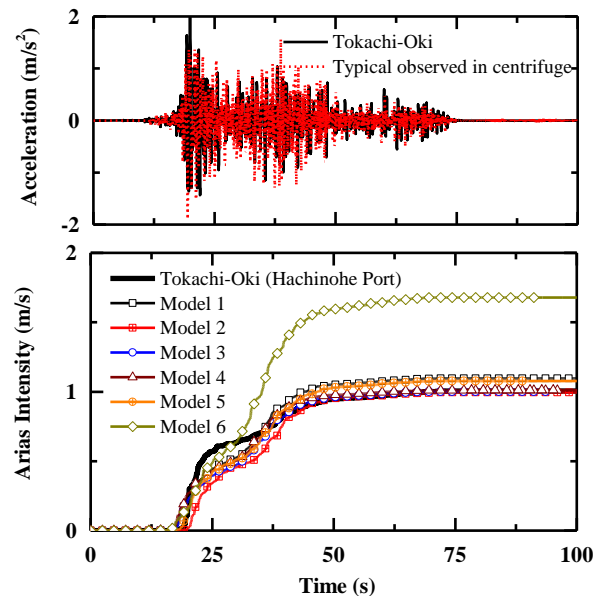
Fig. 4.4. Typical observed acceleration time history in centrifuge and Arias intensities of all Models 1-6 for input Tokachi-Oki ground motion.

The performance of hybrid foundation is assessed based on generation and dissipation of excess pore water pressure (EPWP), settlement and tilting of the shallow foundation, behavior of model ground, seismic demand to the superstructures, bending moment and the axial force exerted on friction piles, and the overall soil-structure-interaction. The suitability and effectiveness of the hybrid foundation are evaluated against temporary structures such as buffer tank (BT) and flare stack (FS) imposing an average bearing pressure of 51.2 kPa and 71.2 kPa respectively at 0.8 m below the surface of the model ground in prototype scale. The detailed configuration of model foundation and structure system is explained in Chapter 2.

4.2 Design of gravel drainage system

Design charts reported by Seed and Booker (1977) in their seminal work and the revised guidelines presented by Bouckovalas et al. (2009) are used to design the gravel drainage system for Models 2 and 3 (as shown in Fig. 4.1). Many parameters, e.g., replacement area, target

excess pore water pressure ratio (r_u), earthquake intensity, reported case histories, and installation methodology of gravel drains, are considered while designing the gravel drainage system. Design specifications of both gravel drainage Types 1 and 2 are tabulated in Table 4.4. Liquefaction resistance curves for saturated Toyoura sand with a relative density of 50+/-5% for different confining pressure are obtained using the laboratory test results from Chiaro et al. (2012). Then, based on Seed and Booker (1977) it is found that Tokachi-Oki ground motion can be considered as a medium EQ to strong EQ (as specified in Table 4.4) for Models 1-6.

Table 4.4. Design specifications of gravel drainage Types 1 and 2

Specifications[*]	Gravel drainage Type 1	Gravel drainage Type 2
Drain diameter (m)	0.40	0.60
Length of gravel drain (m)	5.6	5.6
Clear spacing (m)	0.70	0.55
Treated Plan	4.8 m X 4.8 m	5.2 m X 5.2 m
Replacement area (%)	13.63	26.14
Maximum allowable clear spacing between gravel drains for target $r_u = 0.7$		
Earthquake intensity	For gravel drainage Type 1	For gravel drainage Type 2
Small EQ (Neq/NL = 1) **	0.74 m	1.12 m
Medium EQ (Neq/NL = 2) **	0.44 m	0.80 m
Strong EQ (Neq/NL = 3) **	0.28 m	0.64 m

* The layout of both gravel drainage types are shown in Fig. 4.1
** For more details, readers are suggested to read Seed and Booker (1977) and Bouckovalas et al. (2009)

It is evident that the gravel drainage Type 1 does not satisfy the design guidelines as the clear spacing between the drains are more than the maximum allowable spacing for medium EQ to strong EQ. Initially, it is hypothesized that gravel drainage system (Type 1) could render the targeted performance of hybrid foundation along with friction piles having spiral blades. However, centrifuge test results of Model 2 demonstrated the inefficiency of gravel drainage Type 1 in terms of both generation and dissipation of EPWP. Based on the performance of gravel drainage Type 1, redesign of the gravel drainage system is done, and new gravel drainage Type 2 is tested in Model 3 which satisfies the design guidelines as tabulated in Table 4.4. In addition to provide the significant drainage for developed EPWP to dissipate, the focus is put on shear-induced and post-liquefaction/shaking settlement due to presence of gravel drains

which alter the stresses and strains applied to the improved ground as highlighted by Priebe (1989), Baez and Martin (1993), and Adalier et al. (2003).

4.3 Results and discussion

4.3.1 Effectiveness of gravel drains

Liquefaction-induced effects on shallow foundation resting on liquefiable ground are discussed in Chapter 2 in details with the help of Model 1. Performance of gravel drainage systems (Types 1 and 2 as described in Table 4.4) are investigated in Models 2 and 3. EPWP time histories of different pore pressure transducers (PPTs) for Models 2 and 3 are presented and compared with EPWP time histories of respective PPTs of Model 1 in Fig. 4.5. It is evident from Fig. 4.5 that the dissipation rate of EPWP increases in accordance with gravel drainage capacity. It is to be noted that the drainage capacity of the gravel drainage system in Model 3 is more than the drainage capacity in Model 2. Larger the drainage capacity, quicker is the dissipation of EPWP as designed. For instance, at Level 3 (at P2, P3, and P4), the EPWP takes approximately 1000s to dissipate in case of Model 1 (no gravel drains), whereas in case of Model 3 the EPWP dissipates within 400s. The foremost reason for the inefficiency of gravel drainage Type 1 in the case of Model 2 is the less drainage capacity.

The targeted excess pore water pressure ratio (as described in Table 4.4) at the liquefied zone within the ground could not be achieved even in case of Model 3 as the maximum magnitude of EPWP at all PPTs (P1-P10) for Models 2 and 3, are almost similar to the one observed in Model 1 for respective PPTs. Surprisingly, the maximum EPWP at P9 and P10 in the case of Model 2 is more than the one observed in the case of Model 1. This might be associated with the non-uniformity of the model ground and possible densification because of the presence of gravel drains or relatively deeper positioning of PPTs. Although the capacity of the gravel drainage Type 1 is not sufficient to dissipate the EPWP; however, relatively larger permeability of gravel drains might have led to the flow of water from deeper portion to the shallower portion with more ease, resulting in large EPWP at the shallower portion in case of Model 2.
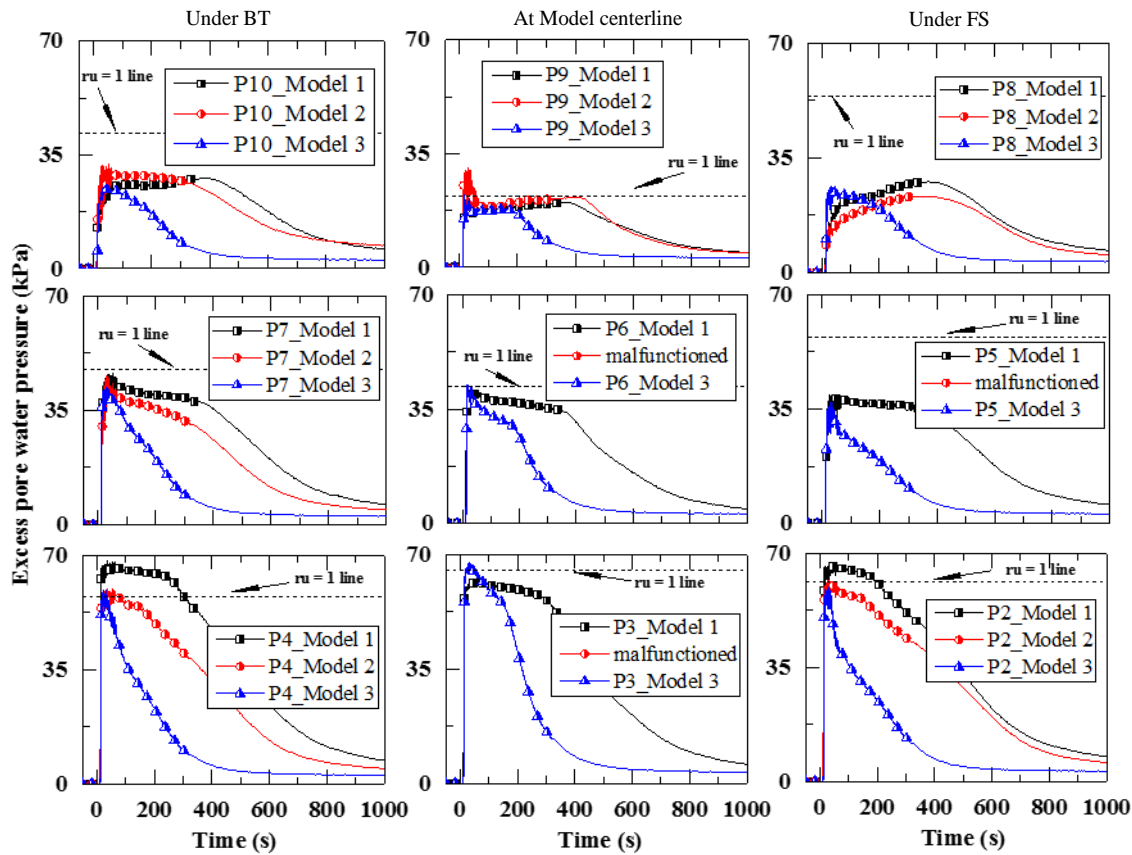
Fig. 4.5. Excess pore water pressure time histories of Models 1, 2 and 3 during Tokachi-Oki ground motion

The settlement time histories of both BT and FS foundation in Models 2 and 3 are presented and compared with the respective settlement time histories of Model 1 in Fig. 4.6 The influence of gravel drainage Type 1 (Model 2) on settlement mitigation is not significant. However, the overall settlement in case of Model 3 is less in comparison with Models 1 and 2 due to the presence of sufficient gravel drainage capacity. Considerable differential settlement for BT in case of Model 3 is occurred because of unusual change in the initial condition before dynamic excitation. While spinning up the centrifuge up to 40g; BT foundation experienced a significant amount of differential settlement probably because of non-uniformity of the model ground. This uneven settlement of BT before shaking exaggerated the differential settlement during Tokachi-Oki ground motion as shown in Fig. 4.6. It is to be noted that the ground settlement below treated zone (depth, z = 7-10 m) is not considered while interpreting the effectiveness of gravel drainage system to mitigate the footing settlement. Based on the evolution of EPWP time

histories at P3, it is found that the settlement (at Z= 7 m) is around 3.7 mm which is negligible compared to footing settlement (~80 mm). Although, the layer (depth, z = 7-10 m) settlement cannot be generalized based on settlement of a single PPT (i.e. P3).

Fig. 4.7 depicts the average settlement of the foundations during both co-shaking and post-shaking phase. In the case of Model 1, the foundations undergo excessive settlement during both co-shaking and post-shaking phase of the dynamic event. However, in the case of Models 2 and 3, the significant settlement of both BT and FS foundation occurred during the co-shaking phase. Fig. 4.7 depicts that the effect of post-liquefaction/shaking reconsolidation mechanism seems to be overshadowed by the presence of gravel drainage system which helped to reduce the total settlement of the shallow foundation.
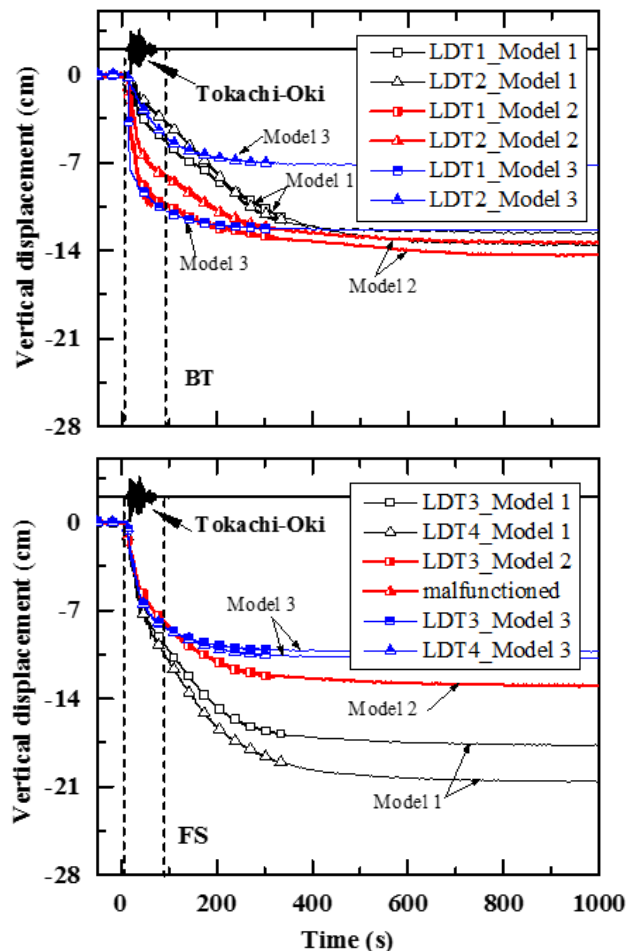
Fig. 4.6.   Settlement time histories of BT (LDT1 and 2) and FS (LDT3 and 4) for Models 1, 2 and 3 during Tokachi-Oki ground motion
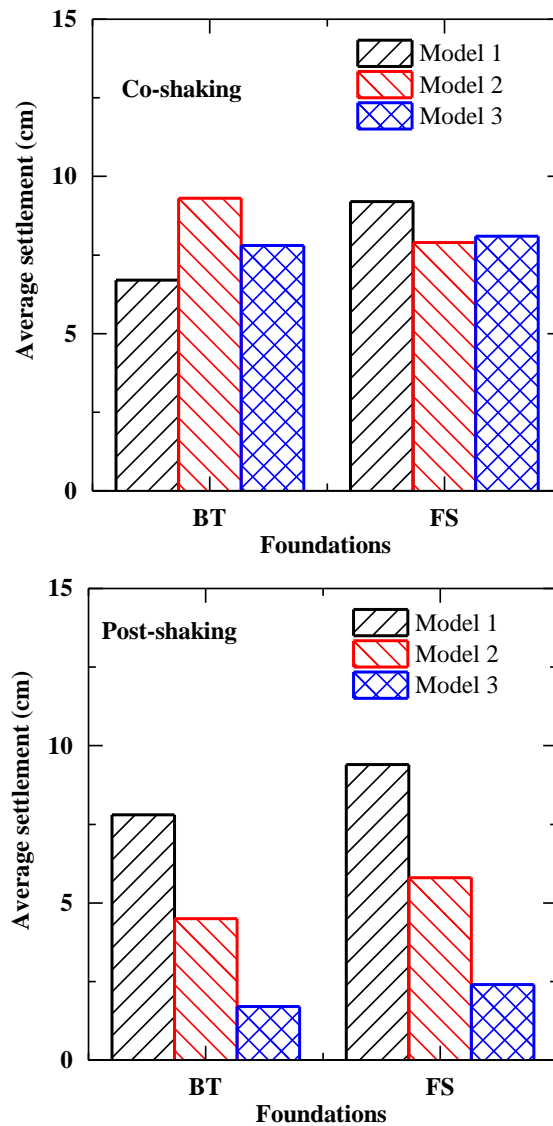
Fig. 4.7.   Average settlement during co-shaking and post-shaking phase for Models 1, 2, and 3

An attempt is made to estimate the pore fluid flow (vectors with total hydraulic head and resultant direction) during Tokachi-Oki ground motion at different time intervals. As the EPWP was recorded merely at 10 locations during the experiment (Fig. 4.2), linear interpolation of EPWP is done to estimate the pore fluid flow at several locations within the ground. Initially, the hydraulic gradient field is estimated by pore pressure distribution, and then the flow direction is estimated by using the hydraulic gradient field. Following assumptions are made to obtain qualitative pore fluid flow within the ground. The EPWP evolution at 0 m and 24 m length is assumed to be same as along the model centerline. This assumption ignores the boundary effects of the laminar container on the evolution of pore water pressure at the

boundaries. A linear interpolation of EPWP at non-measured locations might not be accurate at the shallower depth (in the vicinity of the BT and FS footing to be specific), because of different confining pressure. However, the effects mentioned above can be ignored for the overall qualitative representation of pore fluid flow.

Pore fluid flow within the ground in the case of Model 1 is shown in Fig. 4.8 during Tokachi-Oki ground motion. As discussed earlier, the dissipation of pore pressure is only permitted from the surface of the model ground. Hence, dominatingly the flow of pore fluid is always upward even after the shaking ceased and continued until pore fluid pressure reached the equilibrium state throughout the ground (Zeybek and Madabhushi, 2017) which is also apparent from Fig 4.8. In the case of Model 3, the drainage effects of the gravel drainage system are apparent as the radial flow (towards the gravel drainage zone) is set up as shown in Fig. 4.8. However, at the shallower depth, as the pore fluid tends to flow to the horizontal drainage boundary at the groundwater level, the pore fluid flow is almost vertical. Besides, the influence of gravel drains along model centerline seems negligible as the fluid flow are very much alike for both the Models 1 and 3.
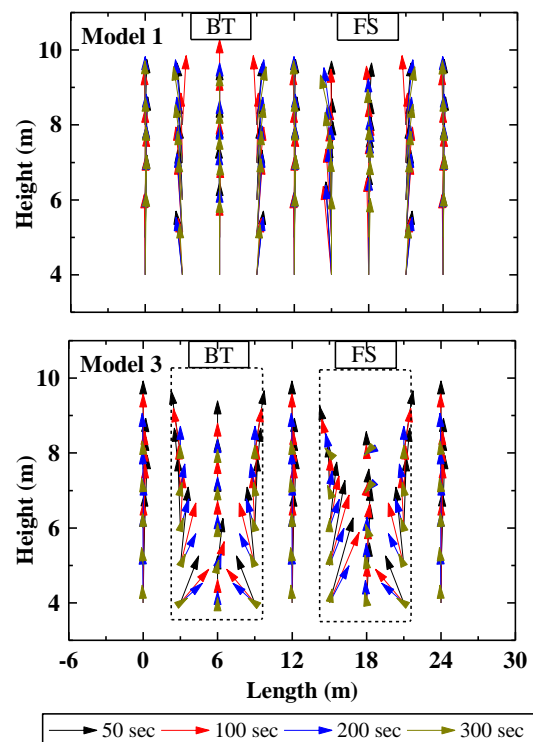
Fig. 4.8. Pore fluid flow at different times for Models 1 and 3 during Tokachi-Oki ground motion

4.3.2 *Effectiveness of friction piles*

Model 4 (see Fig. 4.1) is used to investigate the effectiveness of friction piles. The EPWP evolution for model 4 at different pore pressure transducers (PPTs) is found to be mostly in accordance with the Model 1 as the ground conditions are alike in both the Models 1 and 4. Fig. 4.9 shows the settlement time histories of both BT and FS foundation in Models 1, and 4. It is evident that the presence of friction piles reduced the overall settlement of shallow foundation significantly for both BT and FS. However, the friction piles are not able to restrict the post-shaking settlement of foundation which is the desired functioning as the friction piles are not fixed with the footings. Although, the post-shaking settlement rate is decreased for Model 4 in comparison with Model 1. Unfortunately, LDT4 did not work in case of Model 4 and differential settlement of FS could not be measured. However, the visual inspection after the experiment indicated less differential settlement of FS foundation in case of Model 4 in comparison with Model 1.
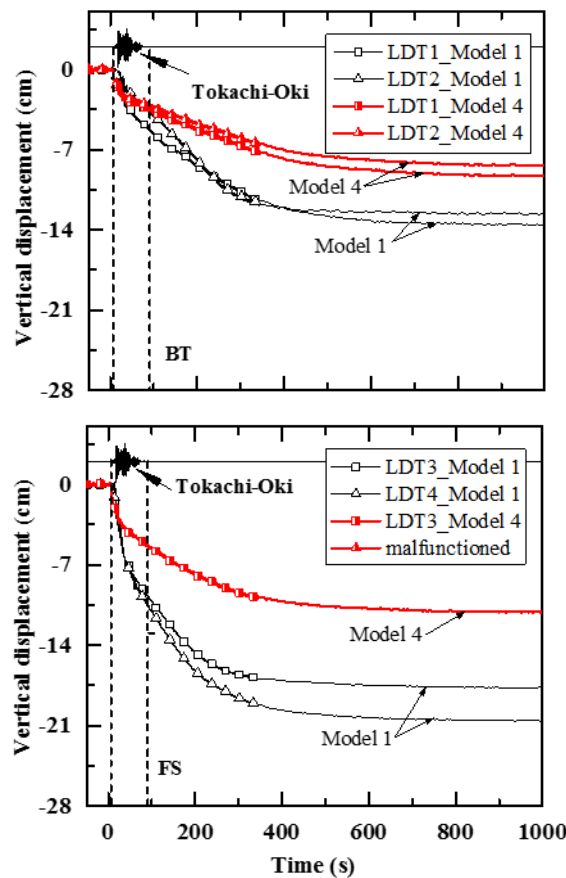
Fig. 4.9. Settlement time histories of BT (LDT1 and 2) and FS (LDT3 and 4) for Models 1 and 4 during Tokachi-Oki ground motion

During centrifuge experiments, two dominating mechanisms, i.e., inertial interaction between the foundation-structure system and kinematic interaction because of the friction pile and relative model ground movement, governed the overall soil-structure interaction phenomena. The seismic load exerted on friction piles are recorded in terms of bending moment (BM) and axial force (AF) at several locations as shown in Fig. 4.1. The seismic demand on the superstructure is further deduced using the recorded acceleration time histories at the foundation-structure system. Fig. 4.10 shows the exerted bending moment on BT and FS friction piles during Tokachi-Oki ground motion. Bending moment time histories depict that friction piles experienced a significant bending moment for both BT and FS during the shaking. The residual bending moment in post-shaking phase is also apparent. The exerted bending moment on friction piles substantially depends on inertial force/stress due to foundation-structure mass and the relative pile and soil movement during the dynamic event. Unfortunately, the precise relative movement of friction pile and surrounding soil could not be evaluated due to the limited number of friction pile sensors and absence of acceleration transducers under the centerline of BT and FS footings.

Friction piles as an integral part of the hybrid foundation are provided presuming that they would help to avoid/minimize the tilting and rocking motion of both BT and FS. However, experimental results show that the rocking behavior is not dominating even in case of the taller structure (FS) as discussed earlier. Axial force sensors (AF1 and AF2) are used to examine the load taken by piles as shown in Fig. 4.1. Maximum recorded axial force in case of FS is found to be 3 to 6 times more than the axial force in case of BT. One of the main purposes of providing the free connection between the footing and friction piles was to avoid any subsidence below the footing, i.e., the formation of a gap between the footing and soil below, during the shaking. Subsidence commonly takes place under the footing if the piles are fixedly connected with it. In that case, significant stress from the foundation structure system is transferred through the piles. Large exerted AF in case of FS footing indicates that the FS piles experienced significant fixity with the footing. Although, the friction piles (4 mm diameter at pile head in model scale) passes through the corners of footings with a clear spacing of 0.5 mm (in model scale), i.e., theoretically; footing and piles should exhibit the free connection (in fact it did happen to a great extent in case of BT footing). However, due to the large thickness of FS footing, the semi/fully rigid connection between FS footing and piles are inevitable. In this case, the transferred axial force through piles and BM at pile head largely depends upon the uncertain

fixity condition between the pile head and footing.
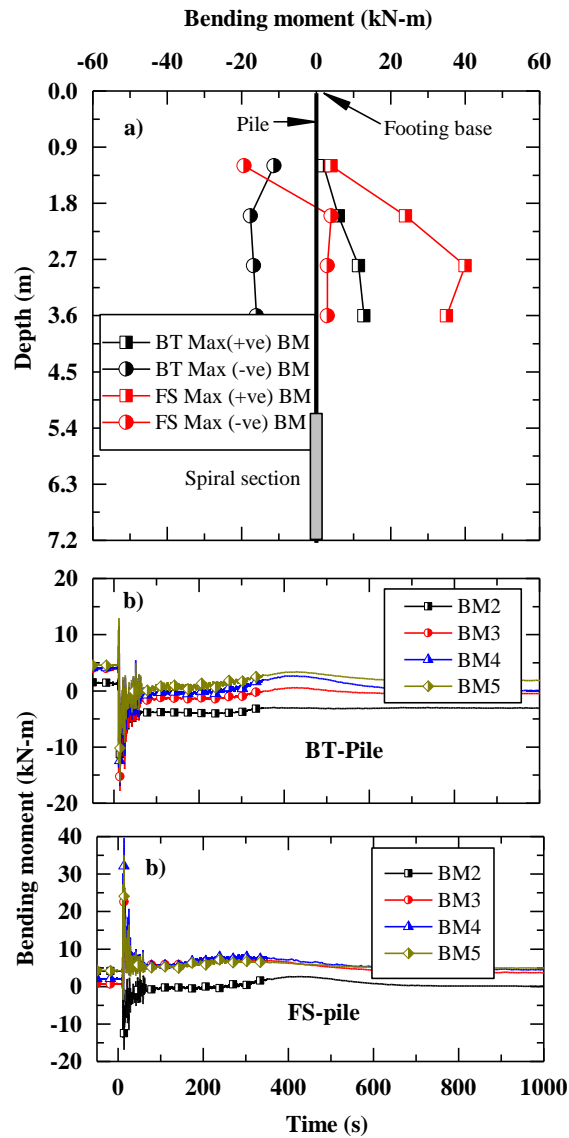
Fig. 4.10. Exerted bending moment on friction piles a) bending moment envelope, and b) bending moment time histories during Tokachi-Oki ground motion

4.3.3   Performance of hybrid foundation

In the final stage, two centrifuge tests (Models 5-6) are carried out to traverse the performance of the proposed hybrid foundation (having both gravel drainage and friction piles) to mitigate the liquefaction-induced effects on shallow foundation resting on the liquefiable ground. Initially, the liquefiable ground is treated with gravel drainage Type 1, and friction piles in

Model 5 and then, the liquefiable ground is treated with gravel drainage Type 2 and friction piles in Model 6 as shown in Fig. 4.1.

EPWP time histories for Models 5 and 6 are presented and compared with EPWP time histories for Model 1 in Fig. 4.11. It is evident from Fig. 4.11 that the dissipation rate of EPWP increased because of the gravel drainage system. It is to be noted that the drainage capacity of the gravel drainage system is more in case of Model 6 than Model 5 as assigned. Larger the drainage capacity, faster is the dissipation of EPWP. For instance, at Level 3 (at P2, P3, and P4), the EPWP takes approximately 1000 s to dissipate in case of Model 1 (no gravel drains), whereas in case of Model 6, the EPWP dissipates within 600s. However, in the case of Model 5 (having gravel drainage Type 1), the dissipation rate of EPWP is almost similar to the Model 1. The reason for the inefficiency of gravel drainage Type 1 in the case of Model 5 is because of less drainage capacity as discussed earlier.

The maximum magnitude of EPWP at Level 4 (at P5, P6, and P7) in Model 6 is significantly less in comparison with respective EPWP in Model 1 as shown in Fig. 4.11. However, Fig. 4.5 depicts that the maximum magnitude of EPWP in case of Model 3 (having same drainage system as in Model 6) at Level 4 (at P5, P6, and P7) is almost same as those in case of Model 1. Although, Model 6 has the friction piles which has negligible effects on the evolution of EPWP. The reason associated with this is the shallower positioning of PPTS at Level 4. The positioning of PPTs at Level 4 are back-calculated using the hydrostatic pressure at 40g (before the shakings), and it is found that the PPTs were placed at approximately 8-9 mm (in model scale) shallower than the required depth. The targeted excess pore water pressure ratio (as described in Table 4.4) at liquefied zone within the ground could not be achieved in both Models 5 and 6 (except at Level 4 in case of Model 6) as the maximum magnitude of EPWPs for both Models 5 and 6, are almost similar to the one observed in Model 1. It should be noted that gravel drainage system both in the case of Models 5 and 6 could not avoid the model ground to be liquefied.
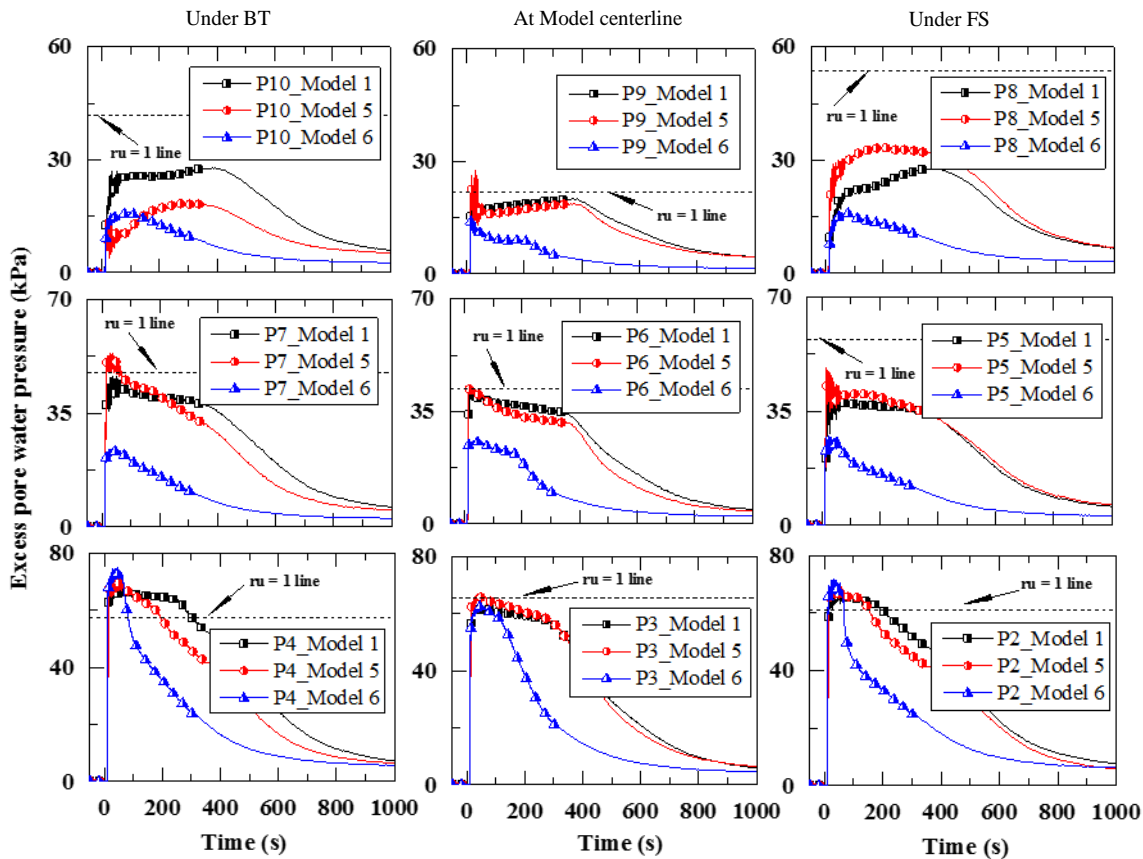
Fig. 4.11. Excess pore water pressure time histories of Models 1, 5 and 6 during Tokachi-Oki ground motion

Settlement time histories of both BT and FS foundations in Models 5 and 6 are presented and compared with the respective settlement time histories of Model 1 in Fig. 4.12. It is evident that the overall settlement of both BT and FS is significantly less in the case of Model 6 in comparison with Models 1 and 5. The gravel drainage system (Type 2) can mitigate the post-shaking settlement while the friction pile contributed to minimizing the co-shaking deformation of both footings. To examine the combined influence of gravel drainage system and friction piles, the cumulative settlement progression of footings at different time intervals is shown in Fig. 4.13 for Models 1 (no treatment), 3 (gravel drainage Type 2 only), 4 (friction piles only), and 6 (both gravel drainage Type 2 and friction piles). It is evident that the presence of gravel drainage minimized the post-shaking settlement (after 100s) in Models 3 and 6. Though the settlement during shaking is small in the case of Model 4 in comparison with Model 1 and 3; however, a comparatively large amount of settlement occurred after shaking in case of Model

4. The combined effects of both friction pile and gravel drainage (Type 2) are evident in case of Model 6 as the settlement occurred in all time intervals is significantly less in comparison with Models 1, 3, and 4.
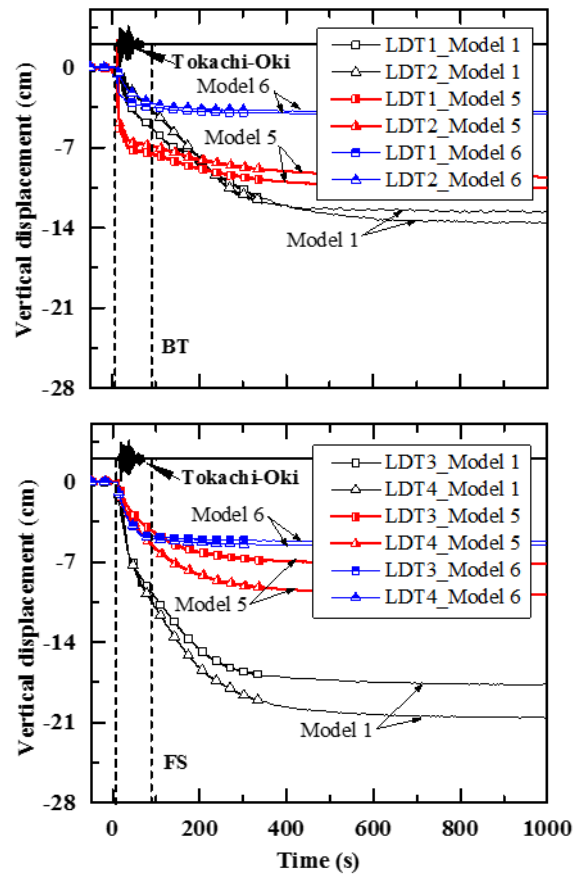
Fig. 4.12. Settlement time histories of BT (LDT1 and 2) and FS (LDT3 and 4) for Models 1, 5 and 6 during Tokachi-Oki ground motion
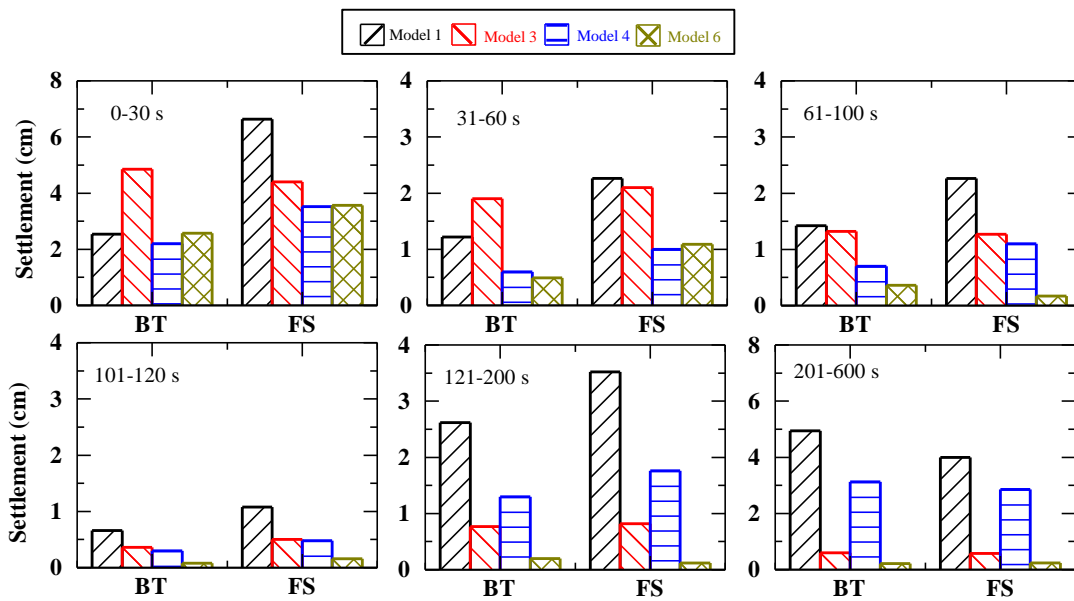
Fig. 4.13. Average settlement of BT and FS footings for different time periods during Tokachi-Oki ground motion

4.4 Summary

A unique hybrid foundation is proposed to mitigate the liquefaction-induced effects on a shallow foundation. The proposed hybrid foundation is a combination of gravel drainage and friction piles with spiral blades. The intended purpose of providing the gravel drainage is to mitigate the liquefaction-induced effects through rapid dissipation of EPWP. Moreover, friction piles are presumed to minimize the excessive settlement/tilting of the foundation system during the strong ground motion. The efficacy of the hybrid foundation to mitigate the liquefaction-induced effects on the shallow foundation is investigated using a series of dynamic centrifuge experiments. The development of hybrid foundation is carried out in three phases. In the first phase, an attempt is made to understand the behavior of shallow foundation on the liquefiable ground during Tokachi-Oki ground motion. In the second phase, the performance of gravel drainage system and friction piles are evaluated. Three types of model tests are performed for this purpose in which two model tests consist of the gravel drainage system of different drainage capacities, and one model test consists of only friction piles. In the third stage, the performance of hybrid foundation is investigated using two model tests. Each model test consists of the

friction piles and gravel drainage system of different drainage capacities as individually investigated in the second phase. It is found that the shallow foundation resting on the liquefiable ground is prone to undergo excessive settlement. Shear and volume change induced deformation dominate the overall settlement of the shallow foundation. Treating the ground with gravel drainage system found to be useful to mitigate the liquefaction-induced deformation. The presence of gravel drainage increased the dissipation rate (through radial flow towards the gravel drainage zone) of generated EPWP and reduced the post-shaking settlement. Centrifuge tests results depict that the friction piles having spiral blades at bottom served an excellent means of frictional resistance against the settlement of shallow foundation and reduced the overall deformation of shallow foundation significantly through combined inertial and kinematic interaction with foundation-superstructure and model ground. Overall, the hybrid foundation performs as expected to mitigate liquefaction-induced effects on shallow foundation during the strong ground motion.

Chapter 5. Efficacy of liquefaction mitigation techniques under different strong ground motions

The performance of induced partial saturation and proposed hybrid foundation to mitigate the liquefaction-induced effects on shallow foundations under Tokachi-Oki ground motion is discussed in Chapters 3 and 4, respectively. These mitigation techniques are found to minimize the liquefaction-induced effects during Tokachi-Oki ground motion. However, the alteration of the ground condition is apparent due to induced cyclic stress, shear-induced deformation, development of excess pore water pressure (EPWP), localized drainage, post-liquefaction reconsolidation, void re-distribution, and inertial and kinematic interaction within the soil-foundation-structure system. These factors may affect the effectiveness of liquefaction mitigation techniques under next strong ground motion. Any structure may experience several moderate to strong earthquakes during its lifespan. Therefore, the effectiveness of these mitigation techniques under various level of earthquakes is necessary to examine the long term efficacy of their performance to mitigate the liquefaction-induced effects.

Ground motion recorded at Hachinohe Port during the 1968 Tokachi-Oki earthquake (NS component) is used as the first dynamic excitation after the white noise (WN1). Enough time is given for full dissipation of EPWP before applying the second earthquake ground motion. Design earthquake motion for highway bridges in Japan (2-I-I-3, NS component) recorded at the ground surface near New Bansuikyo Bridge, Tochigi during the 2011 Tohoku Earthquake shown in Fig. 5.1 is applied to the model after that. Finally, the white noise (WN2, see Fig. 5.2) is applied after the Tohoku ground motion to examine the change in the fundamental characteristics of the ground-foundation-structure system with reference to WN 1 (Fig. 3.3). The results under the strong ground motion (Tohoku earthquake) are discussed with reference to the observations made during Tokachi-Oki ground motion (Chapters 3 and 4). The implications of two different strong ground motions on the performance of liquefaction mitigation techniques are also discussed in this chapter.
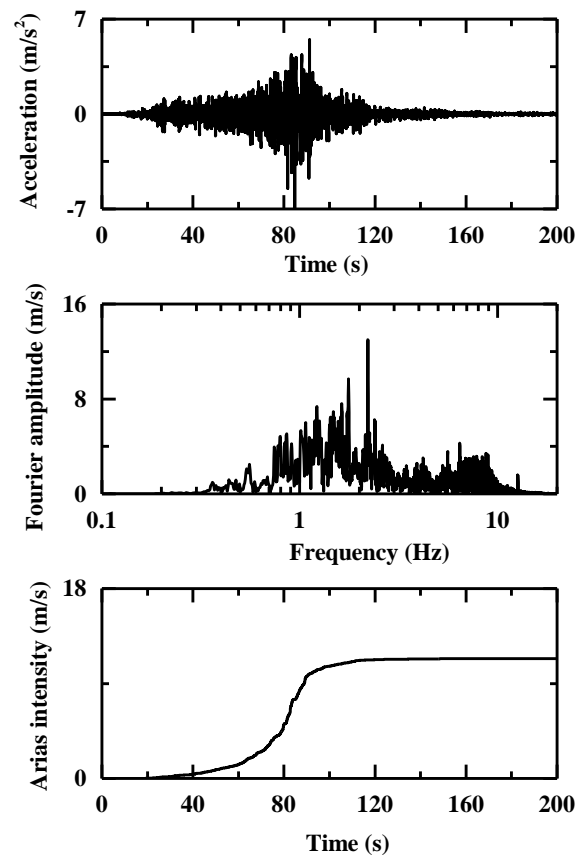
Fig. 5.1. Acceleration time history, Fourier spectra and Arias intensity of Tohoku earthquake applied as second ground motion
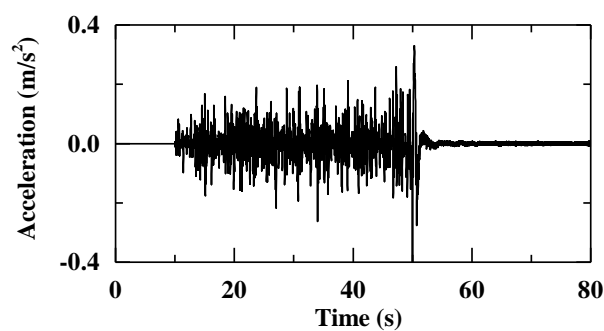
Fig. 5.2. Acceleration time history and Fourier spectra of input white noise (WN2)

5.1 Efficacy of induced partial saturation

Induced partial saturation is one of the novel techniques to increase the liquefaction resistance

of the saturated sandy ground. Nonetheless, a limited number of experimental studies are available on the delineation of this method. Moreover, the performance of induced partial saturation under a strong ground motion is poorly understood. In this subsection, the efficacy of induced partial saturation under the strong Tohoku earthquake is examined.

5.1.1   *Evolution of excess pore water pressure*

Fig. 5.3 depicts the EPWP time histories for both fully saturated and partially saturated model grounds when subjected to Tohoku ground motion. It is evident from Fig. 5.3 that whole model ground gets liquefied except in the vicinity of FS foundation (at P7) in case of fully saturated model ground. However, induced partial saturation can avoid the liquefaction state at P6 (Level 4) and P7 and P9 (Level 5) in case of the partially saturated model ground. During Tohoku ground motion, the overall performance of partially saturated ground is diminished in comparison with the one witnessed during Tokachi-Oki ground motion (Fig. 3.6). Tohoku earthquake is stronger than the Tokachi-Oki in terms of both peak acceleration and duration. Also, there is a considerable possibility that a few percentages of air voids might have disintegrated/dissolved during Tokachi-Oki earthquake because of pore fluid migration in the liquefied zone and due to the deformation of the model ground.

Pore pressure transducers (PPTs) at a shallower depth (P7-P9) exhibit maximum EPWP quite after the shaking period in case of partially saturated model ground during both Tokachi-Oki and Tohoku ground motion as shown in Figs. 3.6 and 5.3. The reason for this is the slower rate of water flow from the deeper portion of the model ground in case of partially saturated ground. It is to be noted that all PPTs show a small magnitude of the residual EPWP in dissipation phase at 5000 s except at P1. This is associated with the fact that the PPTs experienced a marginal settlement during the shakings which changed the overall void ratio (probably decreased) and the marginal rise of the water table. This inevitable settlement of PPTs during Tokachi-Oki ground motion changed the initial vertical effective stress condition at the location of PPTs for Tohoku ground motions. However, the initial vertical effective stress is assumed to be constant for both the ground motions (Tokachi-Oki and Tohoku earthquake) at different levels in the model ground as tabulated in Table 3.1 for the sake of brevity.
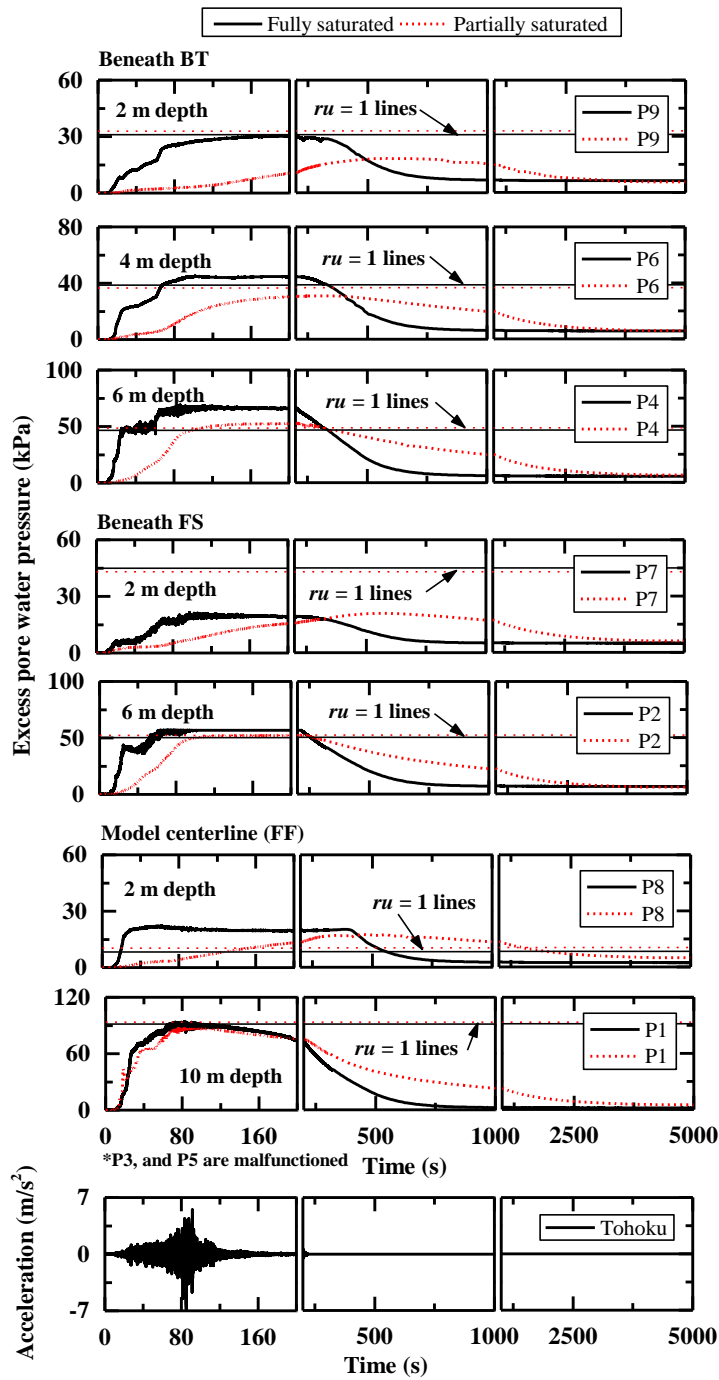
Fig. 5.3.   EPWP time histories obtained during Tohoku ground motion

5.1.2   *Air void dissolution/collapse during shakings*

Air voids are introduced using the drainage-recharge method to induce partial saturation within the model ground. It is to be noted that the model grounds are prepared in 1g condition, and the calculated degree of saturation is certain to change at 40g environment within the partially

saturated model ground. Introducing Boyle's law and assuming air voids to be isolated and soil grains to be incompressible, the distribution of the degree of saturation is estimated within the partially saturated model ground at 40g as shown in Fig. 3.7.

Fig. 3.7 depicted that the degree of saturation increases (significantly) at the deeper portion of the model ground due to high hydrostatic pressure condition. This is also confirmed by the evolution of EPWP, as explained earlier. There are two governing factors by which the induced partial saturation can increase the liquefaction resistance of the ground. The first factor is the increase in the compressibility of the pore fluid due to the air voids entrapped within the pore fluid. This mechanism helps to restrict the rate of development of EPWP during cyclic loading, which is also witnessed during the EPWP build-up stage in the experiment as depicted from Figs. 3.6 and 5.3. The second one is matric suction which is not significant in the case of liquefiable soil, as explained by Bishop and Blight (Bishop and Blight, 1963). By implementing the above stated Boyle's law, the maximum potential volumetric compressibility (strain) within the model ground can be estimated using the evolution of EPWP during the shaking (Okamura and Soga, 2006; Marasini and Okamura, 2015; and Kumar et al., 2019a).

Let's consider a fully saturated soil mass comprising incompressible soil particles and pore fluid. For a small change in pressure, the volumetric strain in soil mass will be zero under undrained condition. However, the soil mass with air voids (partially saturated case) will undergo considerable volumetric strain (potential volume compressibility) under the same conditions. This potential volume compressibility of soil mass is solely due to the inclusion of air voids as the water and sand particles are assumed to be incompressible. The empirical equation proposed by Okamura and Soga (2006) is used to estimate the potential volumetric compressibility which required the parameters such as the degree of saturation (Fig. 3.7), initial vertical effective stress (Table 3.1), maximum EPWP, and the initial void ratio.

Fig. 5.4 shows the maximum potential volume compressibility because of air voids induced within the partially saturated model ground during white noise 1 (WN1, before Tokachi-Oki ground motion) and white noise 2 (WN2, after Tohoku ground motion). The maximum potential volumetric strain depends on several factors such as void ratio, the evolution of EPWP, dynamic shaking, vertical effective stress and degree of saturation. Considering these factors and to evaluate the available potential volumetric compressibility before and after the main shakings, four locations (at P2, P4, P5, and P6 as shown in Fig. 3.1) are considered during the white

noises. The reason for selecting pore pressure locations at Levels 3 and 4 (at P2, P4, P5, and P6) is to avoid/minimize the influence of an abrupt change in void ratio and degree of saturation during and after the shaking. Both white noise shakings (WN1 and WN2) are alike as shown in Fig. 5.4 and possess almost the same intensity.
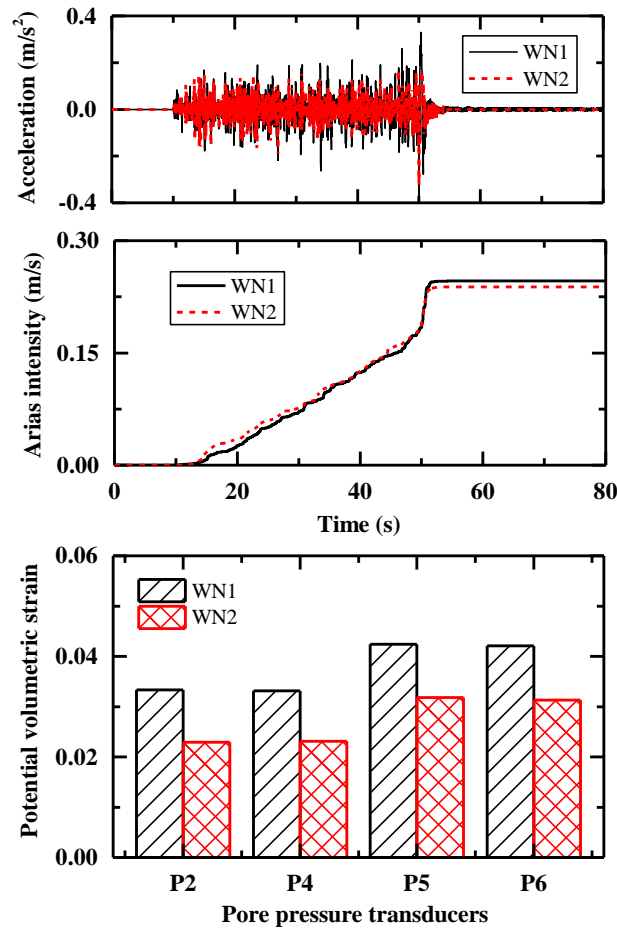
Fig. 5.4. Maximum potential volumetric strain during white noise 1 (WN1) and white noise 2 (WN2)

It is evident from Fig. 5.4 that the availability of maximum potential volumetric compressibility because of induced air voids during WN1 is relatively more than the one available during WN2. This is associated with the fact of air void dissolution/collapse during Tokachi-Oki and Tohoku ground motion which is also witnessed from the EPWP time histories (Fig. 5.3) as explained earlier. However, the available capacity of potential volume compressibility is quite significant even after the strong Tohoku ground motion (corresponds to

WN2) which signifies the novelty of induced partial saturation to increase the liquefaction resistance of the partially saturated ground.

5.1.3   Settlement behavior

Fig. 5.5 depicts the settlement observed at BT and FS footings during Tohoku ground motion. In case of fully saturated ground, both BT and FS experienced collapse kind of behavior (from the visual inspection after the experiment, it is found that both BT and FS had struck to the surrounding guide plate). During Tokachi-Oki ground motion, BT footing exhibits the significant amount of differential settlement in the direction of LDT1 in case of fully saturated ground, as explained in Chapter 3. The rotational tilting (as it seems to have happened from Fig. 5.5) occurred after the Tohoku ground motion, and BT footing concludes with excessive differential settlement by the side of LDT2. This unusual behavior of BT during Tohoku ground motion in case of the fully saturated model ground might have happened because of the soil flow (traces were observed after the experiment) over the location of LDTs 1, 2 and 4 during Tohoku ground motion because of liquefaction. In that case, the LDTs (1, 2 and 4) readings, especially after the soil overflow (dashed lines in Fig. 5.5), are not reliable in case of fully saturated model ground for Tohoku ground motion. It is evident from Figs. 3.10 and 5.5, that the overall performance of the partially saturated ground for both the footings and associated superstructures is better than the fully saturated ground even under different strong ground motions
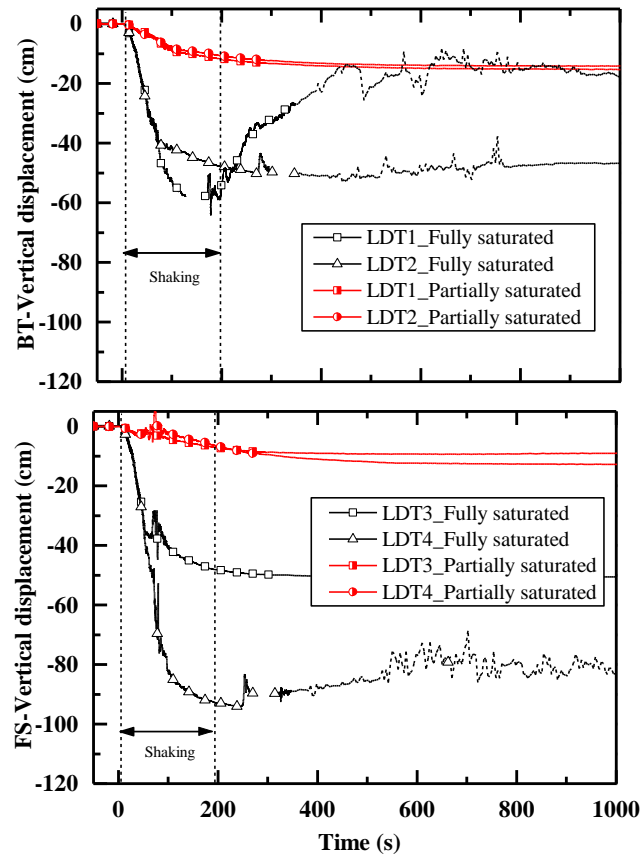
Fig. 5.5.   Settlement time histories of BT (LDT1 and 2) and FS (LDT3 and 4) during Tohoku ground

Fig. 5.6 shows the cumulative average settlement of BT and FS footings during and after the shakings. It is evident that footings undergo significant co-shaking settlement (settlement occurred during shaking) in case of fully saturated model ground during Tohoku ground motion. Shear-induced deformation is the governing factor for co-shaking settlement, and it can be seen from Fig. 5.6 as the overall vertical settlement of FS is significantly large compared to the vertical settlement of BT. The shear strength of soil in the vicinity of the foundation start to mobilize because of the generation of EPWP (reduction in mean vertical effective stress), and hence shear-induced co-shaking settlement is apparent. The induced partial saturation can mitigate the shear-induced deformation as the co-shaking settlement in case of the partially saturated ground is less in comparison with the fully saturated ground. Volumetric strains due to partial drainage and development of post-liquefaction/shaking reconsolidation strains are the prime responsible factors associated with the post-shaking settlement. It is evident from Fig.

5.6 that the post-shaking settlement is significantly mitigated by the presence of air voids in case of partially saturated model ground. Unfortunately, the post-shaking readings of LDTs in case of the fully saturated ground are not reliable during Tohoku ground motion as discussed earlier and hence are not shown in Fig. 5.6.
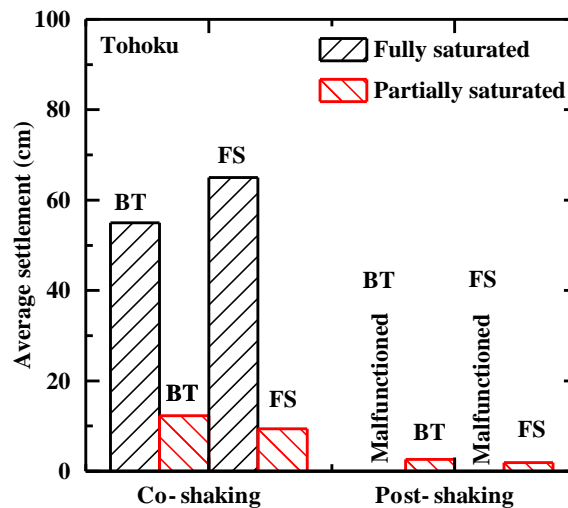
Fig. 5.6. Co-shaking and post-shaking settlement during Tohoku ground motion
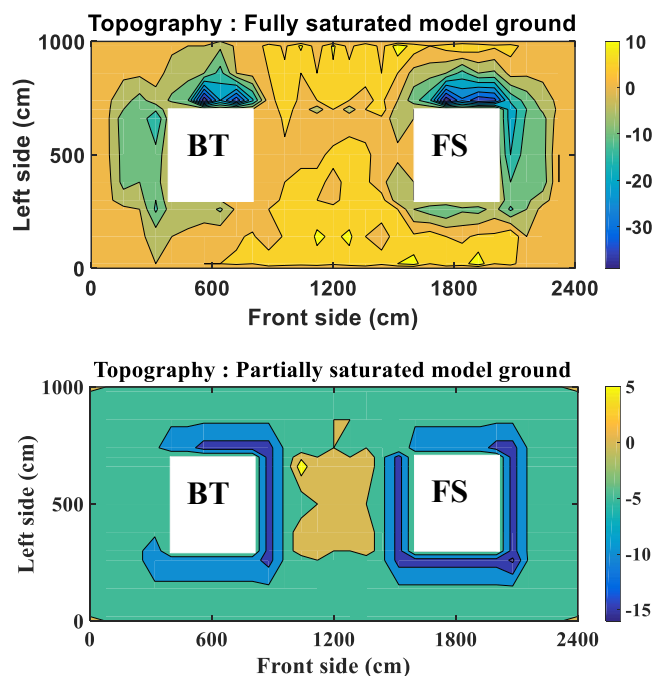
Fig. 5.7. Topography (surface settlement in cm) after the centrifuge experiment

Fig. 5.7 depicts the surface settlement (topography) measured after the centrifuge experiments. The surface settlement is shown in Fig. 5.7 is the cumulative response during all the shakings (WN1, Tokachi-Oki, Tohoku, and WN2). Larger the bearing pressure more is the settlement in the vicinity of the foundation for both fully saturated and partially saturated ground. It is evident that the overall surface settlement is significantly less in case of partially saturated ground in comparison with the fully saturated ground.

5.1.4   *Kinematic and inertial interaction between the model ground-foundation-structure system*

Fig. 5.8 depicts the acceleration time histories recorded at several locations on/within foundation-superstructure and model ground (see Fig. 3.1). Acceleration records measured at A5 showed the significant amount of de-amplification in acceleration time histories for both fully saturated and partially saturated model grounds during Tohoku ground motion. Significant de-amplified acceleration time history of A5 also consolidate the fact that the model ground exhibits considerable softened state during Tohoku ground motion. Similar observations are made in Chapter 3. The partially saturated ground shows relatively less de-amplification in comparison with the fully saturated ground at all locations except at A7 and A9 in case of Tohoku ground motion. This explains that the partially saturated model ground exhibits more liquefaction resistance (relatively less model ground softening) in comparison with the fully saturated model ground. Similar observations of acceleration records were made by Zeybek and Madabhushi (2017). During Tohoku ground motion, acceleration time histories recorded at the foundation and superstructure of FS (A7 and A9) showed the spikes in case of fully saturated ground. The reason for this might be the excessive settlement of the foundation (Dashti et al., 2010). Also, larger acceleration spikes at the FS might be observed because of soil dilation and re-stiffening caused by excessive soil flow under the shallow foundation.

To examine the influence of the kinematic and inertial interaction on foundation, Fourier amplitude spectra (FAS) of acceleration records at footings and far-field is obtained, as shown in Fig. 5.9. The FAS representation of acceleration records can give an insight of amplification/attenuation between fully saturated and partially saturated ground at respective locations. The frequency content can be divided into two ranges; i.e., acceleration dominating (Fa) and velocity dominating (Fv) range, as suggested by Borcherdt (1994).
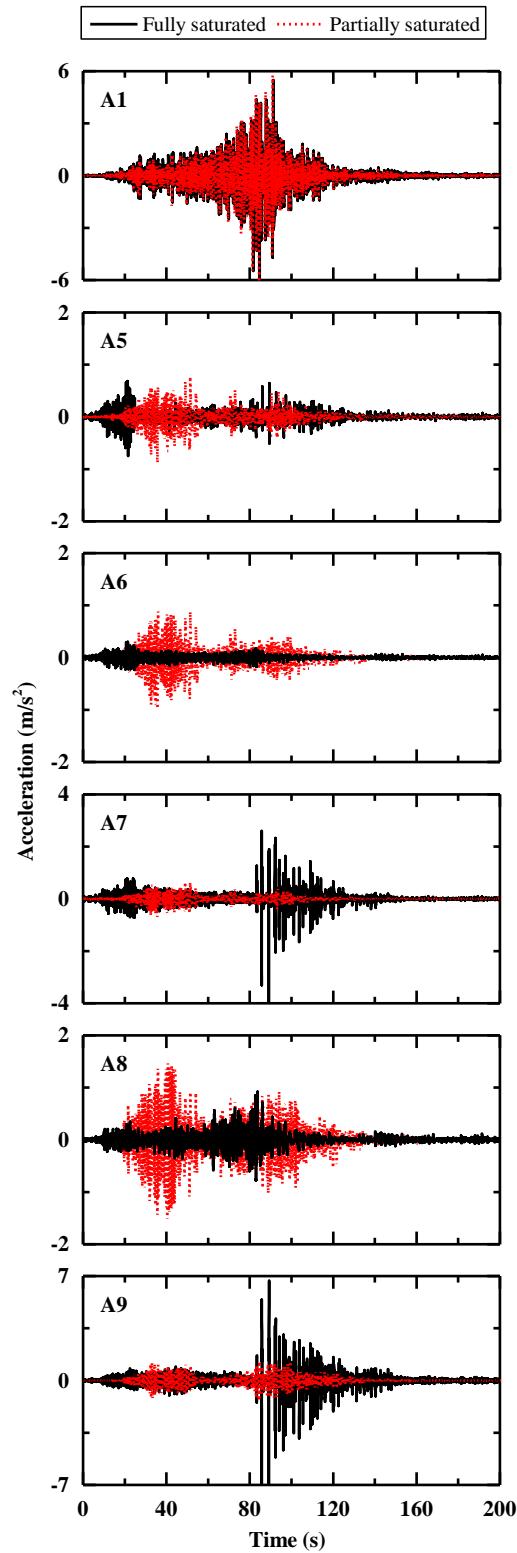
Fig. 5.8. Acceleration time histories during Tohoku ground motion

It is evident that the FAS amplitudes for FF and BT are significantly large in case of

partially saturated model ground in comparison with the fully saturated ground during both Tokachi-Oki and Tohoku ground motions. The observed amplification is dominating in the *Fv* frequency (0.5–2.0 Hz) range. This demonstrates that the partially saturated ground yield amplified seismic demand to the model ground-foundation system. However, the FAS trend for FS footing seems to be alike for both fully saturated and partially saturated grounds during Tokachi-Oki ground motion. Although, a marginal attenuation in FAS is observed for high frequency in case of partially saturated ground. The reason for this is the same model ground condition in the vicinity of FS footing as the degree of saturation is almost same for both fully saturated and partially saturated ground.
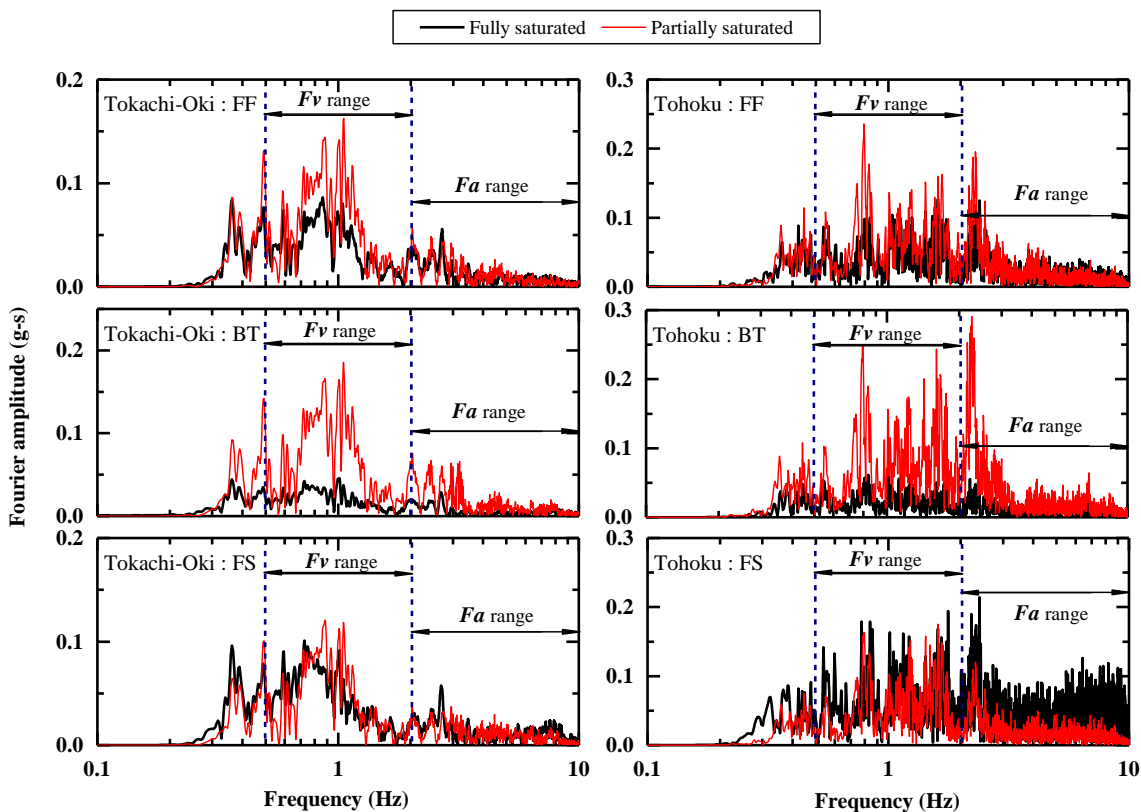
Fig. 5.9.   Fourier amplitude spectra of acceleration recorded at footings of BT and FS and free field

5.1.5   *Strength/stiffness mobilization of model ground*

Fig. 5.10 depicts transfer functions (TFs) during white noise 1, Tokachi-Oki, and Tohoku ground motions. The ratio of acceleration records at A5 to A1 in the frequency domain is used

to obtain the TFs. It is evident that the fundamental site frequency obtained for both fully saturated and partially saturated grounds during white noise 1 falls within the range of small-strain site fundamental frequency obtained by empirical equations (Hardin and Drnevich, 1972), even though the soil response is highly nonlinear. This also implies that the fundamental site frequency of the model ground could be captured by appropriate white noise (usually a random small amplitude vibration having equal intensities at different frequencies, giving it a constant power spectral density).
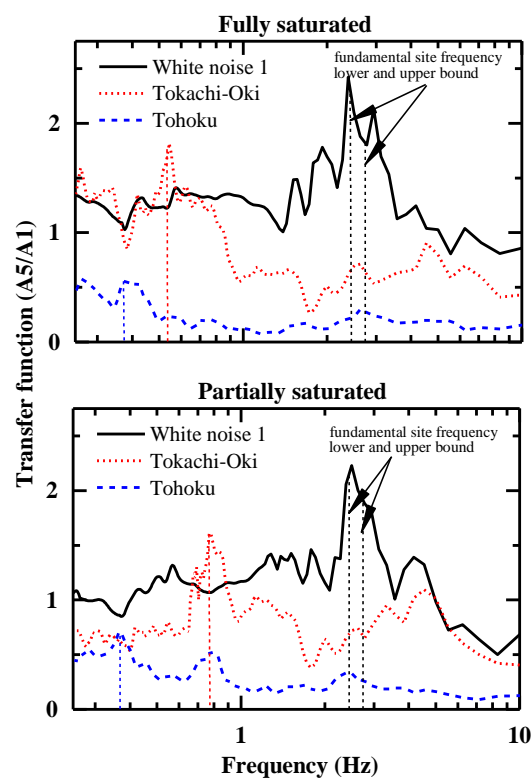
Fig. 5.10. Far-field model ground behavior during white noise, Tokachi-Oki and Tohoku ground motion

Shear wave velocity profile (within the ground using small strain shear pulse) is used in empirical equations to estimate the fundamental site frequency. The upper and lower bound of the fundamental frequency of the model ground (2.5-2.8 Hz) is determined by the estimated range of shear wave velocity (approximately 169 to 186 m/s) using empirical equations as mentioned above. Site fundamental frequencies obtained during Tokachi-Oki ground motion falls to 0.54 and 0.8 Hz for the fully saturated and partially saturated model ground respectively.

The significant drop in site fundamental frequency occurred because of the softening of the model ground during Tokachi-Oki ground motion (Arulanandan and Scott, 1993). It is evident that the extent of model ground softening is relatively small in case of partially saturated ground in comparison with the fully saturated ground. However, both the model grounds exhibit a nearly same trend of TFs during Tohoku ground motion.
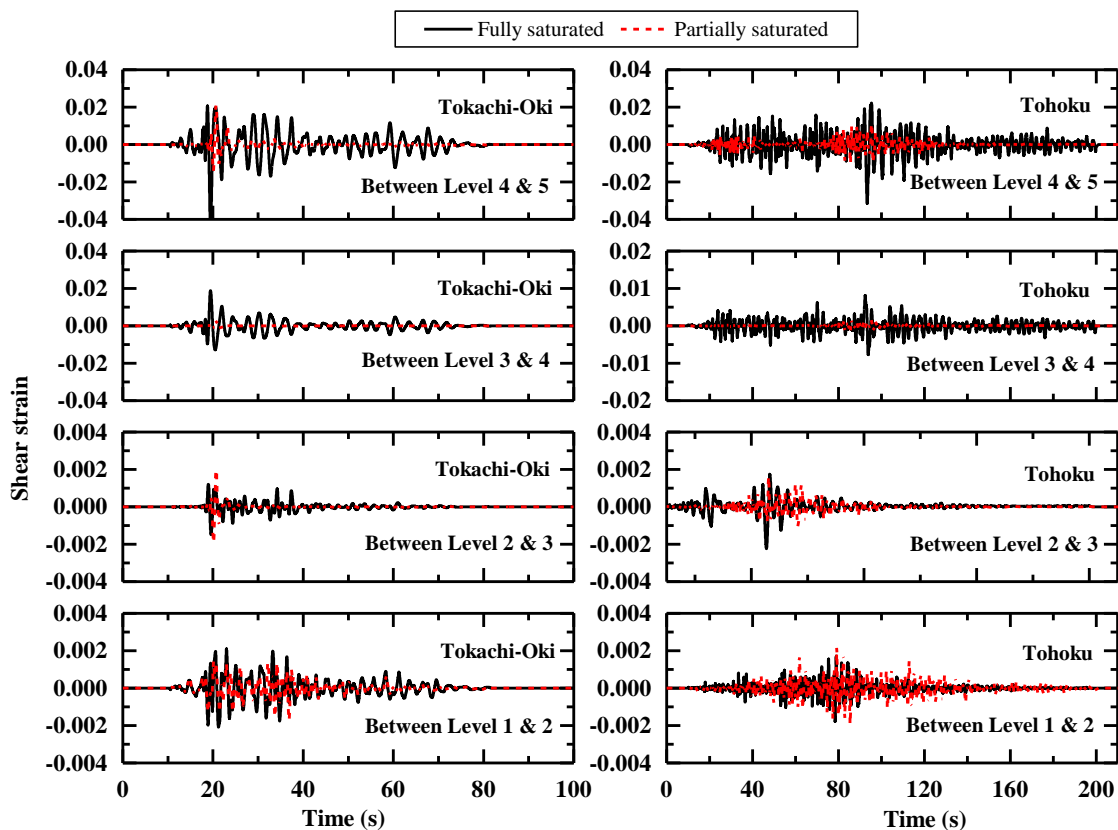
Fig. 5.11. Shear strain time histories for model centerline (MC) between different levels

Back analysis of acceleration records, is performed to get the insight into the progression of shear strain within the model ground. Many studies justify the credibility of this method. Zeghal et al. (1999); Adalier and Elgamal (2002) used the recorded lateral accelerations to evaluate shear stress and strain histories at different elevations within the ground. Brennan et al. (2005) assessed the shear modulus and shear degradation curves for dry and saturated sand, soft clay from the acceleration histories obtained from the centrifuge tests. Fig. 5.11 depicts the shear strain developed along the centerline of the model ground between different levels (as mentioned in Table 3.1) during the centrifuge test for fully saturated and partially saturated

grounds. At a shallower depth (between Levels 4 and 5), the shear strain developed within the partially saturated ground is significantly less in comparison with the fully saturated ground. Similar behavior is observed between Levels 3 and 4. This behavior corroborates the fact that inclusion of air voids within the ground increases the liquefaction resistance of the ground. However, shear strain time histories between Levels 2-3 and Level 1-2 are alike for both fully saturated and partially saturated grounds. The presence of air voids seems to have negligible effects at the deeper portion. EPWP time histories obtained at the deeper portion (Figs. 3.6 and 5.3) also delineate the limitation of the presence of the air voids under higher stress level.

5.2 Efficacy of hybrid foundation

5.2.1   *Evolution of excess pore water pressure*

The efficacy of hybrid foundation (Models 5 and 6, see Fig. 4.1) is evaluated with reference to the liquefaction-induced effects on the shallow foundation during Tokachi-Oki ground motion as discussed in Chapter 4. Time histories of EPWP at different locations are shown in Fig. 5.12 during Tohoku ground motion. Fig. 5.12 depicts a similar response, as observed in Fig. 4.11. It is to be noted that the presence of gravel drainage both in case of Models 5 and 6, could not avoid the model ground to be liquefied. However, because of rapid drainage, EPWP remains in development state for a shorter time in case of Model 6 in comparison with Models 1 and 5. In addition, the performance of gravel drainage seems to be diminished in terms of both generation and dissipation of EPWP during Tohoku ground motion in comparison with Tokachi-Oki ground motion.

The effect of friction piles (in case of Models 5 and 6) on the evolution of EPWP can be made with reference to the EPWP trends observed for Models 2 and 3 (see Fig. 4.5). As the gravel drainage system in case of Models 2 and 3 is same as for Models 5 and 6, the deviation of EPWP time histories presented in Figs. 4.11 and 5.12 from the corresponding EPWP time histories presented in Fig. 4.5 exhibits the influence of friction piles on the evolution of EPWP.
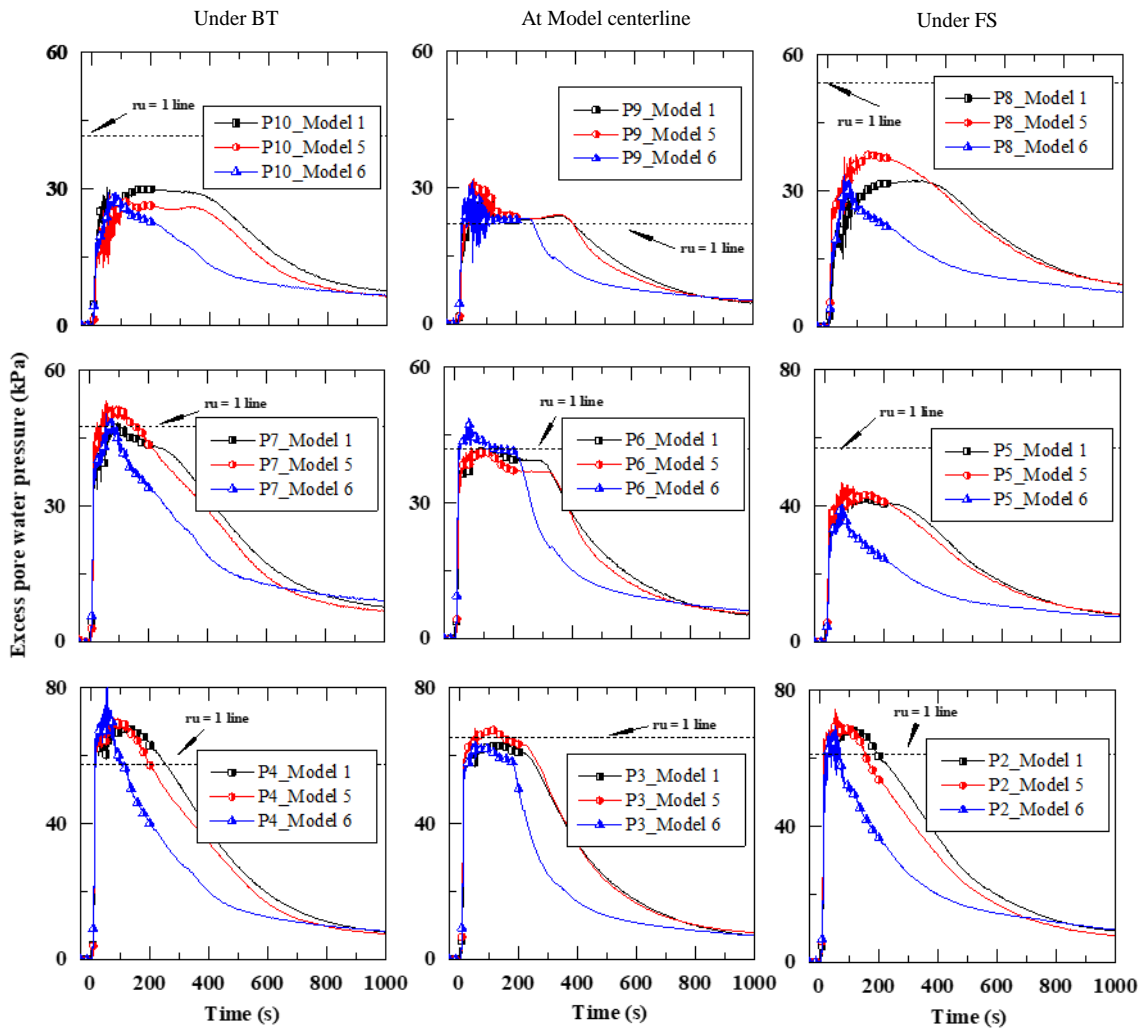
Fig. 5.12. EPWP time histories of Models 1, 5 and 6 during Tohoku ground motion

At level 3 (P2, P3, and P4), EPWP time histories are alike both in Models 2, 3, 5 and 6 during Tokachi-Oki ground motion which indicate that the presence of friction piles does not affect the EPWP at the deeper portion. However, at Level 4 (P5, P6, and P7), the maximum magnitude of EPWP in case of Model 6 is significantly less than the one observed in the case of Model 3. There might be many factors associated to less magnitude of EPWP at Level 4 in case of Model 6 during Tokachi-Oki ground motion, such as placing of PPTs very close to gravel drains, better performance of gravel drains, and comparatively shallower positioning of PPTs in case of Model 6. This explanation might also hold true for the less observed EPWP at Level 5 (P8, P9, and P10) dominatingly in case of Model 6 (at P10 for Model 5 as well). In addition, there might be a possibility of change in stress condition below the footings in case of

Model 6 because of subsidence. Noted that the friction piles pass through the footings with a marginal clear spacing of 0.5 mm (model scale). The jamming of soil particle in the gap (which is observed after the experiment) might have restricted the intended free vertical movement of footing, causing the subsidence condition below the footing. In that case, the significant amount of stress from foundation structure is transferred through the friction piles resulting in comparatively less stress condition at the shallower portion. However, this assumption does not hold true for P6 and P9 (along model centerline) which also show the less value of EPWP in case of Model 6. During Tohoku ground motion, the EPWP time histories are more or less same for all Models 2, 3, 5, and 6 which indicate that the deviation in EPWP time histories because of the presence of friction piles during Tokachi-Oki ground motion might be merely a coincidence.

5.2.2   *Settlement behavior of foundation*

Fig. 5.13 depicts the settlement behavior of BT and FS during Tohoku ground motion. The initial condition of the model ground-foundation system during Tohoku ground motion altered because of deformation occurred during Tokachi-Oki ground motion. This alteration significantly influenced the differential settlement behavior of both BT and FS foundation during Tohoku ground motion. The reasons for the fluctuation in the settlement recording during shaking, as shown in Fig. 5.13 might be the movement of the sensor holder/plate as such fluctuations were not observed in all sensors during Tokachi-Oki ground motion. Settlement time histories for Model 6 during Tohoku ground motion as depicted in Fig. 5.13 is a little unusual. The sudden jump in settlement time histories of LDTs 1 and 2 at 500 seconds is evident, which may have occurred because of soil flow over the footing during Tohoku ground motion which is witnessed after the experiment (see Fig. 5.14). Excessive settlement in case of Model 6 might be associated with the localized development of excessive volumetric strains in the vicinity of footings (also resulted in soil flow over the footing) which increased the shear-induced deformation. In addition, sometimes the higher rate of dissipation might cause the development of large settlement if the ground is liquefied during shaking. The performance of hybrid foundation seems to be diminished in terms of the overall settlement of both BT and FS footings in case of Model 6 during Tohoku ground motion whereas the evolution of EPWP within the model ground indicates otherwise.
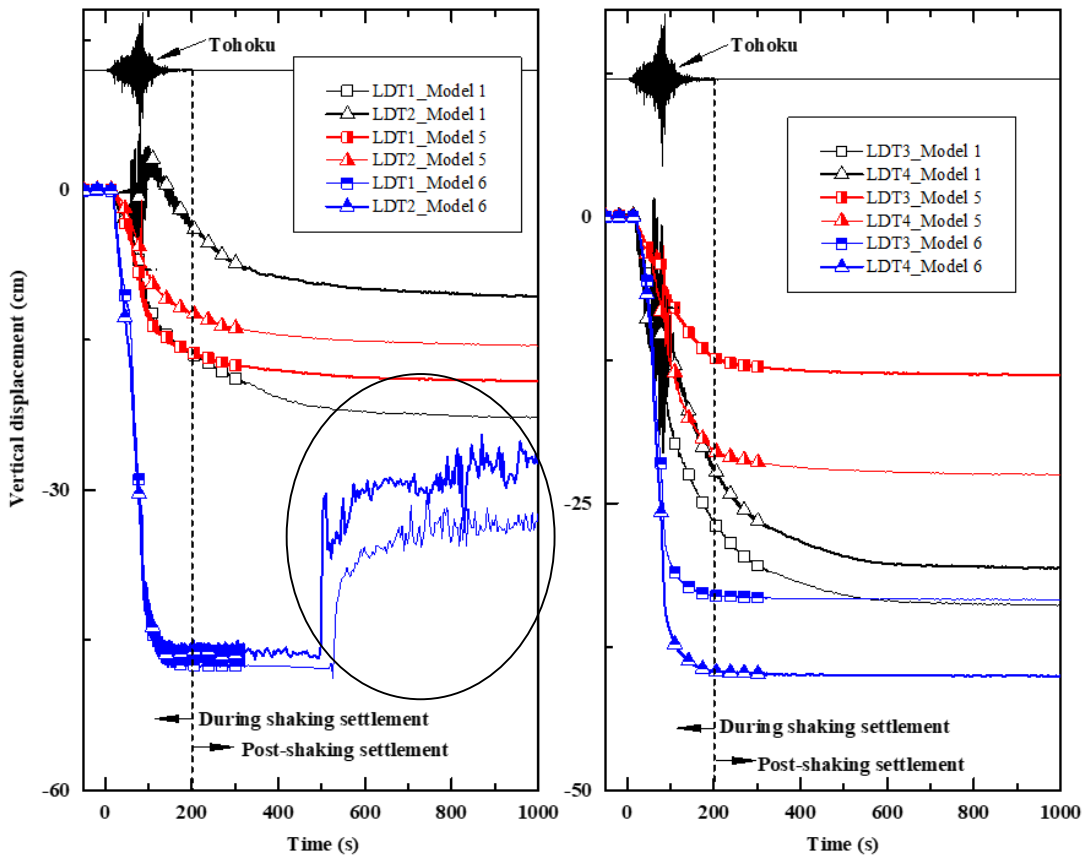
Fig. 5.13. Settlement time histories of foundations during Tohoku ground motion

Fig. 5.14. Model ground surface after the experiment. Pinching of target plates and trace of water flow is visible.

5.2.3   Model ground behavior

Fig. 5.15 depicts the TFs during white noise, Tokachi-Oki, and Tohoku ground motion. The ratio of acceleration records at A5 to A1 in the frequency domain is used to obtain the TFs during shaking. Recorded acceleration time histories are modified using filtering and baseline correction before calculating the transfer function. Filtering is performed in the frequency domain using the band-pass Butterworth filter with corner frequencies of 0.3Hz and 10 Hz respectively. It is evident that the site fundamental frequency obtained for Models 1, 5, and 6 during white noise falls under the range of small-strain site fundamental frequency obtained by empirical equations (Seed and Idriss, 1970; Hardin and Drnevich, 1972), despite the fact that the soil response is highly nonlinear. This also implies that the site natural frequency could be captured by appropriate white noise (usually a random small amplitude vibration having equal intensities at different frequencies, giving it a constant power spectral density).
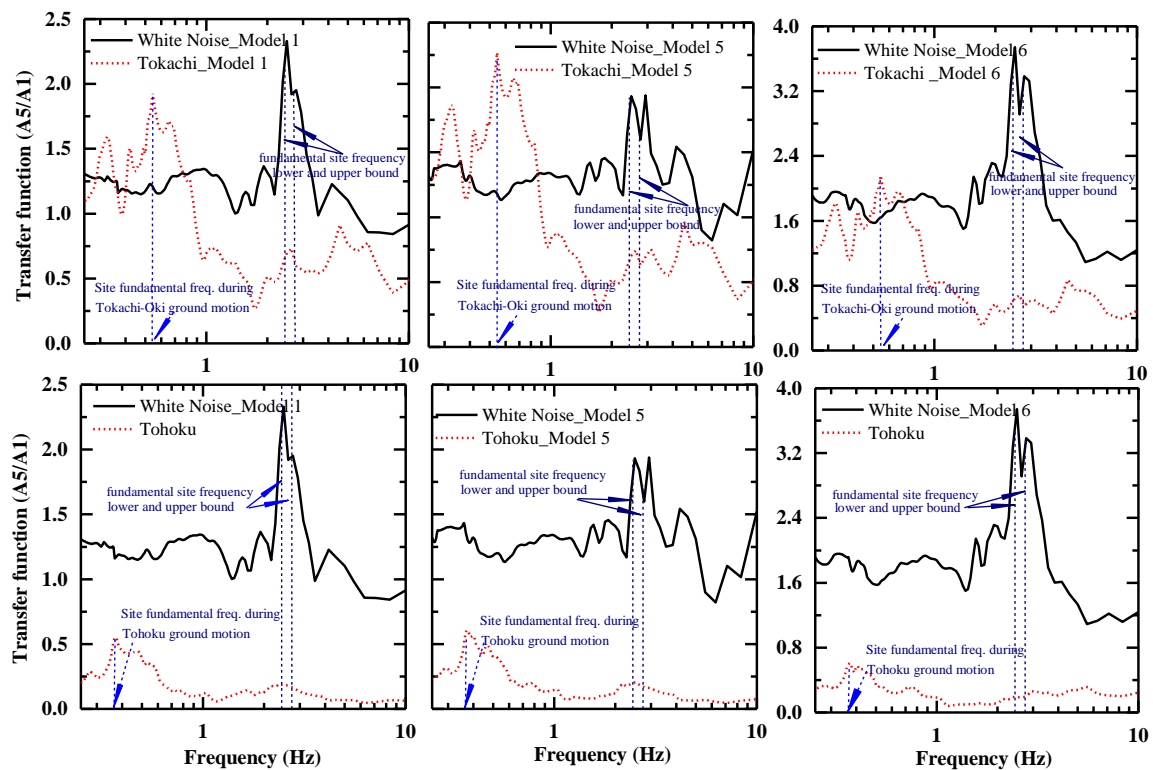
Fig. 5.15. Model ground behavior during white noise, Tokachi-Oki and Tohoku ground motion

The empirical equations use the shear wave velocity profile (within the ground using small

strain shear pulse). The upper and lower bound of natural frequency is determined by the observed range of shear wave velocity using empirical equations, as mentioned above. The maximum magnitude of peaks of TFs gives an indication of model ground stiffness (in other words, the relative density). The relative density of Model 6 is highest among Models 1 and 5 (Table 4.3), which is also evident from the TFs trends during white noise, as shown in Fig. 5.15. The site fundamental frequencies obtained during Tokachi-Oki ground motion falls down in the range of 0.53-0.57 Hz for Models 1, 5, and 6. The significant drop in site fundamental frequency is because of the softening of the model ground due to shear strength mobilization during Tokachi-Oki ground motion (Arulanandan and Scott, 1993). The drop in the site natural frequency is similar in Models 1, 5, and 6, which might be attributed to the fact that the liquefaction extent within the model ground at far-field is alike even after employing the hybrid foundation (in Models 5 and 6). This apprises the limitation of the proposed hybrid foundation, which is solely related to the performance of gravel drainage system. There are many reasons associated with the observed inefficiency of gravel drainage to avoid/minimize the liquefaction extent within the model ground. The design charts proposed by Seed and Booker (1977) based on which, the design of gravel drainage system for the hybrid foundation is carried out, largely overestimate the performance of gravel drainage (Boulanger et al., 1998; Adalier et al., 2003; Rollins et al., 2004; and Bouckovalas et al., 2006). Although the gravel drainage system is designed keeping in mind the intensity and severity of Tohoku ground motion; however, it seems that the designed gravel drainage system is not able to achieve the intended drainage performance during Tohoku ground motion.

Excessive drop in natural frequency of the model ground and significant de-amplified peaks observed in transfer functions, as shown in Fig. 5.15 exhibits the enormous extent of liquefaction state during Tohoku ground motion. This also indicates the limitation of gravel drainage capacity to avoid/minimize the liquefaction extent during strong Tohoku ground motion. It is to be noted that the acceleration records are only taken along the model centerline (MC) not under the BT or FS under which hybrid foundation is employed in case of Models 5 and 6. Hence, judging the performance of Models 5 and 6 from the acceleration records taken along MC might be an underestimation of performance of the hybrid foundation.

5.2.4 Foundation-structure response

During the dynamic excitation, soils undergo deformation, which is offloaded to the foundations. During the seismic loading, the wave propagates through the soil media, which altered in the vicinity of the structure and eventually structural response altered by the compliance of surrounding soil. This well-known phenomenon of soil-structure interaction plays a vital role in understanding the structure behavior on the liquefiable ground. Inertial interaction is not significant in the case of the liquefiable ground because the soil is assumed to behave as a seismic isolator to the foundation (Karamitros et al., 2013). However, superstructure's dynamic properties that control inertial interaction (e.g., mass, stiffness, and height/width) have been showing to influence the pore pressure, settlement trend, tilt potential, which in turn, influence the overall performance of superstructure (Sancio et al., 2004). Structure fundamental frequencies are calculated using white noise small strain shaking, as shown in Fig. 5.16. The transfer functions are obtained at footing and superstructure's lumped mass for both BT and FS during Tokachi-Oki and Tohoku ground motion. The ratio of acceleration records at A6, and A7, to A1 for BT and FS footing respectively and the ratio of A8, and A9 to A1 for BT and FS superstructure's mass respectively in the frequency domain is used to obtain the TFs during shaking as shown in Figs.5.17 and 5.18.
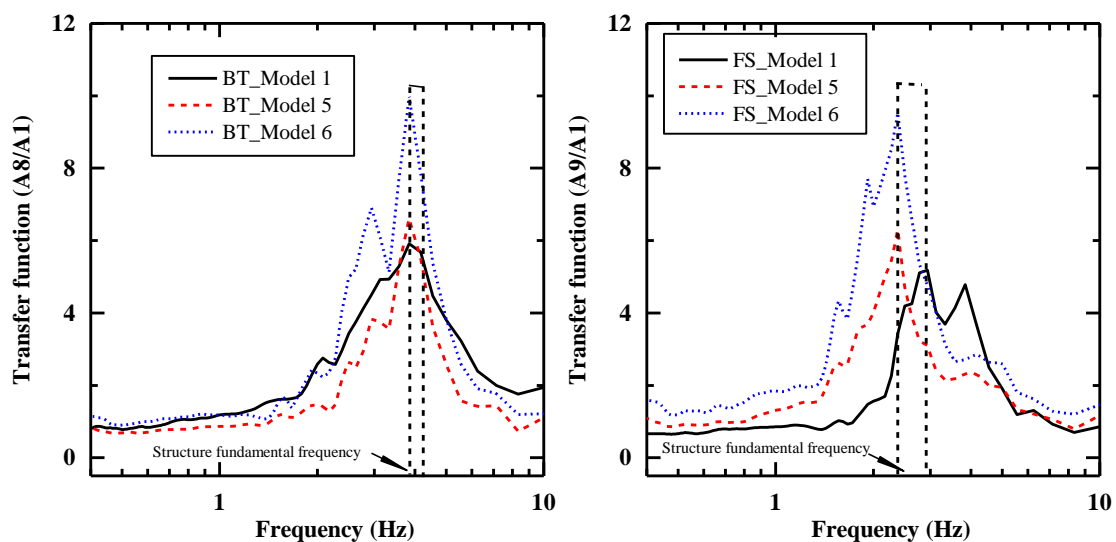
Fig. 5.16. Structure fundamental frequencies obtained during white noise

Fig. 5.17 depicts the transfer function obtained associated with footing and superstructure's lumped mass of both BT and FS during Tokachi-Oki ground motion. It is evident that the overall seismic demand observed in case of Model 6 is large in comparison with Models 1 and 5 at footings; though, no clear trace of magnified seismic demand at superstructure is observed for Model 6 at higher frequency range.

Fig. 5.18 shows the structural response during the Tohoku ground motion. Significant de-amplification in seismic intensity is observed at the footings of Both BT and FS. This is associated with the development of liquefied state (leading to comparatively large ground softening) within the model ground during strong Tohoku ground motion. However; for superstructures, the explicit trace of amplification/de-amplification is undulating in the presented frequency range.

5.2.5 *Foundation settlement progression*

Average settlement of BT and FS footings for different time intervals during Tokachi-Oki and Tohoku ground motion is shown in Figs. 5.19 and 5.20. The purpose of this illustration is to get an insight into the settlement progression of the shallow foundation. Each graph shows the average settlement of footings; i.e., the average of LDTs 1 and 2, and LDTs 3 and 4; corresponding respectively for BT and FS during different time intervals. The time intervals are selected to capture the overall settlement progression during co-shaking and post-shaking event.
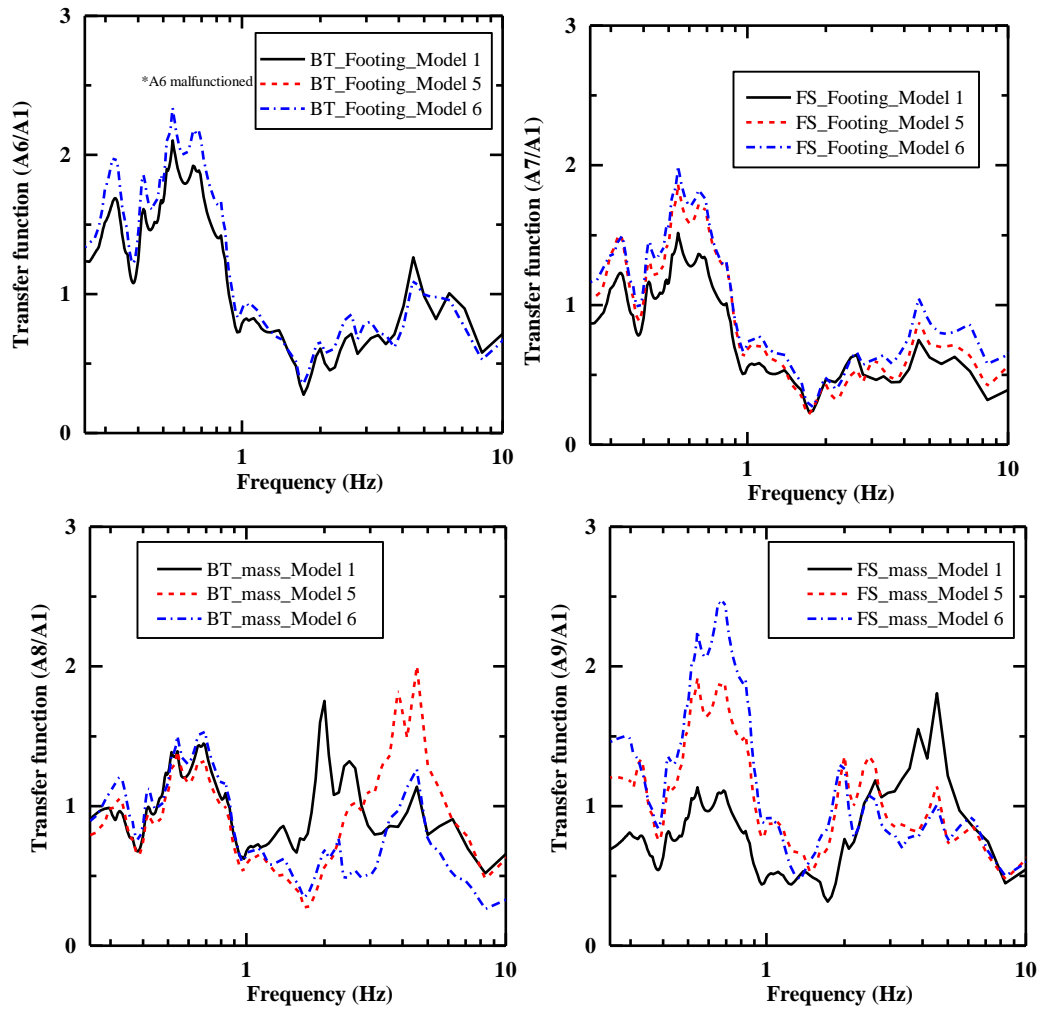
Fig. 5.17. Foundation-superstructure kinematic response during Tokachi-Oki ground motion
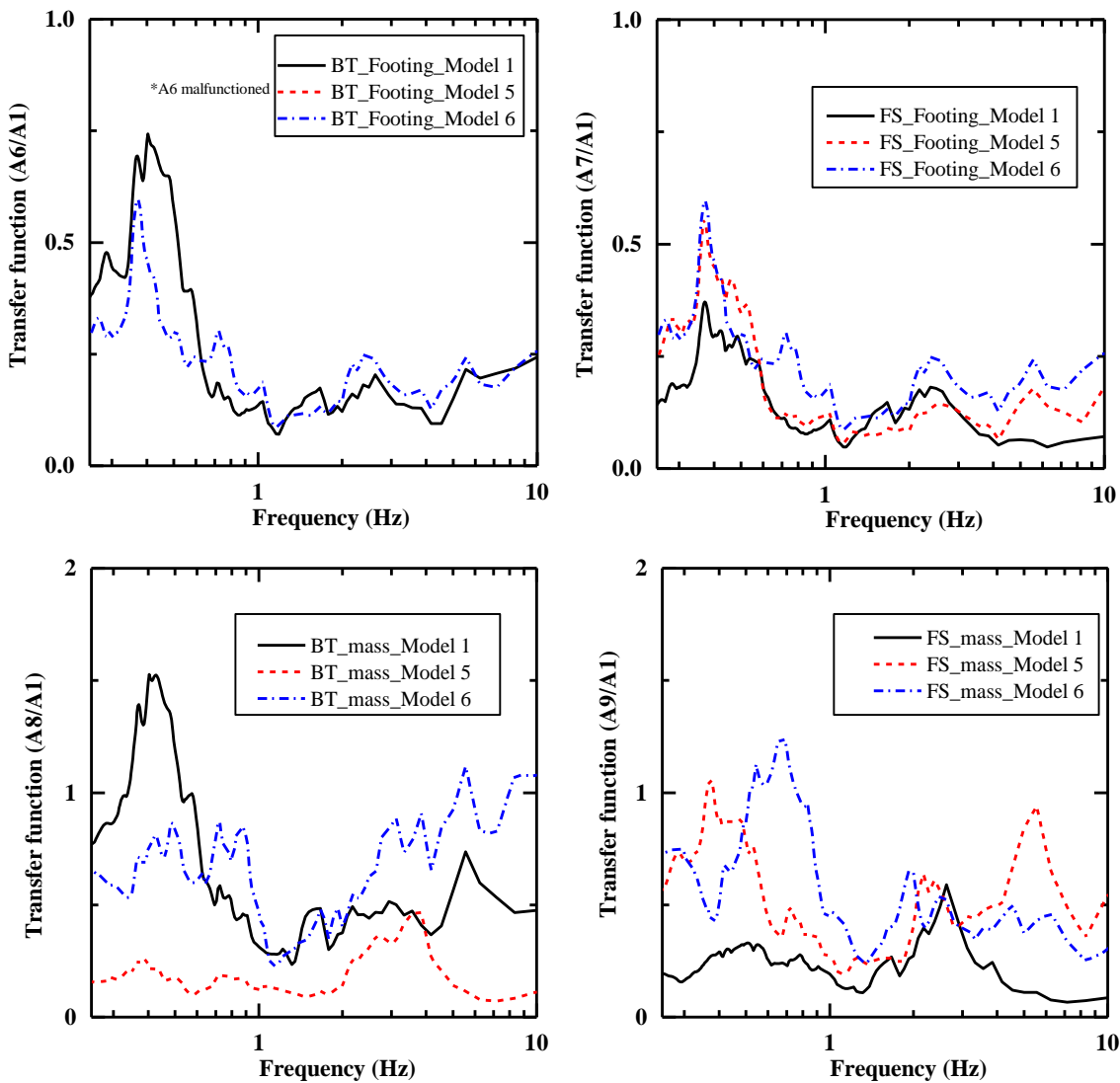
Fig. 5.18. Foundation-superstructure kinematic response during Tohoku ground motion

Effectiveness of gravel drainage system and friction piles to minimize the settlement of both BT and FS during co-shaking and post-shaking event in case of Models 5 and 6 is apparent in comparison with Model 1 as shown in Fig. 5.19. The post-shaking settlement for both BT and FS footings is remarkably less in case of Model 6 compared to Models 1 and 5. However, BT exhibits comparatively large settlement for BT in case of Model 5 during the initial phase of Tokachi-Oki ground motion (i.e., 0-30 seconds). This might be associated with the localized higher permeability in the vicinity of BT, which steered the shear-induced deformation at the beginning of the shaking.
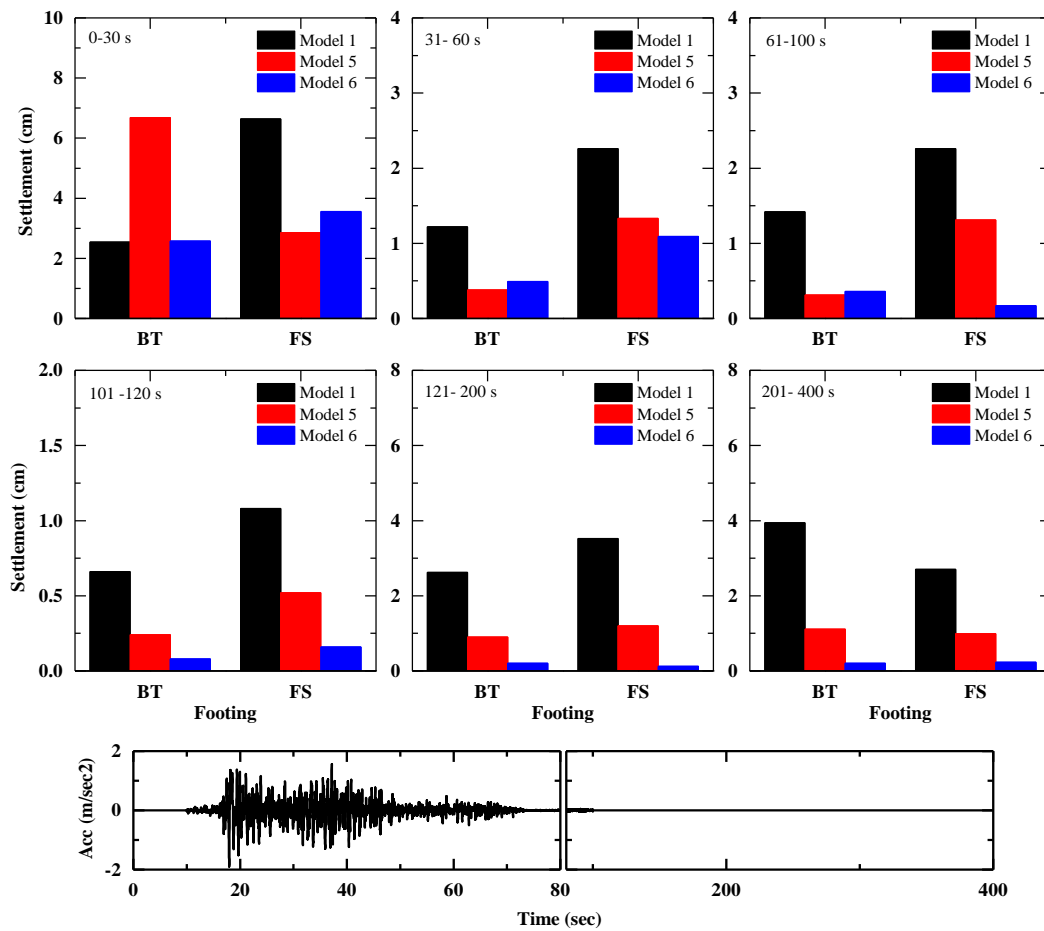
Fig. 5.19. Average settlement of BT and FS footings for different time periods during Tokachi-Oki ground motion

Fig. 5.20 shows the average settlement of BT and FS footing occurred within different time intervals during Tohoku ground motion. Surprisingly, the settlement occurred for both BT and FS before 100 seconds is adversely large in case of Model 6 in comparison with Models 1 and 5. However, BT and FS settlement until 100 seconds for Model 5, is more or less the same as the one observed for Model 1. The excessive settlement for both BT and FS before 100 seconds of shaking indicates sort of punching shear failure provided that the footing has a free vertical movement of the model ground, which could also be consolidated from Fig. 5.13, as the settlement of both BT and FS, is very steep in nature (in other words observed settlement is not progressive with time). In addition, it might be possible that at the beginning of the shaking, because of the jamming of the soil between the piles and footings, the piles took some load and the vertical stress in the soil under the structure was smaller than expected. This made the soil

under the structure more liquefiable, and further shaking released jammed of soil at the holes and allowed the footing to settle, resulting in the rather fast settlement in case of Model 6.
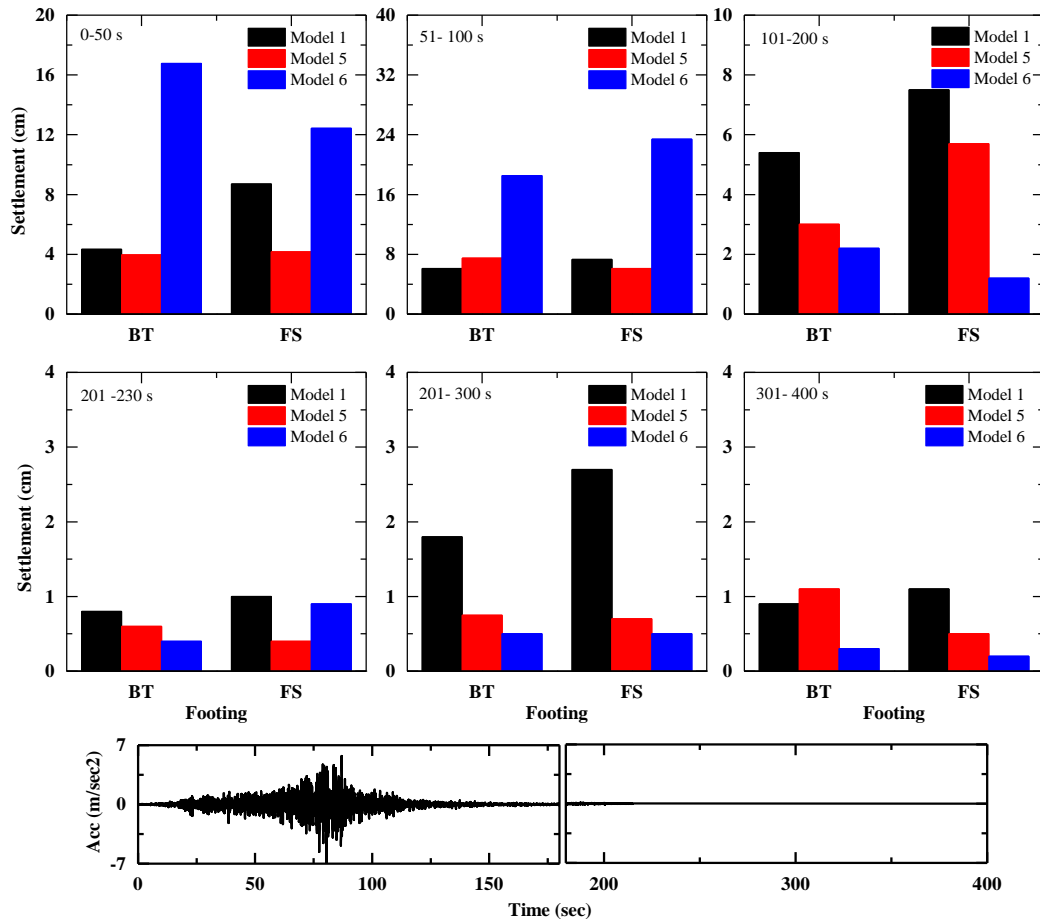
Fig. 5.20. Average settlement of BT and FS footings for different time periods during Tohoku ground motion

The trace of comparatively large increment in EPWP after even after shaking in case of Model 6 compared to Model 5 at P8, and P10 (see Fig. 5.12) also consolidate the fact as described above. The limitations of hybrid foundation (dominatingly for Model 6) to minimize the settlement of shallow foundation during Tohoku ground motion might be associated to many factors. High localized permeability because of presence of the gravel drainage might have adversely affected the settlement mechanism of shallow foundation during strong Tohoku ground motion. If the model ground experienced the complete liquefied state (model ground softening to be specific) during shaking, the accumulation of volumetric strains might increase to manifold because of simultaneously shear-induced deformation and post-liquefaction

reconsolidation caused by localized higher permeability.

5.3 Summary

The performance of induced partial saturation under a strong ground motion (Tohoku earthquake) is examined. Centrifuge test results under Tohoku earthquake are discussed in comparison with the respective test results under Tokachi-Oki ground motion. During Tohoku ground motion, the overall performance of partially saturated ground is diminished in comparison with the one witnessed during Tokachi-Oki ground motion. Tohoku earthquake is stronger than the Tokachi-Oki in terms of both peak acceleration and duration. It is observed that the availability of maximum potential volumetric compressibility because of induced air voids during WN1 is relatively more than that available during WN2. This corroborates the fact of air void dissolution/collapse during Tokachi-Oki and Tohoku ground motion. However, the available capacity of potential volume compressibility is found quite significant even after the strong Tohoku ground motion (corresponds to WN2) which signifies the novelty of induced partial saturation to increase the liquefaction resistance of the partially saturated ground. Besides, the partially saturated ground is found to minimize the footing settlement even under strong Tohoku ground motion. The presence of air voids within the ground increases the liquefaction resistance of the ground. However, air voids seem to have negligible effects at the deeper portion. The overall performance of induced partial saturation is quite satisfactory. However, much research is needed to develop the implementation guidelines and case history data for validation of site specific performance of induced partial saturation.

The performance of hybrid foundation seems to be diminished in terms of overall settlement of both BT and FS footings during Tohoku ground motion, whereas the evolution of EPWP within the model ground indicated otherwise. The hybrid foundation is a complex arrangement of the gravel drainage system and friction piles passing through the footing with a minimal clear spacing. The alteration in ground condition after Tokachi-Oki ground motion significantly affected the performance of hybrid foundation under Tohoku ground motion. The extent of softening of the ground due to liquefaction-induced mechanism during the seismic event could be captured qualitatively by the drop of site fundamental frequency. More substantial is the drop in the fundamental frequency, softer is the ground during shaking, which

is also related to the severity of the shaking. Settlement progression of the shallow foundation during co-shaking and post-shaking also associated with the liquefaction extent (model ground softening to be specific). Shallow foundation resting on liquefiable ground undergoes excessive settlement during Tohoku ground motion caused by co-shaking and post-shaking settlement mechanism.

Chapter 6. Reliability assessment of performance of a granular column

A hybrid foundation is developed to mitigate the liquefaction-induced effects on shallow foundations as discussed in Chapter 4. The proposed hybrid foundation is a combination of the gravel drainage system and friction piles having spiral blades devised under the footing as a hybrid mitigation technique against the liquefaction-induced effects. The efficacy of the hybrid foundation is investigated in the uniform deposit of liquefiable Toyoura sand (D_R ~50%). The gravel drainage system (D_R ~30%) used in the centrifuge experiment is an array of 5x5 granular columns (see Fig. 6.1). Design charts reported by Seed and Booker (1977) in their seminal work and the revised guidelines presented by Bouckovalas et al., (2009) are used to design the granular columns. Many parameters, e.g., replacement area, target excess pore water pressure ratio (r_u), earthquake intensity, reported case histories, and installation methodology of gravel drains, are considered while designing the granular columns. The index properties of Toyoura sand and granular column (silica no. 3) are tabulated in Table 4.1. There are a few parameters that need to be considered to ensure the reliability of the performance of the granular columns as an integral part of the developed hybrid foundation. For instance, the ground is prone to spatial nonuniformity, which was not considered in the centrifuge experiments. Besides, the granular columns only provided additional drainage to rapidly dissipate the excess pore water pressure (EPWP), and the contribution in the shear reinforcement is ignored in the centrifuge experiments. Moreover, the density of granular columns in the centrifuge experiments is nearly 30%, which is significantly less than the density of constructed granular columns at the site (usually in the range of 75- 85%). These site-specific parameters are essential to consider for a reliable engineering judgment on the performance of granular columns to mitigate the liquefaction-induced ground deformation.

6.1 Numerical model

Half of the single granular column (with $D_R = 80\%$) in the middle of the gravel drainage system

(due to symmetry) under the buffer tank (see Fig. 6.1) and associated model ground (effective drainage zone of granular column) in the above-mentioned centrifuge test is considered for the numerical simulations, as shown in Fig. 6.2. The reason for this idealization is that the modeling of the whole centrifuge model and gravel drainage system (see Fig. 6.1) is computationally expensive and not feasible for stochastic analyses as the reliability assessment requires thousands of analyses. Similar idealizations have been well-adopted by many researchers (Elgamal et al., 2009; Raymajhi et al., 2014; and Khosravifar et al., 2018). This approach does not account for the distinct stress distribution to the individual granular column (in the gravel drainage system) coming from the foundation-structure system during the dynamic event. Instead, the intent is to explore the reliability at a single granular column to get an insight into the overall performance of the whole gravel drainage system.
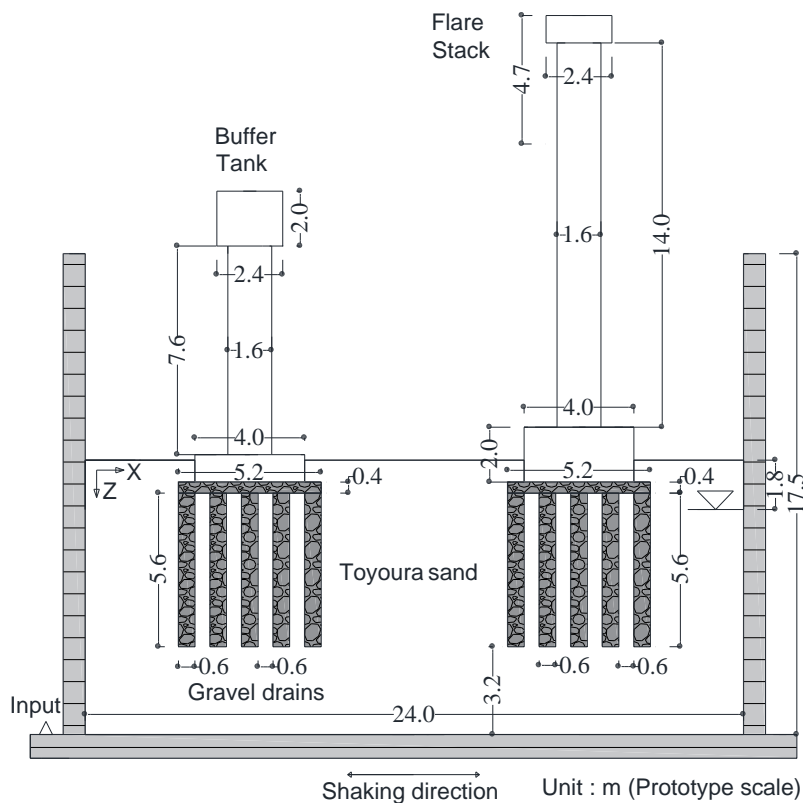
Fig. 6.1. Centrifuge model configuration in the prototype scale
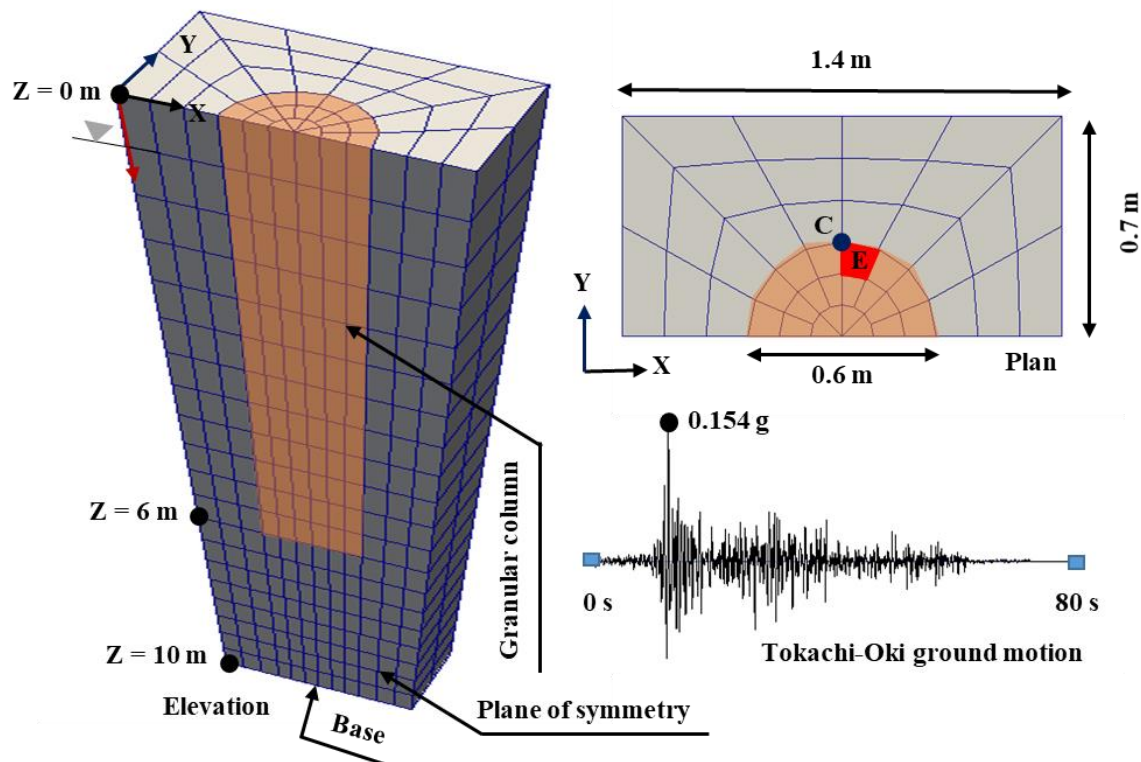
Fig. 6.2. Three-dimensional (3D) numerical model

Numerical simulations are carried with Rayleigh damping of 1% at a frequency of 1 Hz corresponding to the first-mode of a typical nonlinear ground response is used in the analyses (Stewart, 2008). The ground is modeled using brick u-p (8-node brickUP) elements. The load from the foundation-structure system is modeled as surface pressure for simplicity. The load from the foundation-structure system is modeled as surface pressure for simplicity. The effects of the superstructure inertia are ignored in this study. The bottom nodes of the ground are kept fixed in all the degrees of freedom. Tokachi-Oki ground motion (NS component of recorded shaking at the Hachinohe Port in 1968, see Fig. 6.2) is imposed on the bottom nodes of the ground during the dynamic analyses using the multiple support excitation technique in OpenSees. All the nodes on the side boundary with the same elevation are tied to move together (in X and Y direction) using equalDOF command in OpenSees. The vertical movement of side boundary nodes are kept free. The nonuniformity of the liquefiable ground is considered in the presented study. Based on the random realization of the nonuniformity of the ground, the relative density of the elements would fall into a wide range (D_R = 30 – 75%, discussed in Section 6.3). The dynamic behavior of the liquefiable element significantly depends on the

relative density and its corresponding calibrated parameters. In this case, tie the vertical movement of side nodes with periodic boundary (as adopted by Law and Lam, 2001; Elgamal et al., 2009; and Rayamajhi et al., 2014, for a uniform ground) would enforce the side boundary elements to have same settlement which is not reasonable for the nonuniform ground even though the extent of the model in the X and Y directions (see Fig. 6.2) are small compared to the size of the granular column. All the nodes above the water table are assigned zero pore water pressure. The nodes of the planes of Y= 0 and 0.7 m (see Fig. 6.2) are kept fixed against the out-of-plane displacement.

PDMY02 soil constitutive model is used to model the ground. The PDMY02 Model is an elastoplastic soil-liquefaction constitutive model originally developed to simulate the cyclic liquefaction response and the associated accumulation of cyclic shear deformation in clean sand and silt (Yang et al., 2003). Within a stress–space plasticity framework, PDMY02 Model employs a new flow rule and strain–space parameters to simulate the cyclic development and evolution of plastic shear strain. PDMY02 does not include a critical state soil mechanics framework.

The parameters of the PDMY02 Model are calibrated to achieve the single-amplitude shear strain of 3% in cyclic undrained simple shear loading with zero initial static shear stress ratio on a horizontal plane at a single element level. Laboratory test results from Chiaro et al. (2012) are considered as the dynamic behavior of saturated Toyoura sand with a relative density of 50% at a single element level for the calibration purpose. Fig. 6.3(a) shows a typical response of calibrated PDMY02 Model for cyclic stress ratio (CSR) = 0.171, D_R = 50%, and σ'_{vc} = 100 kPa in cyclic undrained simple shear loading with zero initial static shear stress ratio on a horizontal plane. The PDMY02 Model exhibits the ability of shear strain accumulation, commonly referred to as cyclic mobility, which is evident from the stress-strain behavior. The stress path is shown in Fig. 6.3(b). The vertical effective stress ratio drops down to nearly zero within 15 cycles and triggered large shear strains afterward. Numerically simulated cyclic response at the single element level is obtained after calibrating the parameters of the PDMY02 Model to achieve a similar response as observed in the experiment in terms of cyclic mobility, initial shear modulus, and the accumulation rate of shear strain. Fig. 6.3(c) shows the shear strain accumulation with the drop in vertical effective stress ratio. Fig. 6.3(d) shows the CSR curves corresponding to single-amplitude shear strains of 3% with zero initial static shear stress ratio. The calibrated values of the PDMY02 Model for Toyoura sand (D_R ~50%) and granular

column ($D_R \sim 80\%$) are shown in Table 6.1.
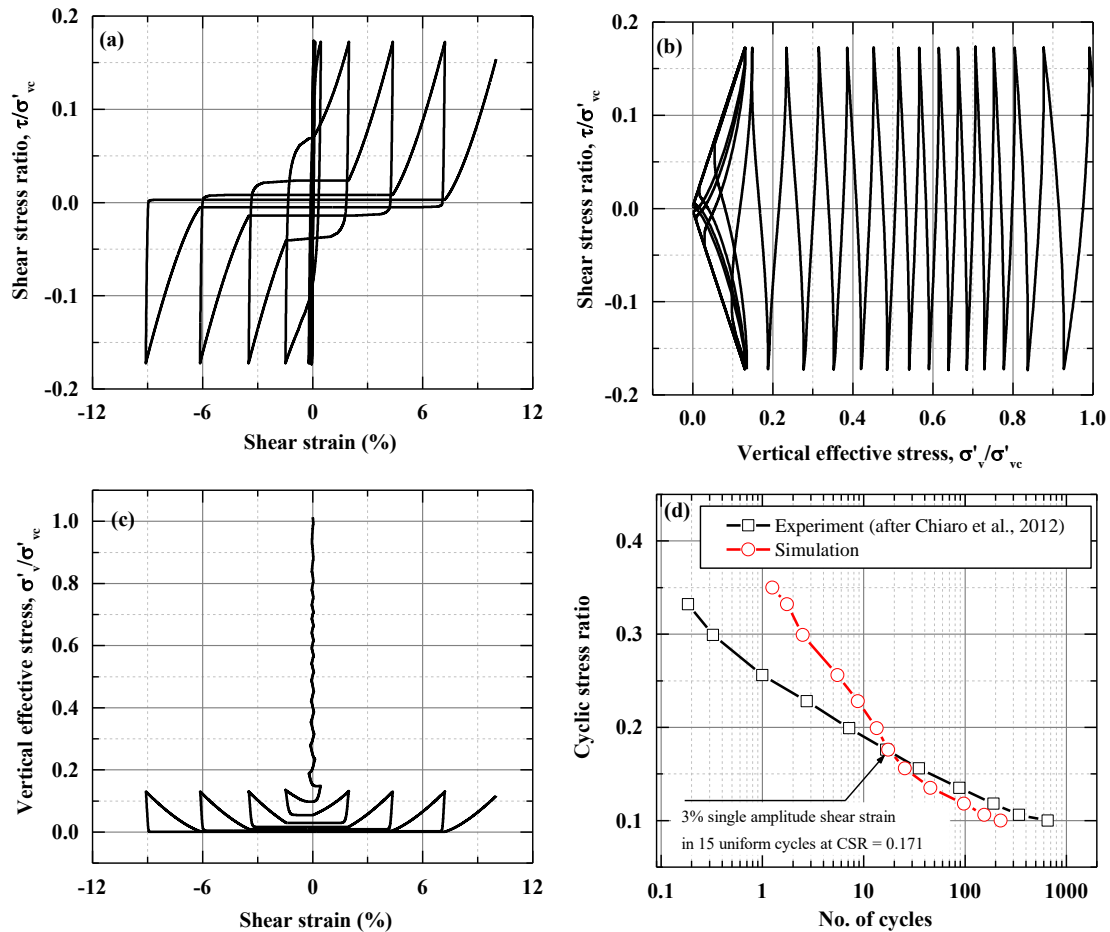
Fig. 6.3.   The response of the calibrated PDMY02 Model at the element level

Table 6.1.   Calibrated parameters for Toyoura sand and granular column

Material/Pars*ameter	ρ (ton/m^3)	G_{max} (kPa)	B (kPa)	φ	PT_{ang}	C1	C3	D1	D3
Toyoura sand (D_R = 50%)	1.94	3.54E4	7.50E4	33.5	25.5	0.07	0.20	0.06	0.20
Granular column (D_R = 80%)**	2.14	10.4E4	26.0E4	48	30	0.006	0.0	0.42	0.0

*Remaining parameters (total number of parameters are 22) received default values as reported by Khosravifar et al. (2018)

**The parameters for the granular column are selected per Elgamal et al. 2009, Raymajhi et al. 2016, and Khosravifar et al. (2018).

6.2 Deterministic analyses

6.2.1 Ground deformation

The deterministic analysis is carried out (Toyoura sand with D_R ~50%, the granular column with D_R ~80%) before performing the series of stochastic analyses to investigate the dynamic behavior of a liquefiable ground treated with equally-spaced granular columns. The simulated time histories of average settlement of the top surface of the grounds with and without granular column are shown in Fig. 6.4.
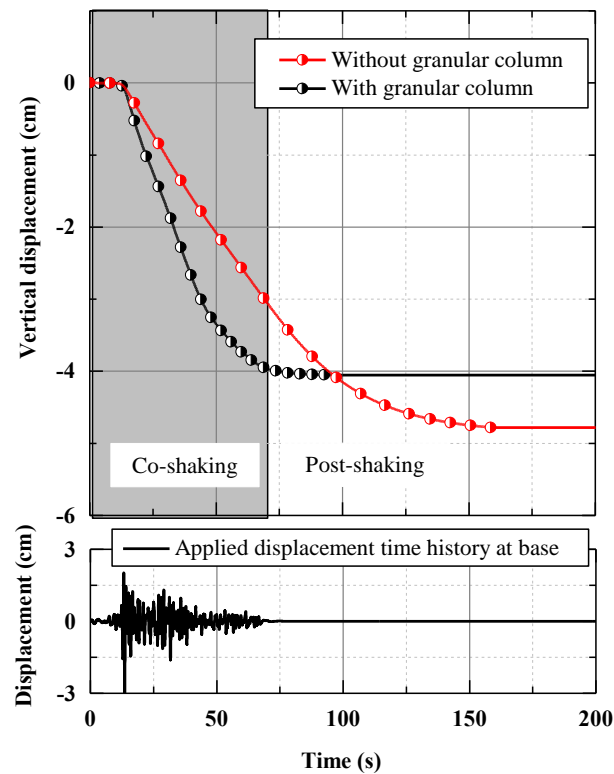
Fig. 6.4. Average settlement of the top surface of the ground

The settlement time histories are divided into co-shaking and post-shaking phases. It is evident that the rate of settlement in the co-shaking phase (until t = 50 s) is significantly large in the case of the ground with the granular column in comparison with the ground without a granular column. The large permeability of the granular column seems to adversely affect the settlement evolution during the co-shaking phase. The settlement time histories also indicate that the relatively large stiffness of the granular column (with respect to the ground) does not

have any contribution in the restriction of the average vertical settlement of the top surface of the ground. This was also confirmed with the simulated settlement time histories of the ground with granular columns of density D_R ~30 and 80% as there was not any considerable change in the simulated settlement response.

The effectiveness of the granular column is evident in restricting the post-shaking average settlement of the top surface of the ground. Similar trends were observed in the centrifuge experiments as reported in Chapter 4. However, the numerically simulated settlement is significantly less than the observed settlement (in centrifuge experiments) in the post-shaking phase for both the grounds with and without granular column, while that in the co-shaking is comparable to the observed ones. It is to be noted that the laminar boundary conditions in the numerical model ignore the settlement contribution due to three-dimensional lateral spreading in the centrifuge test. This idealization is also responsible for the overall less settlement in the case of numerical simulations. Several researchers have made similar observations, e.g., Taibet et al. (2007), Dashti and Bray (2013), Karimi and Dashti (2015), and Kumar et al. (2020). The numerical models typically exhibit limitations in capturing the settlement caused by partial drainage and reconsolidation specifically the post-shaking phase because of the characteristics of their constitutive formulations, as reported by Shahir et al. (2012), Karimi and Dashti (2016), Boulanger and Ziotopoulou (2017), and Adamidis and Madabhushi (2019).

Fig. 6.5 shows the horizontal displacement of the top surface of the grounds with and without the granular column. The peaks of applied ground motion triggered the large horizontal displacement at the beginning of the shaking (t = 12 - 16 s). The ground without the granular column experienced the mobilization of its shear strength soon after the maximum horizontal displacement and started to exhibit the traces of cyclic mobility (accumulation of horizontal displacement in one direction) after t = 28 s. However, the ground with granular column did not show such a tendency, and the residual horizontal displacement is marginal in comparison with the ground without a granular column.
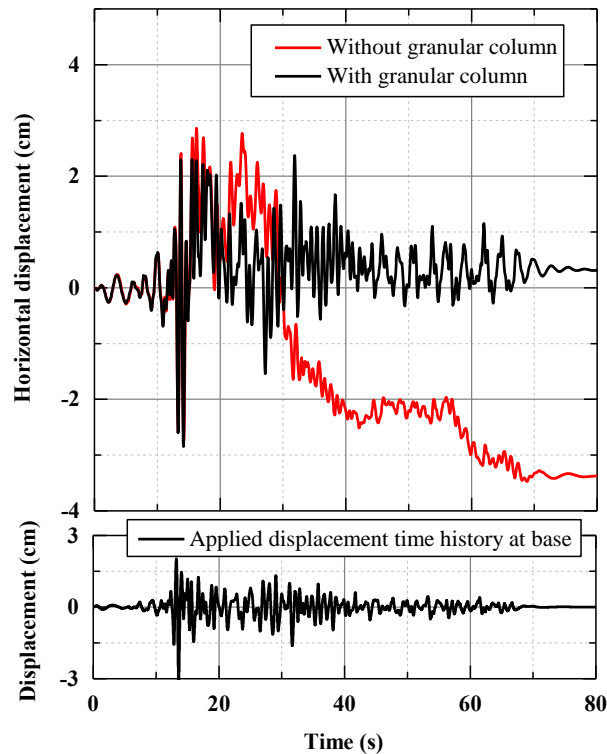
Fig. 6.5.   The horizontal displacement of the top surface of the ground

6.2.2   *Evolution of excess pore water pressure*

The evolution of EPWP plays a vital role in the manifestation of liquefaction during the dynamic event. Fig. 6.6 shows the EPWP generation and dissipation trends at different depths along a selected point C (see Fig. 6.2) for the grounds with and without a granular column. The soil at certain depth undergoes liquefaction state if the r_u, which is the ratio of EPWP and the initial vertical effective stress at respective depth, reaches one. During the early phase of shaking, the generation rate of EPWP is typical for both the grounds. However, the ground without granular column shows a significantly larger magnitude of maximum EPWP, even approaching $r_u = 1$ line (liquefaction state) at depths Z = 5, 8, and 10 m. The ground with granular column exhibits significantly faster dissipation of EPWP after t = 20 s in comparison with the ground without the granular column. The observed trends signify that the presence of a granular column is able to restrict the evolution of EPWP to minimize the extent of the liquefaction in the ground.
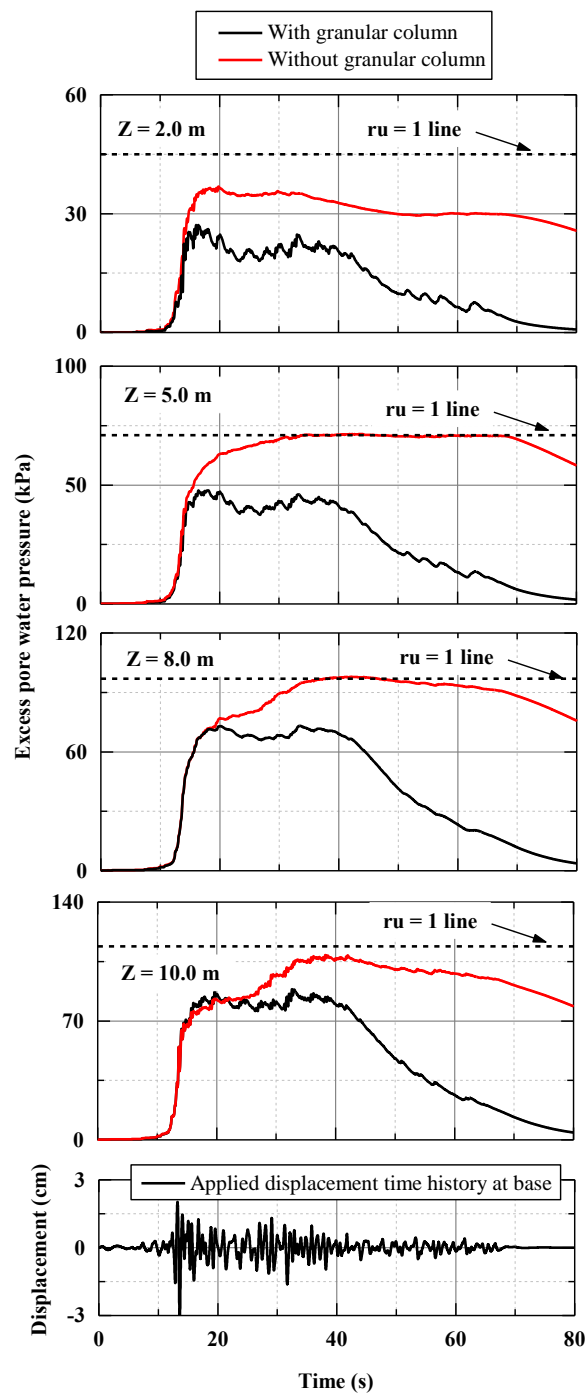
Fig. 6.6. Evolution of excess pore water pressure along point C (see Fig. 6.2) at different depths for grounds with and without granular column
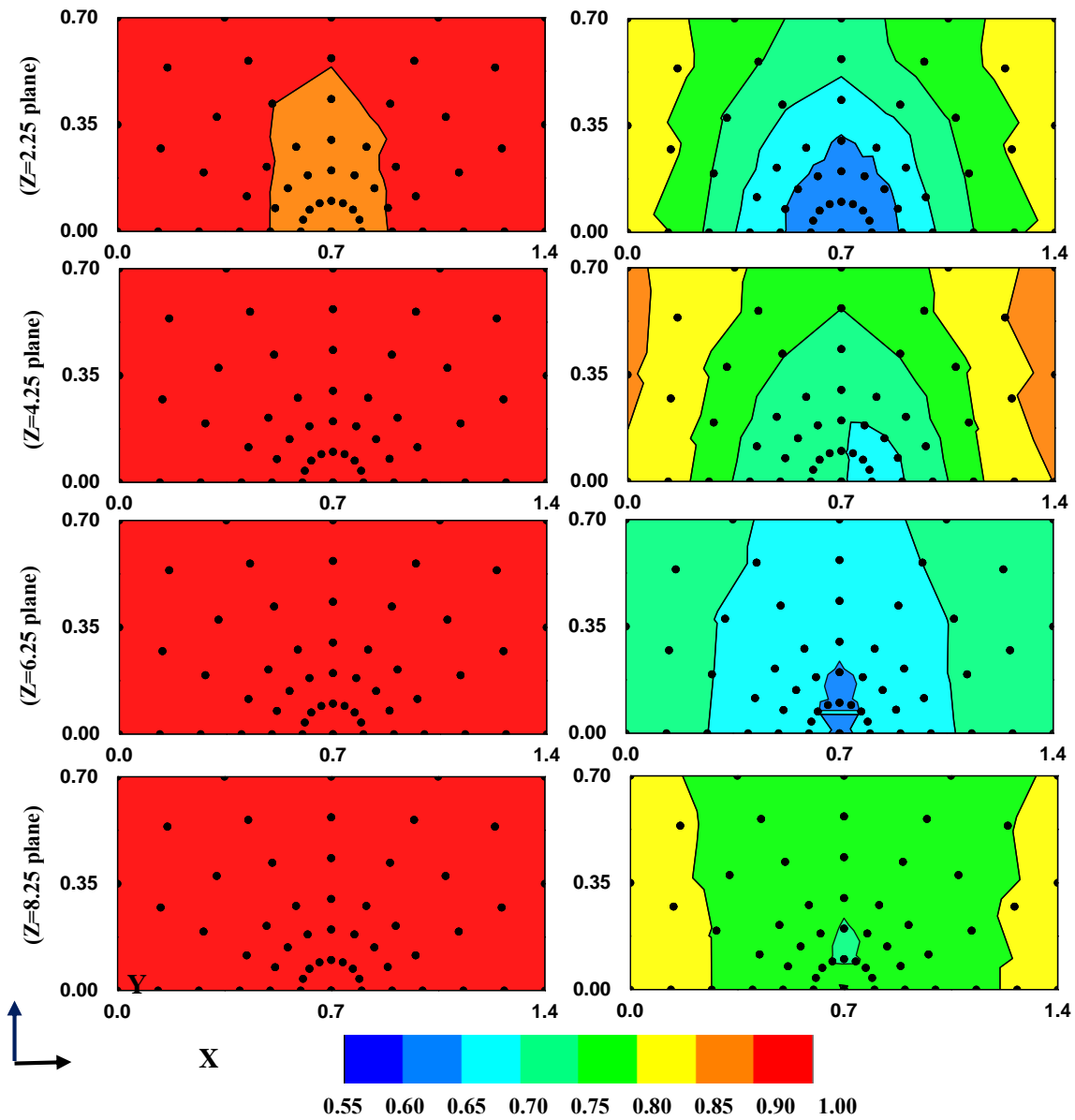
Fig. 6.7. Contours of maximum r_u at different depths (planes Z = 0.25, 2.25, 4.25, 6.25, and 8.25 m) for (a) ground without granular column and (b) ground with granular column

Contours of maximum r_u for the grounds with and without granular column at different depths are shown in Fig. 6.7. Four different planes are selected at different depths Z = 2.25, 4.25, 6.25 and 8.25 m (depths are selected below the below water table or drainage boundary to examine the apparent effects of granular column). Fig. 6.7(a) depicts that the ground without granular column undergoes liquefaction as the values of r_u is in the range of 0.90 – 1.0 for all the planes at depths Z = 2.25, 4.25, 6.25, and 8.25 m (however, slightly lower values of r_u in the

range of 0.85 – 0.90 are observed for a few elements at depth Z = 2.25 m). The presence of granular column is found to restrict the evolution of EPWP remarkably as the r_u values are significantly lower for the ground with the granular column in caparison with the ground without granular column as depicted in Fig. 6.7(b). The best performance of the granular column appeared to be just below the base of the granular column (at depth Z = 6.25 m, noted that the depth of the granular column is 6 m). The base of the granular column acts as a drainage boundary for the pore fluid during the earthquake. The strong hydraulic gradients steer the pore fluid toward the granular column, which facilitates in the significant dissipation of EPWP (Kumar et al. 2019b). This also corroborates the observation that the granular column is able to restrict the values of r_u in the range of 0.70 – 0.85 for a plane at a depth Z = 8.25 m, which is significantly deeper from the base of the granular column.

6.2.3 Shear reinforcement

The deformed shapes (10 times magnified) after the shaking and the distribution of r_u at t = 16 s for the grounds with and without granular column are shown in Fig. 6.8. It is evident from Fig. 6.8(a) that the ground without the granular column undergoes significant deformation (settlement and horizontal displacement). The ground exhibited mobilization of shear strength for depths Z = 4 - 6 m (element behavior at Z =5 m is shown in Fig. 6.9(a)). The ground also exhibited the state of liquefaction (r_u ~ 1, from depths Z = 3 – 9 m, as shown in Fig. 6.8(b)). The liquefaction in the ground resulted in the mobilization of shear strength during the shaking, which lead to the excessive deformation of the ground. The presence of granular column increased the overall stiffness of the ground (discussed later with Figs. 6.9 and 6.10) and minimized the overall liquefaction extent of the ground (Figs. 6.7 and 6.8(b)), which restricted the deformation of the ground.

Stress-strain curves for elements of array E, at Z = 5 and 10 m (see Fig. 6.2) for the grounds with and without granular column are shown in Fig. 6.9. It is evident from Fig. 6.9(a) that the element of the ground without the granular column undergoes considerable shear strain in comparison with the ground with the granular column. This also corroborates the observation made earlier that the ground without granular column exhibited mobilization of excessive shear strength for depths Z = 4 - 6 m (as discussed with Fig. 6.8(a)). The stress-strain curves for the element at Z = 10 m (Fig. 6.9(b)) exhibits the trace of relatively large stiffness degradation

during the shaking for the ground without the granular column in comparison with the ground with the granular column. This implies that the presence of a granular column increases the overall stiffness of the ground. Besides, the granular column helped to minimize the liquefaction extent (Figs. 6.7 and 6.8(b)), which also resulted in stiffer behavior of the ground with the granular column. The general notion that the presence of a granular column increases the overall stiffness of the ground (Baez 1995) is further examined with Figs. 6.10 and 6.11. The induced cyclic stress ratio during the shaking is proportional to the shear stress reduction coefficient per the simplified procedure of Seed and Idriss (1971), as shown in equation 6.1.
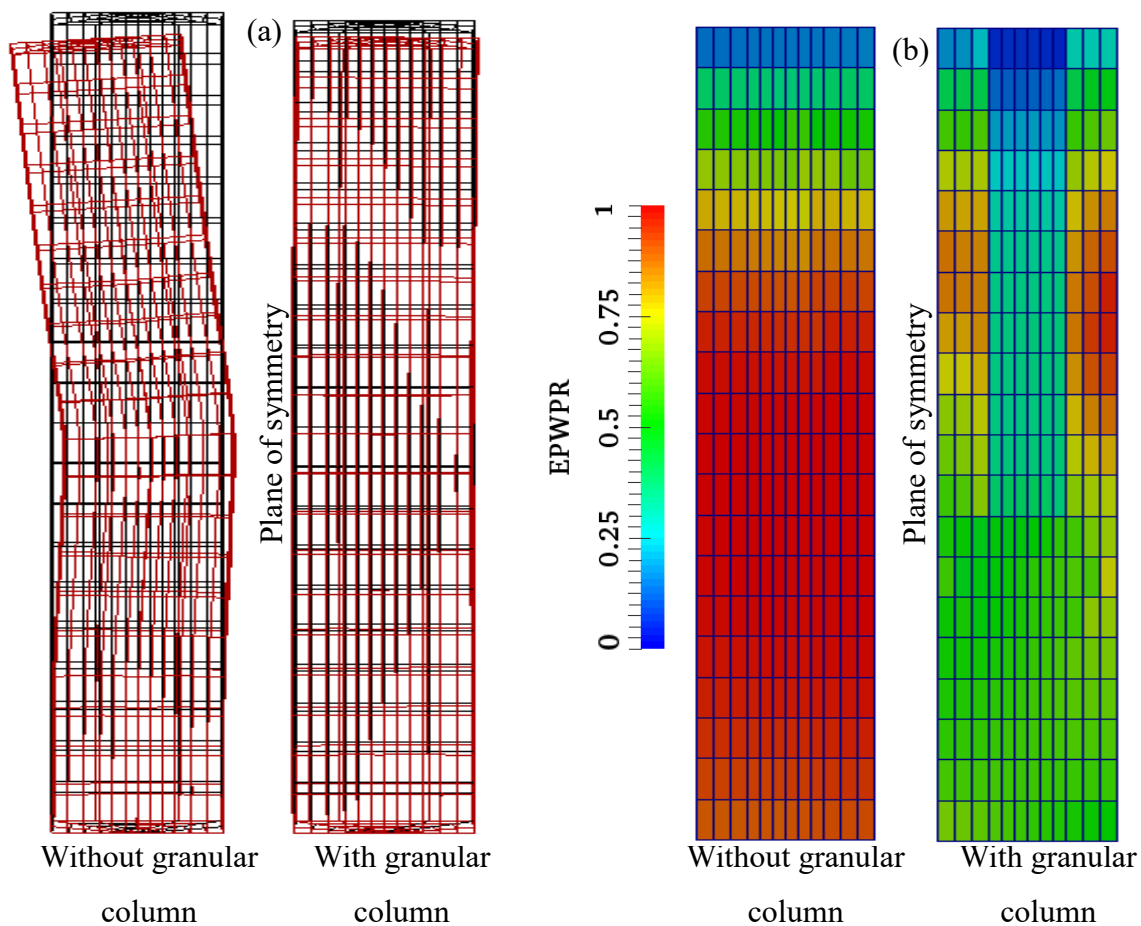
Fig. 6.8. Ground response: (a) deformed shape (10 times magnified) after the shaking and (b) distribution of r_u at t = 16 s
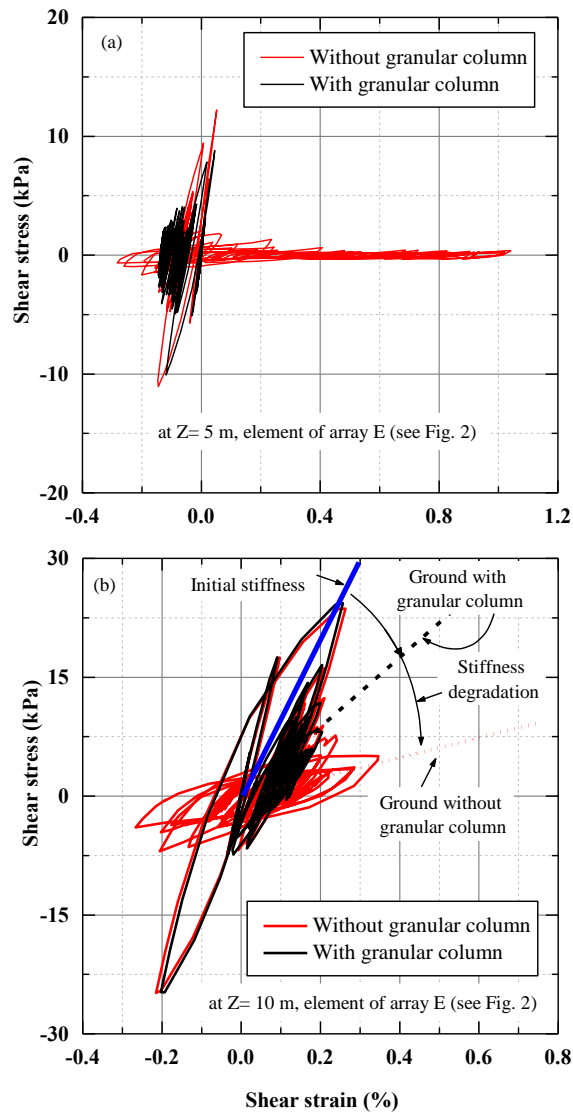
Fig. 6.9.   Typical stress-strain behavior for elements along E (see Fig. 6.2): (a) at depth Z = 5 m and (b) at depth Z = 10 m

$$\text{CSR} = \frac{\tau_s}{\sigma'_v} = 0.65 \left(\frac{a_{max}}{g}\right)\left(\frac{\sigma_v}{\sigma'_v}\right) \text{rd} \qquad (6.1)$$

Where, CSR = cyclic stress ratio; τ_s = cyclic shear stress; σ'_v and σ_v = effective and total vertical stress at a depth of interest, respectively; a_{max} = peak horizontal acceleration; rd = shear stress reduction coefficient. Larger is the stress reduction coefficient, larger the induced cyclic stress ratio during the shaking. The effect of the granular column on shear stress distribution within the ground is estimated using R_{rd}, which is defined in equation 6.2.

$$R_{rd} = \frac{rd_{wg}}{rd_{ng}} \qquad (6.2)$$

Where, rd_{wg} and rd_{ng} = shear stress reduction coefficient for the grounds with and without granular column, respectively. The value of R_{rd} can provide an insight into the shear reinforcement in the ground due to the granular column. For instance, the value of R_{rd} less than one, equal to one, and more than one implies that the ground with granular column experience proportionally smaller, equal, and larger shear stress, respectively, in comparison with the ground without the granular column.

Fig. 6.10 shows the contours of R_{rd} at different depths (at the middle of the elements for planes Z = 0.25, 2.25, 4.25, 6.25 and 8.25 m) of the ground. The values of R_{rd} inside the zone of the granular column (see Fig. 6.2) is more than or equal to one for planes Z = 0.25, 2.25, and 4.25 m as expected. This is associated with the fact that the granular column attracts larger shear stress due to its stiffer characteristics. The substantial spatial variation in the values of R_{rd} is evident at the top surface of the ground (plane Z = 0.25 m), which is associated with the deformation pattern. Besides, the load from the foundation-structure system is modeled as surface pressure (applied at the top surface of the ground), which also resulted in the attraction of significant shear stress due to the apparent inertial interaction during the dynamic loading. The values of R_{rd} for planes Z = 2.25 and 4.25 m are significantly less than one in the ground away from the zone of the granular column, which shows the substantial contribution in the shear reinforcement due to the presence of the granular column.

A relatively uniform distribution of R_{rd} is observed for the planes Z = 6.25 and 8.25 m, and the values of R_{rd} are less than one. It is to be noted that the granular column is up to 6 m of depth (see Fig. 6.2); however, the presence of the granular column seems to reduce the shear stress in the whole ground. The presence of a granular column reduces the induced shear stress in the ground, as shown in Fig. 6.10. However, the magnitude of shear strain in the ground may not adhere to the shear reinforcement during the shaking. Fig. 6.11 shows the contours of the ratio of shear strain (γ) at different depths (at the middle of the elements for planes Z = 0.25, 2.25, 4.25, 6.25 and 8.25 m) of the ground. The value of γ less than one signifies the contribution of shear reinforcement in reducing the shear strain in the ground due to the granular column. The strong spatial variation in the values of γ (values being close to one) is evident for the planes at depth Z = 0.25 and 2.25 m. This incompatibility in shear strain reduction is attributed to the complex deformation mechanism as reported by several researchers (Goughnour and Pestana, 1998; Green et al., 2008; Olgun and Martin, 2008; and Raymajhi et al., 2014) and should be

taken into account while designing the gravel drainage system.
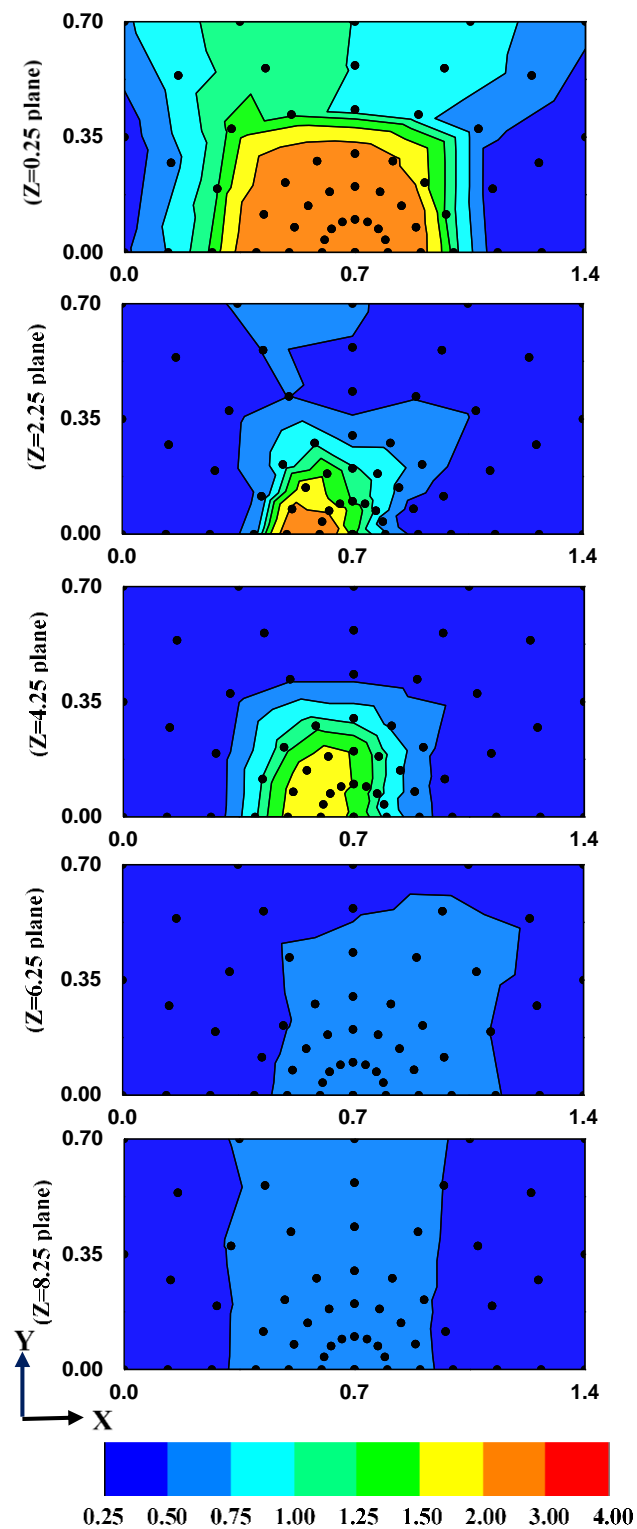
Fig. 6.10. Contours of the ratio of maximum shear stress reduction coefficient at different depths (planes Z = 0.25, 2.25, 4.25, 6.25, and 8.25 m) of the ground
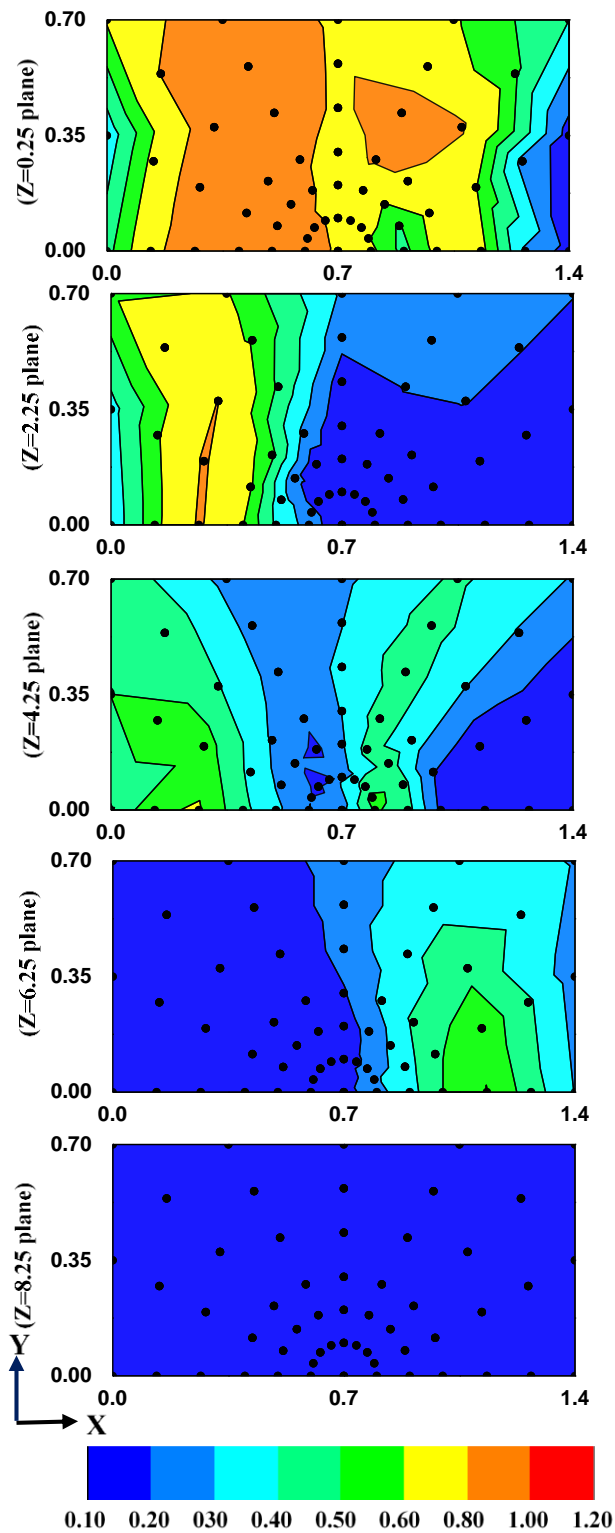
Fig. 6.11. Contours of the ratio of maximum shear strain at different depths (planes Z = 0.25, 2.25, 4.25, 6.25, and 8.25 m) of the ground

6.3 Stochastic analyses

The modeling of inherent soil variability can be achieved utilizing the advanced nonlinear finite element analyses and well-calibrated sophisticated elasto-plastic soil constitutive models. The nonuniformity of the ground is mapped using the overburden and energy-corrected, equivalent clean sand, SPT $(N1)_{60cs}$ values. For a given $(N1)_{60cs}$ value, the relative density (D_R) is calculated per equation 6.3 (Boulanger and Ziotopoulou, 2017).

$$D_R = \sqrt{\frac{(N1)_{60cs}}{46}} \qquad (6.3)$$

A Gaussian correlation function is used, and the random field is generated with Karhunen Loeve (KL) decomposition method (Constantine and Wang, 2012, 2020). The discretized mesh (Fig. 6.2) is implemented in the matrix form of size n by d; where n is the number of nodes and d is the dimension of the random field. The coefficient of variation (COV = 40%) and scale of fluctuation ($\theta x = 5.0$ m and $\theta z = 0.5$ m) are considered to model the nonuniformity of the ground according to Phoon and Kulhawy (1999) and Montgomery and Boulanger (2016). The nonuniformity of the ground is modeled with a mean $(N1)_{60cs} = 12$ ($D_R \sim 50\%$), as shown in Fig. 6.12. A series of three-dimensional stochastic dynamic analyses are performed considering the nonuniformity of the ground using anisotropic, spatially correlated Gaussian random fields of $(N1)_{60cs}$ values. The parameters of PDMY02 are calibrated for a wide range of relative densities corresponding to $(N1)_{60cs}$ of 5 ($D_R \sim 32\%$) to $(N1)_{60cs}$ of 26 ($D_R \sim 75\%$). The parameters of the PDMY02 Model are calibrated to achieve the single-amplitude shear strain of 3% in cyclic undrained simple shear loading with zero initial static shear stress ratio on a horizontal plane at a single element level as described earlier. The target strength (CRR for 3% single-amplitude shear strain in 15 uniform cycles) for different relative densities are estimated using the SPT-based correlation as suggested by Boulanger and Idriss (2014). Numerically simulated CSR curves for relative densities of $D_R = 30$ and 75% are compared with the CSR curves obtained in the experiment, as shown in Fig. 6.13 (CSR curves for $D_R = 50\%$ is shown in Fig. 6.3(d)). Figs. 6.3(d) and 6.13 exhibit that the calibrated parameters reasonably approximate the dynamic behavior of Toyoura sand. The calibrated parameters for 17 different individual relative densities ranging from $D_R = 30 – 75\%$ are tabulated in Table 6.2. For intermediate relative densities, linear interpolation is used to get the calibrated parameters.
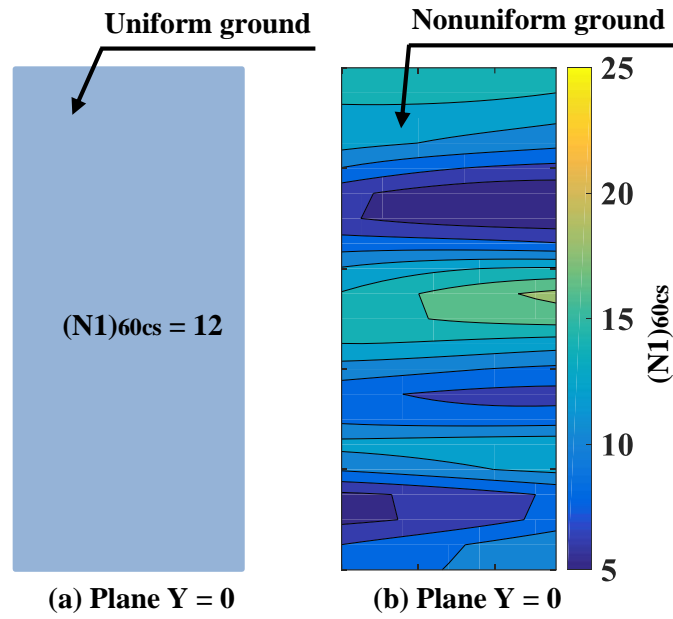
(a) Plane Y = 0   **(b) Plane Y = 0**

Fig. 6.12. A typical scenario of the ground condition at Plane Y= 0 (see Fig. 2): (a) uniform ground and (b) nonuniform ground
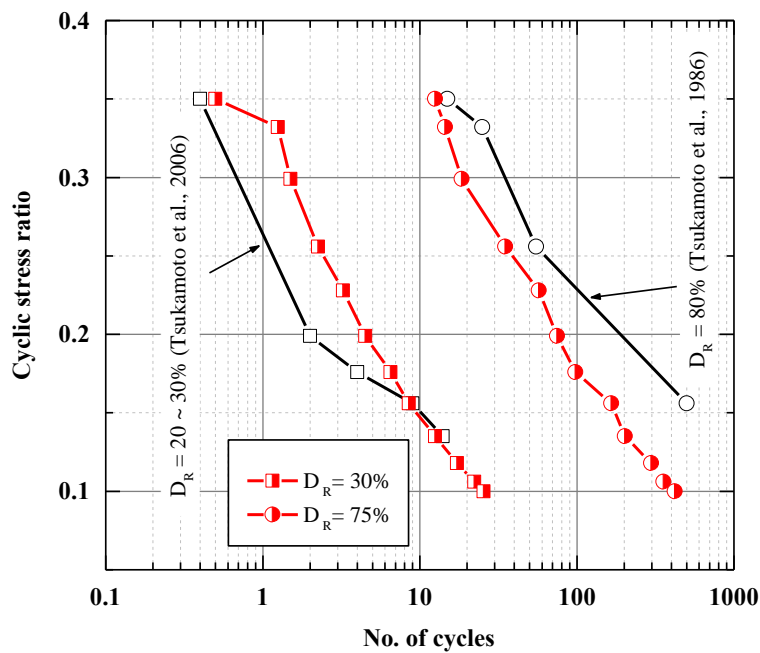
Fig. 6.13. The response of the calibrated PDMY02 Model at element level for loose (D_R = 30%) and dense sand (D_R = 75%)

Table 6.2. Calibrated parameters for Toyoura sand with different relative densities (D_R = 30 – 75%)

D_R (%)	G_{max} (kPa)	B (kPa)	φ	PT_{ang}	C3	D1	D3
30	2.5E4	5.30E4	31.0	31.0	0.52	0.00	0.00
33	2.6E4	5.51E4	31.4	29.0	0.48	0.00	0.00
36	2.7E4	5.72E4	31.8	27.0	0.40	0.01	0.10
39	2.8E4	5.93E4	32.0	26.0	0.30	0.04	0.10
42	2.9E4	6.14E4	32.2	25.9	0.27	0.06	0.25
45	3.0E4	6.36E4	32.5	25.8	0.20	0.06	0.20
48	3.1E4	6.57E4	32.9	25.7	0.20	0.06	0.20
50	3.5E4	7.50E4	33.5	25.5	0.20	0.06	0.20
52	3.7E4	7.73E4	33.8	25.6	0.15	0.06	0.15
55	3.8E4	8.05E4	34.1	25.7	0.10	0.09	0.10
58	4.0E4	8.47E4	34.5	25.8	0.06	0.09	0.10
61	4.5E4	9.53E4	35.0	26.0	0.06	0.09	0.10
64	5.2E4	1.09E5	35.3	26.0	0.06	0.10	0.10
67	5.9E4	1.24E5	35.6	26.0	0.04	0.13	0.10
71	6.3E4	1.32E5	35.7	26.0	0.04	0.14	0.00
73	7.1E4	1.49E5	35.9	26.0	0.00	0.17	0.00
75	8.0E4	1.68E5	36.0	26.0	0.00	0.20	0.00

Note: C1 is 0.07 for all D_R. The remaining parameters (total number of parameters are 22) received default values as reported by Khosravifar et al. (2018)

The granular column and associated ground (Toyoura Sand) is assigned a uniform permeability value of 0.0066 and 0.0002 m/s, respectively. The assigned uniform properties for the granular column is corresponding to $(N1)_{60cs}$ of 30 (D_R ~ 80%), per Raymajhi et al. (2016) and Khosravifar et al. (2018). The random field of $(N1)_{60cs}$ values with calibrated parameters of the PDMY02 Model are implemented into the OpenSees numerical model with the help of Matlab code.

Fig. 6.14 shows the typical variation of the mean and standard deviation of the average settlement and horizontal displacement of the top surface (Z = 0 plane, see Fig. 6.2) of the ground with the granular column. The mean and standard deviation become stable within fifty realizations, and hence, a reliable statistical interpretation of the stochastic data can be obtained from the series of nonlinear dynamic numerical simulations. It should be noted that the larger

the number of realizations, the better the reliability of the statistical interpretation. However, the numerical computational expense should be taken into account when selecting the total number of realizations without compromising with the stability of the mean and standard deviation of the primary stochastic outcomes (e.g., the average settlement and horizontal displacement of the top surface of the ground in this chapter).
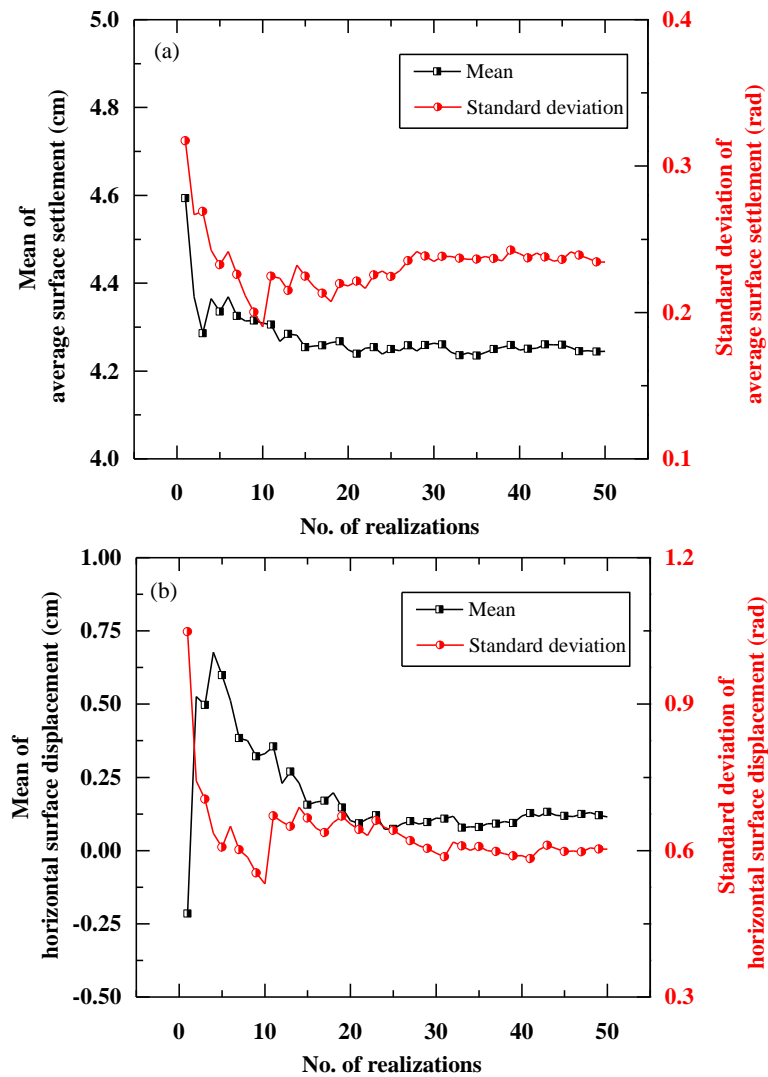
Fig. 6.14. Convergence check for sufficient number of stochastic realizations

6.3.1 *Stochastic distribution of ground deformation*

The results of three–dimensional stochastic analyses are presented and compared with the deterministic analysis results. Fig. 6.15 illustrates the stochastic distribution of the average settlement and horizontal displacement of the top surface of the ground (Z = 0 plane, see Fig.

6.2) for the grounds with and without a granular column. Fig. 6.15(a) depicts that the mean (μ) and the standard deviation (σ) of the average surface settlement is 4.31 cm and 0.23 cm, respectively, for the ground with the granular column. It is observed that the mean of stochastic average surface settlement is significantly larger than the respective deterministic value. Whereas, the mean (μ) and the standard deviation (σ) of the average surface settlement is 4.80 cm and 0.10 cm, respectively, and the mean value is comparable to the deterministic value for the ground without the granular column. A relatively wider stochastic distribution and considerable standard deviation in the average surface settlement is evident in the case of the ground with the granular column in comparison with the ground without a granular column. This emphasizes that the presence of a granular column may adversely affect the uncertainty in the prediction of the average surface settlement due to the inherent ground nonuniformity (further discussed with Fig. 6.16).

Fig. 6.15. Stochastic distribution of model ground deformation for the grounds with and without granular column: (a) average surface settlement and (b) surface horizontal displacement

Fig. 6.15(b) depicts that the mean (μ) and the standard deviation (σ) of the horizontal surface displacement is 0.31 cm (distribution in the range of -1.0 cm to 1.5 cm) and 0.60 cm, respectively, for the ground with the granular column. Whereas, the mean (μ) and the standard deviation (σ) of t surface horizontal displacement is -3.17 cm (distribution in the range of -6.0 cm to -1.0 cm) and 1.34 cm, respectively, for the ground without granular column. The mean of the stochastic distribution is comparable with the deterministic values for both the cases of grounds with and without the granular column. However, a relatively wider stochastic distribution and considerable standard deviation in the horizontal surface displacement is evident in the case of the ground without the granular column in comparison with the ground with the granular column. This emphasizes that the presence of a granular column may favorably affect the uncertainty in the prediction of horizontal surface displacement (further discussed with Fig. 6.16). The reason for this is the shear reinforcement of the ground due to the stiffness of the granular column, which is the governing factor for the residual amount of horizontal surface displacement, as discussed earlier. Besides, the granular column is considered with uniform properties, which facilitated relatively less uncertainty in the prediction of surface horizontal displacement in the case of the ground with the granular column in comparison with the ground without a granular column.

The probability of deviation of the stochastic average settlement and horizontal displacement of the top surface of the ground from their deterministic values are evaluated and presented in Fig. 6.16 for the grounds with and without the granular column. The deviations of the average settlement and horizontal displacement of the top surface of the ground are considered on the positive side (more than the deterministic value) and the negative side (less than the deterministic value).

Fig. 6.16(a) shows that total probabilities of the stochastic average surface settlement being deviated on the negative side from the deterministic value are 13.07 and 40.03%, respectively, and on the positive side from the deterministic value are 86.45 and 56.65%, respectively, for the grounds with and without granular column. The maximum deviation of the average surface settlement on the negative side is 0.20 cm (with a 2.32% probability of occurrence) and 0.29 cm (with a 0.09% probability of occurrence), respectively, for the grounds with and without granular column. The maximum deviation of the average surface settlement on the positive side is 0.62 cm (with a 5.97% probability of occurrence) and 0.19 cm (with a 4.43% probability of

occurrence), respectively, for the grounds with and without granular column. A relatively larger deviation from the deterministic value associated with a significant probability of occurrence in case of the ground with granular column signifies that the presence of granular column adversely affects the uncertainty in the prediction of the average surface settlement due to the inherent ground nonuniformity as discussed earlier (with Fig. 6.15(a)).
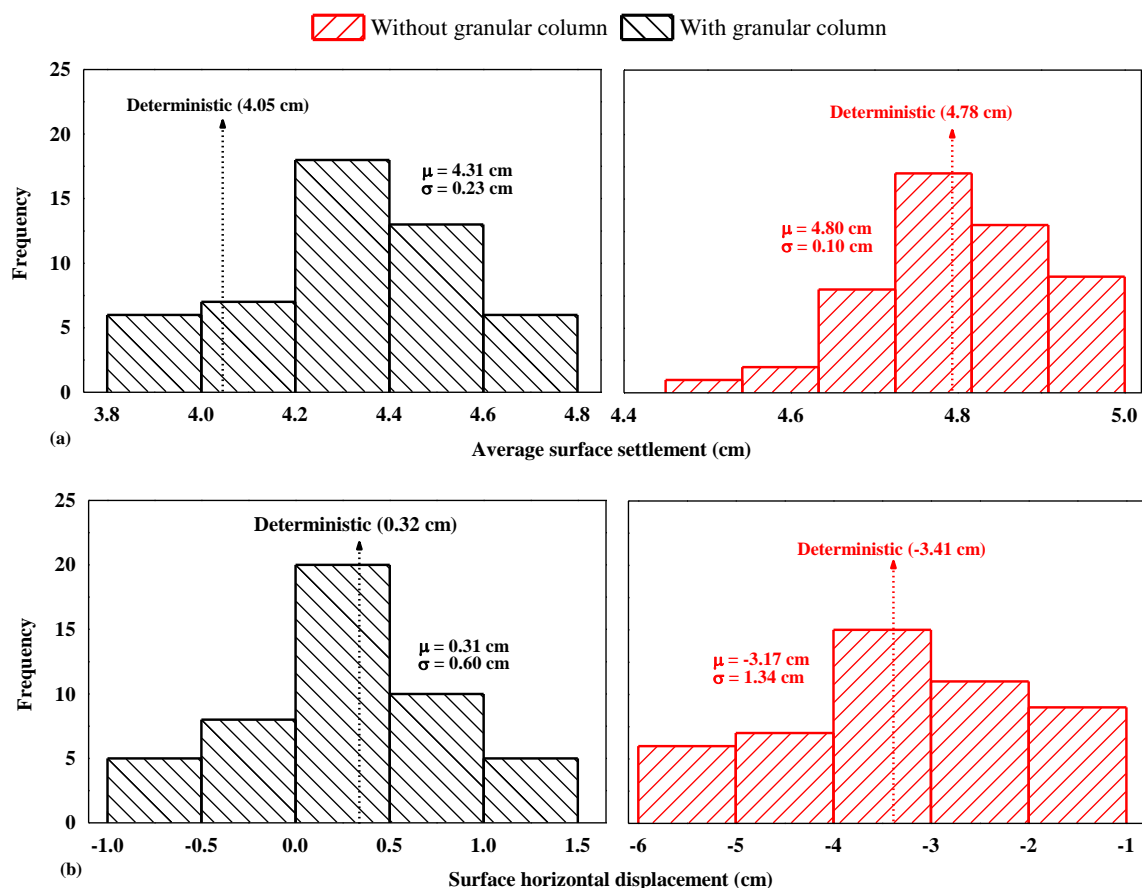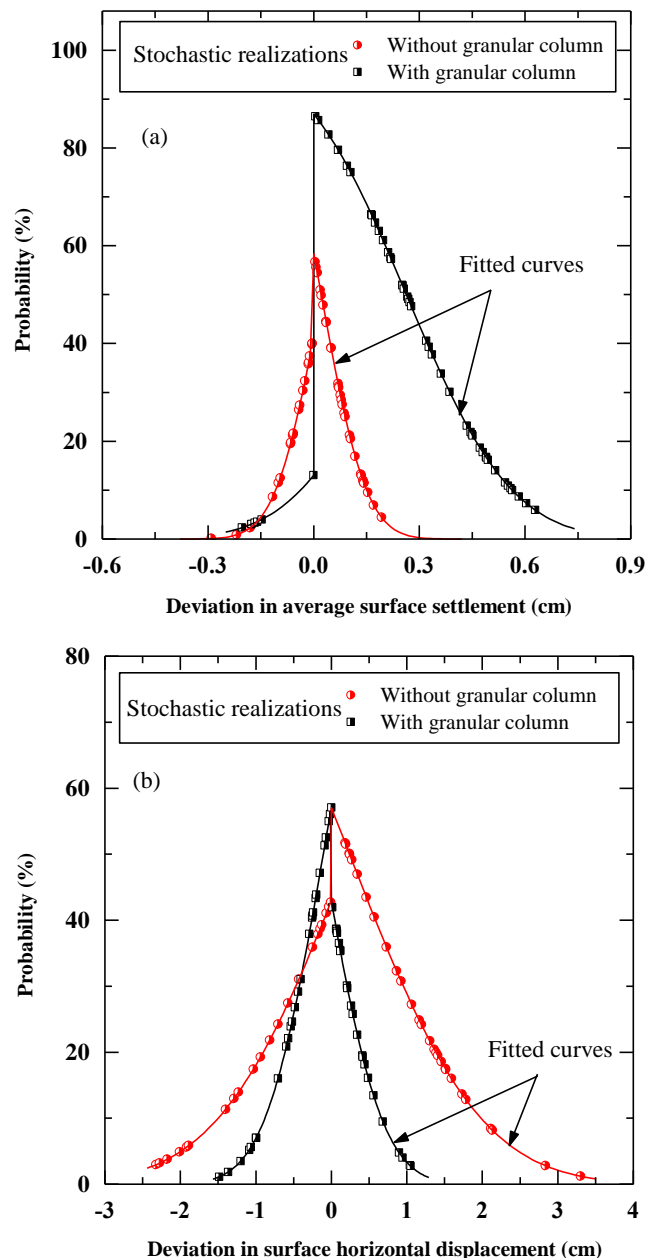

Fig. 6.16. Probability of deviation from the deterministic values for the ground with and without granular column: (a) for average surface settlement and (b) for surface horizontal displacement

Fig. 6.16(b) shows that total probabilities of stochastic surface horizontal displacement being deviated on the negative side from the deterministic value are 57.05 and 42.68%, respectively, and on the positive side from the deterministic value are 41.92 and 51.69%, respectively, for the grounds with and without granular column. The maximum deviation of the horizontal surface displacement on the negative side is 1.48 cm (with a 1.12% probability of occurrence) and 2.32 cm (with a 2.96% probability of occurrence), respectively, for the ground with and without granular column. The maximum deviation of the horizontal surface displacement on the positive side is 1.04 cm (with a 2.74% probability of occurrence) and 3.30 cm (with a 1.05% probability of occurrence), respectively, for the grounds with and without granular column. A relatively larger deviation from the deterministic value associated with a significant probability of occurrence in the case of the ground without granular column signifies that the presence of granular column favorably affects the uncertainty in the prediction of the horizontal surface displacement due to the inherent ground nonuniformity as discussed earlier (with Fig. 6.15(b)).

6.3.2   *Stochastic bounds of excess pore water pressure ratio*

Spatial nonuniformity is prone to influence the evolution of EPWP, which may significantly affect the deformation mechanism of the ground (as witnessed in Figs. 6.15 and 6.16). The efficacy of the granular column to restrict the r_u (for uniform ground, with deterministic analyses) is discussed in Fig. 6.7. Similarly, the contours of r_u at different depths are estimated for each realization from the series of stochastic analyses considering the spatial nonuniformity of the ground with the granular column to trace the worst performance (the largest values of r_u) and best performance (smallest values of r_u) of the granular column as shown in Fig. 6.17. The contours of r_u in Fig. 6.17(b) are significantly larger than the contours of r_u shown in Fig. 6.17(a), which implies that the performance of granular column per the restriction of EPWP may be compromised due to the nonuniformity of the ground. The values of r_u in Figs. 6.7(b) (deterministic case) and 6.17(b) (largest values of r_u based on stochastic analyses) signifies that the nonuniformity in the ground prone to adversely affect the performance of the granular column to restrict the r_u.
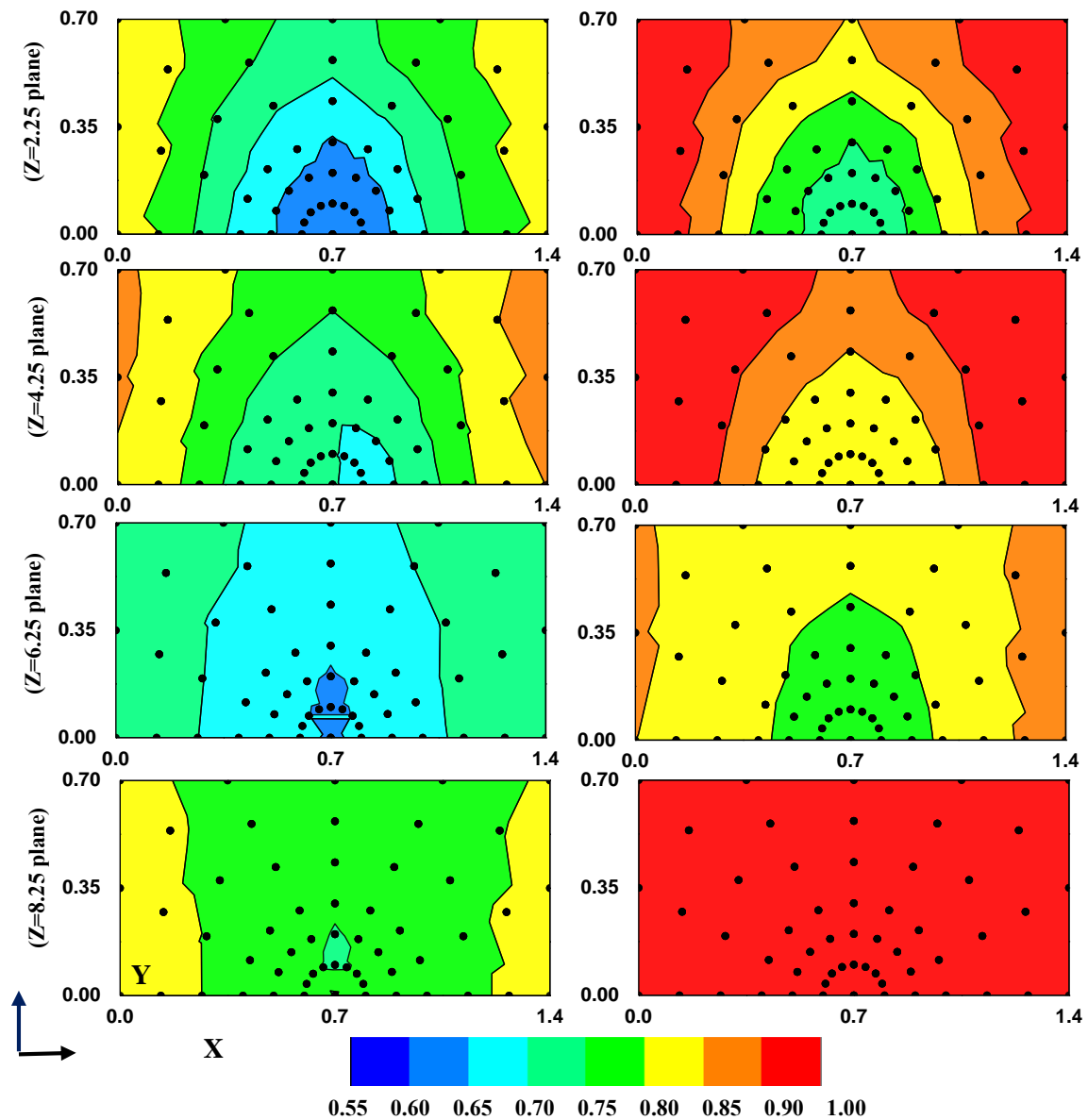
Fig. 6.17. Contours of r_u of ground with granular column at different depths (planes Z = 2.25, 4.25, 6.25, and 8.25 m): (a) smallest values of r_u, and (b) largest values of r_u from the series of stochastic analyses

6.3.3   *Stochastic surface spectral response spectrum*

The frequency and magnitude of the input shaking fluctuate (amplify or attenuate depending upon the inertial and kinematic interaction) as the wave propagates toward the surface of the ground (Kumar et al. 2019a). The presence of a granular column helps to minimize the extent

of liquefaction (Fig. 6.7), which may affect the filtration of the high-frequency content of the incident wave and the amplification in the magnitude of low-frequency content of incident wave. For each realization, the displacement time history of the top surface of the ground is recorded during the shaking. The spectral horizontal displacement is calculated for a wide range of periods (T = 0.0005 - 4 s), considering a damping ratio of 5%.
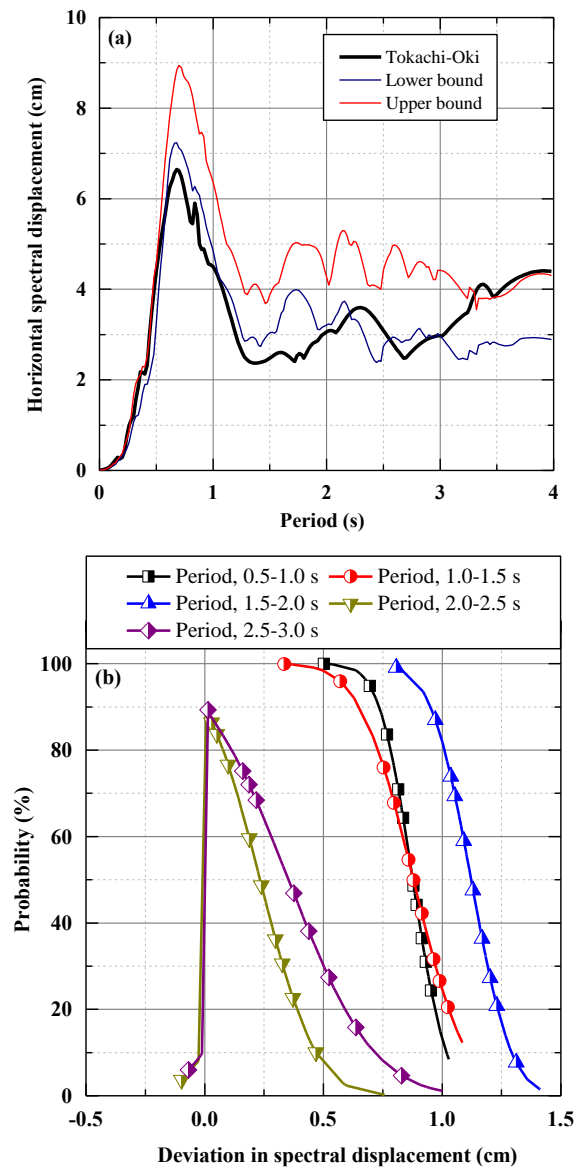
Fig. 6.18. The kinematic response of the ground with granular column: (a) upper and lower bound of displacement response spectra (with 5% damping) at the top surface (Z= 0 m) of the ground from 50 realizations and (b) probability of deviation of average spectral displacement (for different period range) from their respective values for Tokachi-Oki ground motion

Fig. 6.18(a) shows the upper and lower bounds of surface spectral horizontal displacement in comparison with the one for applied Tokachi-Oki ground motion at the base. The stochastic bound of surface spectral horizontal displacement of the top surface of the ground is significantly larger than the corresponding values for Tokachi-Oki ground motion for a wide range of the periods (0.55 - 3.0 s). The probability of deviation of stochastic spectral horizontal displacement (for a different range of periods) from the corresponding values for Tokachi-Oki ground motion is evaluated and shown in Fig. 6.18(b). The total probabilities of stochastic spectral displacement being more than the deterministic value are found in the range of 88.43 to 99.08% for structure periods 0.5 – 3.0 s. The maximum deviation in the spectral displacement from deterministic value is found in the range of 0.59 cm (with 2.68% probability of occurrence) to 1.31 cm (with 7.74% probability of occurrence) for structure periods 0.5 – 3.0 s. This wide range of deviation in spectral displacement from their deterministic values emphasizes that the nonuniformity of the ground (traced with the presented stochastic analyses) is vital to consider for a better insight of the surface response spectrum.

6.3.4   *Effects of different ground motions*

Kinematic and inertial interaction between soil and the granular column plays a vital role in the manifestation of the overall deformation of the ground during the dynamic event. The frequency and magnitude of the input shaking fluctuate as the wave propagates toward the surface of the ground. This alteration significantly depends on the anisotropic conditions resulted due to spatial nonuniformity, relative stiffness, the extent of liquefaction, and deformation pattern of the ground during the dynamic excitation. Each earthquake ground motion possesses a unique signature of frequency content, peak acceleration (PA), and time duration. The results associated with Tokachi-Oki ground motion (discussed so far) may not necessarily represent the overall scenario of the performance of the granular column. Ten different ground motions (GM1-GM10, see Table 6.3) are selected from the Pacific Earthquake Engineering Research (PEER) using the procedure by Jayaram et al. (2011). The ground motions possess a broad spectrum of frequency content and PA of interest, per Raymajhi et al. (2016). The response spectra (damping 5%) for Tokachi-Oki and ten selected ground motions along with their median are shown in Fig. 6.19.
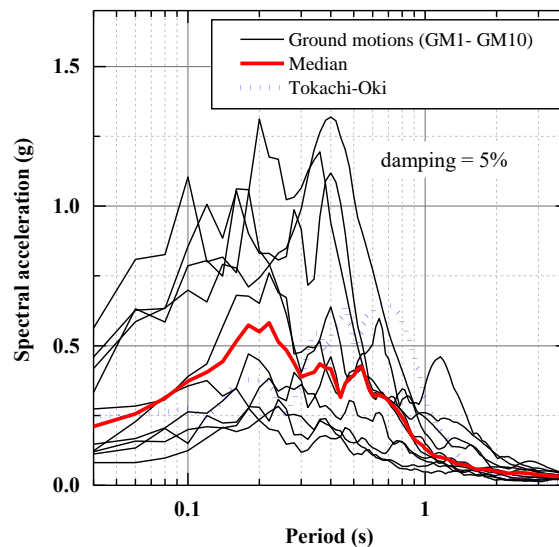
Fig. 6.19. Spectral accelerations for different ground motions (see Table 6.3)

Selected ten ground motions are scaled for PA = 0.2, 0.4, and 0.6g. The ground motions possess cumulative absolute velocity (CAV) and Arias Intensity (AI) in the range of 2.3 – 34 m/s and 0.2 – 10.5 m/s, respectively. Deterministic analyses (Toyoura sand with D_R = 50%) are carried out for these scaled ground motions to examine the fluctuation in the average settlement and horizontal displacement of the top surface of the ground with the granular column in comparison with the Tokachi-Oki ground motion. Fig. 6.20(a) shows that the deterministic average surface settlement for Tokachi-Oki ground motion (= 4.05 cm) is larger than the average surface settlement for all ten ground motions (GM1-GM10) of PA = 0.2g. Similar trends are observed for eight ground motions of PA = 0.4 and 0.6g except for two ground motions with the larger deterministic average surface settlement than Tokachi-Oki ground motion. However, a significant deviation in the horizontal surface displacement is observed for several selected ground motions from the corresponding value for Tokachi-Oki ground motion (= 0.32 cm), as shown in Fig. 6.20(b). The average surface settlement is found to be better correlated with the CAV and AI than the PA of selected ground motions. Fig. 6.20(a) depicts a strong correlation between CAV, AI and average surface settlement. However, horizontal surface displacement is found to be better correlated with the PA than CAV and AI of selected ground motions as depicted in Fig. 6.20(b). The horizontal surface displacement primarily governed by the overall stiffness of the ground (as discussed with Figs. 6.8 and 6.9), and thus large PA of the ground motion may adversely affect the stiffness degradation of the granular

column during the dynamic event. These statistics signify that a wide spectrum of, PA, CAV, and AI of the ground motion is important to consider for a reliable estimate of the ground deformation.
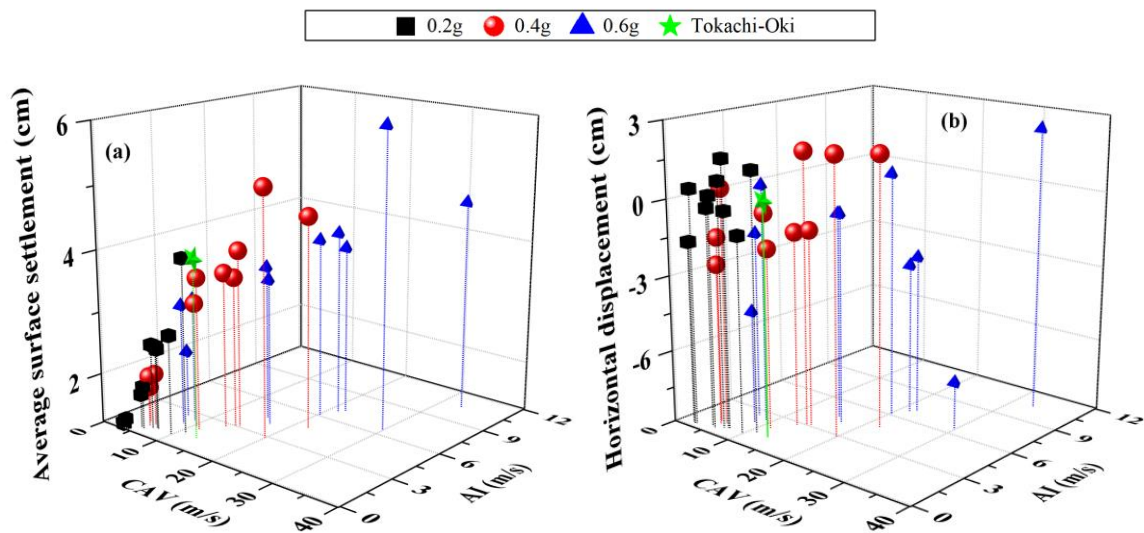
Fig. 6.20. The deterministic response of ten scaled ground motions for the ground with granular column: (a) average surface settlement and (b) surface horizontal displacement

Table 6.3. Earthquake ground motions (after Raymajhi et al., 2016)

Tag	Earthquake name	Year	Magnitude
GM1	Northridge 1	1994	6.69
GM2	Hector Mine 1	1999	7.13
GM3	Hector Mine 1	1999	7.13
GM4	Taiwan SMART 1	1986	7.3
GM5	Loma Prieta 1	1989	6.93
GM6	Northridge 2	1994	6.69
GM7	Alaska	2002	7.9
GM8	Loma Prieta 2	1989	6.93
GM9	Northridge 2	1994	6.69
GM10	Loma Prieta 3	1989	6.93
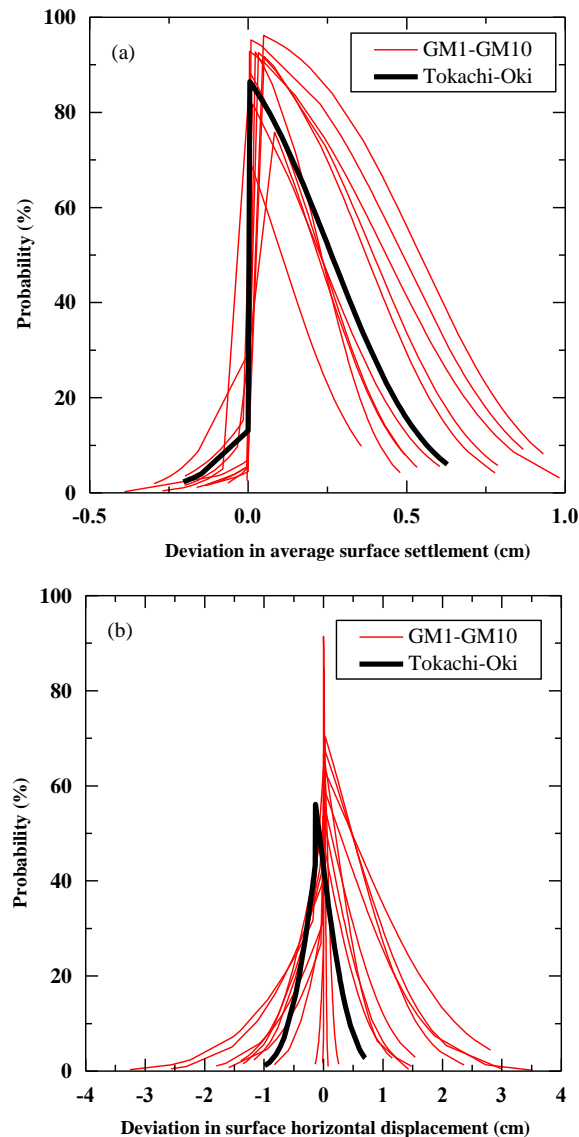
Fig. 6.21. Probability of deviation from the deterministic values for the ground with the granular column for all the ground motions scaled with peak acceleration = 0.6g: (a) for average surface settlement and (b) for surface horizontal displacement

Stochastic analyses are carried out for all the ground motions GM1-GM10 with PA = 0.6g, and the probabilities of deviation from the deterministic values of average settlement and horizontal displacement of the top surface of the ground are evaluated as shown in Fig. 6.21. The interpretation is made in comparison with the respective probability of deviations for Tokachi-Oki ground motion (as reported in Fig. 6.16) to trace the qualitative effects of frequency content, PA, and time duration of the ground motion. Fig. 6.21(a) shows the

probability of deviation of the average surface settlement from the deterministic values. It is evident that the deviation in the average surface settlement and probabilities of exceedance (especially on the positive side) are significantly exceeding the values traced with the Tokachi-Oki ground motion for several ground motions. Fig. 6.21(b) shows the probability of deviation of the horizontal surface displacement from the deterministic values. It is evident that the deviation in the horizontal surface displacement for several ground motions are significantly exceeding the values traced with the Tokachi-Oki ground motion. Besides, the probabilities of exceedance for several ground motions are significantly larger for the deviations in both the positive and negative sides. This observation corroborates the fact that the characteristics of the ground motion (frequency content, PA, and time duration) prone to significantly affect the deformation of the ground.

6.4 Summary

A reliability assessment of the performance of equally-spaced granular columns in a nonuniform liquefiable ground is carried out to mitigate the liquefaction-induced ground deformation using three-dimensional (3D) stochastic numerical analyses. The PDMY02 elastoplastic soil constitutive model is used to simulate the dynamic behavior of the liquefiable ground treated with the granular column. The nonuniformity in the ground is mapped with the stochastic realizations of the overburden and energy-corrected, equivalent clean sand, SPT $(N1)_{60cs}$ values using a spatially correlated Gaussian random field. It is found that the presence of a granular column increases the overall stiffness and minimizes the liquefaction extent of the ground. The favorable shear reinforcement within the ground is observed due to the granular column. However, incompatibility in shear strain reduction is also noted due to the complex deformation mechanism. The spatial nonuniformity in the ground is found to affect the liquefaction-induced ground deformation. Stochastic results depicted that the presence of the granular column reduces the uncertainty in the estimation of horizontal displacement; however, it adversely affects the uncertainty in the prediction of the average surface settlement of the ground. The stochastic displacement spectra exhibited that the nonuniformity of the ground should be taken into account, especially for long-period structures. Besides, the wide range of deviation in spectral displacement from their deterministic value emphasizes that the

nonuniformity of the ground is important to consider for a better insight of the surface response spectrum. It is found that the characteristics of ground motions (CAV, AI, and PA) significantly affect the liquefaction-induced ground deformation. Stochastic results emphasize that the reliability assessment of the performance of the granular column is essential for better engineering judgment. The presented probabilistic assessment traces the conservative nature of the deterministic performance of granular column and possesses significant practical importance. The findings of shear reinforcement, strain incompatibility, probabilistic estimates of liquefaction-induced ground deformation, stochastic bound of the evolution of EPWP, and effects of different ground motions will assist in bridging the gap of risk information while designing the granular columns with conventional design charts. For a generalized framework to incorporate the reduction in the epistemic uncertainty, it is necessary to investigate further the full scenario of the gravel drainage system with the foundation-structure system and different ground conditions

Chapter 7. Conclusions and recommendations

Liquefaction has caused devastating damage to the built environment on shallow foundations such as settlement, tilting, and sinking all over the world during many past earthquakes. Over the past few decades, extensive efforts and contributions have been made by geotechnical earthquake engineering society to grasp the physics behind the liquefaction and for the development of the remedial measures against the liquefaction-induced effects. Soil remediation measures are requisite for liquefaction prone sites. Liquefaction mitigation techniques primarily can be categorized into three categories, i.e., soil reinforcement, desaturation, and drainage improvement. The probable vulnerability of existing structures founded on the soil, which is prone to liquefaction, continued to be a significant concern. The challenging task is to assess the mitigation techniques which could be adopted as non-disruptive mitigation for already developed sites explicitly having important and vulnerable structures. The other essential aspects of liquefaction mitigation methods are achieving the liquefaction mitigation in a large area at low cost and combining the liquefaction mitigation in an environmental friendliness manner.

Implementation of a suitable mitigation technique is essential for any site which is prone to seismically induced liquefaction during the commencement of any project. Conventional liquefaction mitigation techniques existed in practice, performs reasonably well in case of a small earthquake. However, their effectiveness during a moderate or strong earthquake is still poorly understood. There are several case histories where mitigation measures did not work as expected during strong earthquake. The presented research aims for the development and investigation of the efficacy of liquefaction mitigation techniques under different strong shakings. Initially, liquefaction-induced effects on shallow foundation resting on presumably uniform deposit of a liquefiable ground are investigated. Then the reliability of centrifuge experiment is investigated considering the nonuniformity in the centrifuge model. Centrifuge experiments are carried out to examine the efficacy of partial saturation as a liquefaction mitigation measure. A unique hybrid foundation is also developed to mitigate the liquefaction-induced effects under different strong earthquakes. The proposed hybrid foundation is a combination of the gravel drainage system and friction piles having spiral blades devised under the footing as a hybrid mitigation technique against the liquefaction-induced effects. The gravel

drainage system is susceptible to the nonuniformity of the ground and hence the reliability assessment of the performance of a granular column is investigated.

7.1 Conclusions

Chapter 2 discusses the liquefaction-induced effects on shallow foundation and reliability assessment of centrifuge test considering the nonuniformity in the centrifuge model. Dynamic centrifuge modeling has been widely used to understand the liquefaction–induced effects on shallow foundations resting on presumably uniform deposits of clean and loose to medium dense sand. Besides, the use of dynamic centrifuge model test results to validate their soil constitutive models and finite element numerical models is extensive. In both cases, the model ground is usually considered to have uniform soil properties, which is, however prone to spatial nonuniformity and may affect engineering judgment based on physical modeling. Centrifuge test depicted that the ground may remain in liquefaction state even quite after the strong earthquake and shallow foundation is prone to undergo severe deformation. The deformation is likely to take place during both co-shaking and post-shaking phase of the strong earthquake. The nonuniformity in the centrifuge model affects the liquefaction-induced effects on shallow foundation with variable degree of severity. It is observed that the stochastic average foundation settlement with different combinations of centrifuge model nonuniformity are comparable to the deterministic average foundation settlement. However, the nonuniformity in the centrifuge model is found to have significantly adverse impact on the tilt of the foundation. Moreover, the liquefaction extent in the model ground varies with the centrifuge model's nonuniformity and is correlated with the deformation of the foundation-structure system. The stochastic displacement spectra exhibited that the nonuniformity of the centrifuge model ground should be taken into account, especially for long-period structures. The reliability assessment of the centrifuge model test results is essential for better engineering judgment associated with a desired level of confidence. The probabilistic correlations between nonuniformity of the centrifuge model and the response of foundation-structure system possess significant practical importance and provides useful information to assess the reliability of the physical model tests by numerical procedure.

Chapter 3 discusses the efficacy of induced partial saturation to mitigate the liquefaction-induced effects on shallow foundations under strong earthquake. Induced partial saturation is one of the novel techniques to increase the liquefaction resistance of the liquefiable ground. Drainage-recharge method is used to make the centrifuge model ground partially saturated. Centrifuge test results consolidated the fact that the compressibility of pore fluid increases because of inclusion of the air voids within the partially saturated ground. Also, the partially saturated ground showed overall less permeability in comparison with the fully saturated ground. Larger compressibility of pore fluid and smaller permeability of the partially saturated ground in comparison with fully saturated ground resulted in favorable evolution of EPWP. Induced partial saturation is found to mitigate the deformation of foundation-structure system. However, the kinematic seismic demand experienced by foundation-structure systems is relatively large in case of partially saturated ground in comparison with fully saturated ground.

Chapter 4 discusses the development scheme and performance of a hybrid foundation to mitigate the liquefaction-induced effects on shallow foundation. The developed hybrid foundation is a combination of the gravel drainage system and friction piles having spiral blades devised under the footing as a hybrid mitigation technique. After the life span of the targeted structures, the hybrid foundation is planned to be re-used for a different structure with keeping the gravel drains and re-installing the friction piles. Treating the ground with gravel drainage system found to be useful to mitigate the liquefaction-induced deformation. The presence of gravel drainage increased the dissipation rate (through radial flow towards the gravel drainage zone) of generated EPWP and reduced the post-shaking settlement. Centrifuge tests results depict that the friction piles having spiral blades at bottom served an excellent means of frictional resistance against the settlement of shallow foundation and reduced the overall deformation of shallow foundation significantly through combined inertial and kinematic interaction with foundation-superstructure and model ground. It is found that the developed hybrid foundation is able to mitigate liquefaction-induced effects on shallow foundation during the strong earthquake.

Chapter 5 discusses the efficacy of induced partial saturation and hybrid foundation under different strong ground motions. Any structure prone to experience several moderate to strong earthquakes during its lifespan. Therefore, the effectiveness of these mitigation techniques is found to be affected under various level of earthquakes. During Tohoku (second) ground motion, the overall performance of partially saturated ground is found to be diminished

in comparison with the one witnessed during Tokachi-Oki (first) ground motion. It is observed that the maximum potential volumetric compressibility reduces after the first strong ground motion. However, the available capacity of potential volume compressibility is found quite significant after the strong Tohoku ground motion which signifies the novelty of induced partial saturation to increase the liquefaction resistance of the partially saturated ground. The overall performance of induced partial saturation is found satisfactory. However, much research is needed to develop the implementation guidelines and case history data for validation of site specific performance of induced partial saturation. The performance of hybrid foundation is found to be diminished in terms of overall footing settlement during Tohoku ground motion. The alteration in ground condition after Tokachi-Oki ground motion significantly affected the performance of hybrid foundation during Tohoku ground motion.

Chapter 6 discusses the reliability assessment of the performance of a granular column considering the nonuniformity of the ground. Numerical results echo with the general notion that the presence of a granular column increases the overall stiffness and minimizes the liquefaction extent of the ground. The favorable shear reinforcement within the ground is observed due to the granular column. However, incompatibility in shear strain reduction is also noted due to the complex deformation mechanism of the ground treated with granular column. The spatial nonuniformity in the ground is found to affect the liquefaction-induced ground deformation. Stochastic results depicted that the presence of the granular column reduces the uncertainty in the estimation of horizontal displacement; however, it adversely affects the uncertainty in the prediction of the average surface settlement of the ground. The stochastic displacement spectra exhibited that the nonuniformity of the ground should be taken into account, especially for long-period structures. Besides, the wide range of deviation in spectral displacement from their deterministic value emphasizes that the nonuniformity of the ground is important to consider for a better insight of the surface response spectrum. It is found that the characteristics of ground motions (CAV, AI, and PA) significantly affect the liquefaction-induced ground deformation. Stochastic results emphasize that the reliability assessment of the performance of the granular column is essential for better engineering judgment. The presented probabilistic assessment traces the conservative nature of the deterministic performance of granular column and possesses significant practical importance. The findings of shear reinforcement, strain incompatibility, probabilistic estimates of liquefaction-induced ground deformation, stochastic bound of the evolution of EPWP, and

effects of different ground motions will assist in bridging the gap of risk information while designing the granular columns with conventional design charts. For a generalized framework to incorporate the reduction in the epistemic uncertainty, it is necessary to investigate further the full scenario of the gravel drainage system with the foundation-structure system and different ground conditions.

7.2 Recommendations

The presented research aims for the better understanding of liquefaction-induced effects on shallow foundations and gives insight into the physical modeling of different remedial measures and their reliability assessment. The probabilistic correlations between nonuniformity of the centrifuge model and the response of foundation-structure system is found to have significant practical importance which may useful information to assess the reliability of the physical model tests by numerical procedure. However, for a generalized framework to incorporate the reduction in the epistemic uncertainty, it is necessary to further investigate the full scenario of model preparation with the foundation-structure system and different ground conditions. Induced partial saturation is found to be effective to mitigate the liquefaction induced effects on shallow foundations. However, there is a vast scope of further research to develop the guidelines for the implementation of the induced partial saturation into practice at large scale. The alteration in ground condition after Tokachi-Oki ground motion significantly affected the performance of hybrid foundation during Tohoku ground motion. This observation highlighted the need of further improvement in the development scheme to gain the full capabilities of proposed hybrid foundation under different strong ground motions. The reliability assessment of the performance of the granular column is found to be necessary for better engineering judgment associated with a desired level of confidence. However, the inclusion of site specific factors, for instance, densification of the ground during the installation of array of granular columns are further recommended to be considered for a more explicit reliability assessment.

References

Adalier, K., and Elgamal, A. W. (2002). Seismic response of adjacent dense and loose saturated sand columns. Soil Dynamics and Earthquake Engineering, 22(2), 115-127. https://doi.org/10.1016/S0267-7261(01)00059-8.

Adalier, K., Elgamal, A., Meneses, J., and Baez, J. I. (2003). Stone columns as liquefaction countermeasure in non-plastic silty soils. Soil Dynamics and Earthquake Engineering, 23(7), 571-584. https://doi.org/10.1016/S0267-7261(03)00070-8

Adalier, K., and Elgamal, A. (2004). Mitigation of liquefaction and associated ground deformations by stone columns. Engineering Geology, 72(3-4), 275-291. https://doi.org/10.1016/j.enggeo.2003.11.001

Adamidis, O., and Madabhushi, G. S. (2019). Numerical modelling of post-liquefaction reconsolidation. In Online Proceedings: 2nd International Conference on Natural Hazards and Infrastructure (ICONHIC 2019) (p. 963). Innovation Center on Natural Hazards and Infrastructure.

Andrus, R. D., and Stokoe II, K. H. (2000). Liquefaction resistance of soils from shear-wave velocity. Journal of geotechnical and geoenvironmental engineering, 126(11), 1015-1025. https://doi.org/10.1061/(ASCE)1090-0241(2000)126:11(1015)

Arulanandan, K., and Scott, R. F. (1993). Verification of numerical procedures for the analysis of soil liquefaction problems. In International Conference on the Verification of Numerical Procedures for the Analysis of Soil Liquefaction Problems (1993: Davis, Calif.). AA Balkema. Atkinson, J. The mechanics of soils and foundations. CRC Press 2007.

Baez, J. I. (1995). A design model for the reduction of soil liquefaction by using vibro-stone columns. PhD thesis, University of southern California, USA.

Baez, J. I., and Martin, G. R. (1993, May). Advances in the design of vibro systems for the improvement of liquefaction resistance. In Symposium Ground Improvement (pp. 1-16).

Bardet JP, Oka F, Sugito M, and Yashima A. (1995) The Great Hanshin Earthquake disaster. Preliminary Investigation Rep., Dept. of Civil Engineering Univ. of Southern California, Los Angeles.

Bhattacharya, S., Hyodo, M., Goda, K., Tazoh, T., and Taylor, C. A. (2011). Liquefaction of soil in the Tokyo Bay area from the 2011 Tohoku (Japan) earthquake. Soil Dynamics and Earthquake Engineering, 31(11), 1618-1628. 31(11):1618-1628. https://doi.org/10.1016/j.soildyn.2011.06.006.

Bird, J. F., and Bommer, J. J. (2004). Earthquake losses due to ground failure. Engineering geology, 75(2), 147-179. https://doi.org/10.1016/j.enggeo.2004.05.006

Bishop, A. W., and Blight, G. E. (1963). Some aspects of effective stress in saturated and partly saturated soils. Geotechnique, 13(3), 177-197. https://doi.org/10.1680/geot.1963.13.3.177.

Bolton, M. D., Gui, M. W., Garnier, J., Corte, J. F., Bagge, G., Laue, J., and Renzi, R. (1999). Centrifuge cone penetration tests in sand. Géotechnique, 49 (4), 543-552.

Borcherdt, R. D. (1994). Estimates of site-dependent response spectra for design (methodology and justification). Earthquake spectra, 10(4), 617-653. 10(4):617-653. https://doi.org/10.1193/1.1585791.

Bouckovalas, G. D., Papadimitriou, A. G., Kondis, A., and Bakas, G. J. (2006, September). Equivalent-uniform soil model for the seismic response analysis of sites improved with inclusions. In Proc., 6th European Conf. on Numerical Methods in Geotechnical Engineering (pp. 801-807).

Boulanger, R. W., Idriss, I. M., Stewart, D. P., Hashash, Y., and Schmidt, B. (1998). Drainage capacity of stone columns or gravel drains for mitigating liquefaction. In Drainage capacity of stone columns or gravel drains for mitigating liquefaction (pp. 678-690). American Society of Civil Engineers.

Boulanger, R. W., and Ziotopoulou, K. (2017). PM4Sand (Version 3.1): A sand plasticity model for earthquake engineering applications. Center for Geotechnical Modeling Report No. UCD/CGM-17/01, Department of Civil and Environmental Engineering, University of California, Davis, Calif.

Boulanger, R. W., and Idriss, I. M. (2014). CPT and SPT based liquefaction triggering procedures. Report No. UCD/CGM.-14, 1.

Bray, J. D., Stewart, J. P., Baturay, M. B., Durgunoglu, T., Onalp, A., Sancio, R. B., ... and Barka, A. (2000). Damage patterns and foundation performance in Adapazari. Earthquake Spectra, 16(S1), 163-189. https://doi.org/10.1193/1.1586152

Brennan, A. J., Thusyanthan, N. I., and Madabhushi, S. P. (2005). Evaluation of shear modulus and damping in dynamic centrifuge tests. Journal of Geotechnical and Geoenvironmental Engineering, 131(12), 1488-1497. https://doi.org/10.1061/(ASCE)1090-0241(2005)131:12(1488).

Brennan, A. J., and Madabhushi, S. P. G. (2006). Liquefaction remediation by vertical drains with varying penetration depths. Soil Dynamics and Earthquake Engineering, 26(5), 469-475. https://doi.org/10.1016/j.soildyn.2005.10.001

Brennan, A. J., and Madabhushi, S. P. G. (2002). Effectiveness of vertical drains in mitigation of liquefaction. Soil Dynamics and Earthquake Engineering, 22(9-12), 1059-1065. https://doi.org/10.1016/S0267-7261(02)00131-8.

Byrne, P. M., Park, S. S., Beaty, M., Sharp, M., Gonzalez, L., and Abdoun, T. (2004). Numerical modeling of liquefaction and comparison with centrifuge tests. Canadian Geotechnical Journal, 41 (2), 193-211. https://doi.org/10.1139/t03-088

Chen, L., Ghofrani, A., and Arduino, P. (2020). Prediction of LEAP-UCD-2017 centrifuge test results using two advanced plasticity sand models. In Model Tests and Numerical Simulations of Liquefaction and Lateral Spreading (pp. 423-439).

Chiaro, G., Kiyota, T., and Koseki, J. (2013). Strain localization characteristics of loose saturated Toyoura sand in undrained cyclic torsional shear tests with initial static shear. Soils and Foundations, 53 (1), 23-34. https://doi.org/10.1016/j.sandf.2012.07.016

Chiaro, G., Koseki, J., and Sato, T. (2012). Effects of initial static shear on liquefaction and large deformation properties of loose saturated Toyoura sand in undrained cyclic torsional shear tests. Soils and Foundations, 52 (3), 498-510. https://doi.org/10.1016/j.sandf.2012.05.008

Christian, J. T., Ladd, C. C., and Baecher, G. B. (1994). Reliability applied to slope stability analysis. Journal of Geotechnical Engineering, 120 (12), 2180-2207. https://doi.org/10.1061/(ASCE)0733-9410(1994)120:12(2180)

Constantine, P. G., and Wang, Q. (2012, 2020). Random field simulation. < http://www. mathworks. com/matlabcentral/fileexchange/27613-random-field-simulation>

Cubrinovski M, and McCahon I. (2012). Short term recovery project 7, CBD foundation damage. Natural Hazards Research Platform. Christchurch, New Zealand, University of Canterbury.

Dashti, S., Bray, J. D., Pestana, J. M., Riemer, M., and Wilson, D. (2010). Centrifuge testing to

evaluate and mitigate liquefaction-induced building settlement mechanisms. Journal of geotechnical and geoenvironmental engineering, 136(7), 918-929. https://doi.org/10.1061/(ASCE)GT.1943-5606.0000306.

Dashti, S., and Bray, J. D. (2013). Numerical simulation of building response on liquefiable sand. Journal of Geotechnical and Geoenvironmental Engineering, 139 (8), 1235-1249. https://doi.org/10.1061/(ASCE)GT.1943-5606.0000853

Dashti, S., Bray, J. D., Pestana, J. M., Riemer, M., and Wilson, D. (2009). Mechanisms of seismically induced settlement of buildings with shallow foundations on liquefiable soil. Journal of geotechnical and geoenvironmental engineering, 136 (1), 151-164. https://doi.org/10.1061/(ASCE)GT.1943-5606.0000179

Dobry, R., and Liu, L., (1992). Centrifuge modeling of soil liquefaction. In Proc., 10th World Conf. on Earthquake Engineering, 6801-6809.

Duncan, J. M. (2000). Factors of safety and reliability in geotechnical engineering. Journal of geotechnical and geoenvironmental engineering, 126 (4), 307-316. https://doi.org/10.1061/(ASCE)1090-0241(2000)126:4(307)

Elgamal, A. W., Dobry, R., and Adalier, K., (1989). Small scale shaking table tests of saturated layered sand-silt deposits. In 2nd US-Japan Workshop on Soil Liquefaction Rep. No. 89, 32, 233-245.

Elgamal, A., Lu, J., and Forcellini, D. (2009). Mitigation of Liquefaction-Induced Lateral Deformation in a Sloping Stratum: Three-dimensional Numerical Simulation. Journal of Geotechnical and Geoenvironmental Engineering, ASCE 35 (11): 1672-1682. https://doi.org/10.1061/(ASCE)GT.1943-5606.0000137

Elgamal, A., Yang, Z., Lai, T., Kutter, B. L., and Wilson, D. (2005). Dynamic response of saturated dense sand in laminated centrifuge container. Journal of Geotechnical and Geoenvironmental Engineering, 131 (5), 598-609. https://doi.org/10.1061/(ASCE)1090-0241(2005)131:5(598)

Eseller-Bayat, E., Yegian, M. K., Alshawabkeh, A., and Gokyer, S. (2013). Liquefaction response of partially saturated sands. I: Experimental results. Journal of Geotechnical and Geoenvironmental Engineering, 139(6), 863-871. https://doi.org/10.1061/(ASCE)GT.1943-5606.0000815.

Fredlund, D. G., and Rahardjo, H. (1993). Soil mechanics for unsaturated soils. John Wiley and Sons.

Goughnour, R. R., and Pestana, J. M. (1998). Mechanical behavior of stone columns under seismic loading. Proc. 2nd Int. Conf. on ground improvement techniques, Singapore, 157-162.

Cubrinovski, M., Green, R. A., Wotherspoon, L., Allen, J., Bradley, B., Bradshaw, A., ... and Pender, M. (2011). Geotechnical reconnaissance of the 2011 Christchurch, New Zealand earthquake. Report of the National Science Foundation, Version, 1(15), 1-22.

Gallagher P.M, and Mitchell J.K (2002). Influence of colloidal silica grout on liquefaction potential and cyclic undrained behavior of loose sand. Soil Dyn Earthq Eng 22(9):1017–1026.

Green, R. A., Olgun, C. G., and Wissmann, K. J. (2008). Shear stress redistribution as a mechanism to mitigate the risk of liquefaction. In Geotechnical earthquake engineering and soil dynamics IV (pp. 1-10).

Griffiths, D. V., and Fenton, G. A. (2008). Risk assessment in geotechnical engineering (pp. 381-399). Hoboken, New Jersey: John Wiley and Sons, Inc.

Hardin, B. O., and Drnevich, V. P. (1972). Shear modulus and damping in soils: design equations and curves. Journal of Soil Mechanics and Foundations Div, 98(sm7).

Hausler, E. A., and Sitar, N., (2001). Performance of soil improvement techniques in earthquakes.

He, J., Chu, J., and Ivanov, V. (2014). Mitigation of liquefaction of saturated sand using biogas. In Bio-and Chemo-Mechanical Processes in Geotechnical Engineering: Géotechnique Symposium in Print 2013 (pp. 116-124). ICE Publishing.

Huang, Y., and Wen, Z. (2015). Recent developments of soil improvement methods for seismic liquefaction mitigation. Natural Hazards, 76(3), 1927-1938.

Ishihara, K., Haeri, S. M., Moinfar, A. A., Towhata, I., and Tsujino, S. (1992). Geotechnical aspects of the June 20, 1990 Manjil earthquake in Iran. Soils and Foundations, 32(3), 61-78. https://doi.org/10.3208/sandf1972.32.3_61.

Ishihara, K., and Yoshimine, M., (1992). Evaluation of settlements in sand deposits following liquefaction during earthquakes. Soils and foundations 32 (1), 173-188. https://doi.org/10.3208/sandf1972.32.173

Iwasaki, T., Arakawa, T., and Tokida, K. I. (1984). Simplified procedures for assessing soil liquefaction during earthquakes. International Journal of Soil Dynamics and Earthquake Engineering, 3 (1), 49-58. https://doi.org/10.1016/0261-7277(84)90027-5

Japanese Geotechnical Society (1992). Remedial Measures Against Soil Liquefaction: From investigation and design to implementation.

Jayaram, N., Lin, T., and Baker, J. W. (2011). A computationally efficient ground motion selection algorithm for matching a target response spectrum mean and variance. Earthquake Spectra 27(3): 797-815. https://doi.org/10.1193/1.3608002

Karamitros, D. K., Bouckovalas, G. D., and Chaloulos, Y. K. (2013). Insight into the seismic liquefaction performance of shallow foundations. Journal of Geotechnical and Geoenvironmental Engineering, 139(4), 599-607. https://doi.org/10.1061/(ASCE)GT.1943-5606.0000797.

Karimi, Z., and Dashti, S. (2015). Numerical and centrifuge modeling of seismic soil–foundation–structure interaction on liquefiable ground. Journal of Geotechnical and Geoenvironmental Engineering, 142 (1), 04015061. https://doi.org/10.1061/(ASCE)GT.1943-5606.0001346

Karimi, Z., and Dashti, S. (2016). Seismic performance of shallow founded structures on liquefiable ground: validation of numerical simulations using centrifuge experiments. Journal of Geotechnical and Geoenvironmental Engineering, 142 (6), 04016011. https://doi.org/10.1061/(ASCE)GT.1943-5606.0001479

Kayen, R. E., and Mitchell, J. K. (1997). Assessment of liquefaction potential during earthquakes by Arias intensity. Journal of Geotechnical and Geoenvironmental Engineering, 123(12), 1162-1174. https://doi.org/10.1061/(ASCE)1090-0241(1997)123:12(1162).

Khosravifar, A., Elgamal, A., Lu, J., and Li, J. (2018). A 3D model for earthquake-induced liquefaction triggering and post-liquefaction response. Soil Dynamics and Earthquake Engineering 110: 43-52. https://doi.org/10.1016/j.soildyn.2018.04.008

Kokusho, T., (1999). Water film in liquefied sand and its effect on lateral spread. Journal of Geotechnical and Geo-Environmental Engineering 125 (10), 817-826. https://doi.org/10.1061/(ASCE)1090-0241(1999)125:10(817)

Kramer, S. L. (1996). Geotechnical Earthquake Engineering Prentice Hall. New York.

Krinitzsky, E. L., and Hynes, M. E. (2002). The Bhuj, India, earthquake: lessons learned for earthquake safety of dams on alluvium. Engineering Geology, 66(3-4), 163-196. https://doi.org/10.1016/S0013-7952(02)00049-2.

Kumar, R., Horikoshi, K., and Takahashi, A. (2019). Centrifuge testing to investigate effects of partial saturation on the response of shallow foundation in liquefiable ground under strong sequential ground motions. Soil Dynamics and Earthquake Engineering, 125, 105728. https://doi.org/10.1016/j.soildyn.2019.105728

Kumar, R., Kasama, K., and Takahashi, A. (2020). Reliability assessment of the physical modeling of liquefaction-induced effects on shallow foundations considering nonuniformity in the centrifuge model. Computers and Geotechnics 122, 103558. https://doi.org/10.1016/j.compgeo.2020.103558

Kumar, R., Sawaishi, M., Horikoshi, K., and Takahashi, A. (2019). Centrifuge modeling of hybrid foundation to mitigate liquefaction-induced effects on shallow foundation resting on liquefiable ground. Soils and Foundations 59 (6): 2083-2098. https://doi.org/10.1016/j.sandf.2019.11.002

Kutter B. L., (2013). Effects of capillary number, Bond number, and gas solubility on water saturation of sand specimens. Can Geotech J. 50 (2), 133–144. https://doi.org/10.1139/cgj-2011-0250.

Law, H. K., and Lam, I. P. (2001). Application of periodic boundary for large pile group. Journal of geotechnical and geoenvironmental engineering, 127(10), 889-892. https://doi.org/10.1061/(ASCE)1090-0241(2001)127:10(889)

Li, Z., Kutter, B. L., Wilson, D. W., Sprott, K., Lee, J. S., and Santamarina, J. C. (2005). Needle probe application for high-resolution assessment of soil spatial variability in the centrifuge. In Site Characterization and Modeling (pp. 1-15).

Liu, L., and Dobry, R. (1997). Seismic response of shallow foundation on liquefiable sand. Journal of geotechnical and geoenvironmental engineering 123 (6), 557-567. https://doi.org/10.1061/(ASCE)1090-0241(1997)123:6(557)

Macedo, J., and Bray, J. D. (2018). Key Trends in Liquefaction-Induced Building Settlement. Journal of Geotechnical and Geoenvironmental Engineering, 144 (11), 04018076. https://doi.org/10.1061/(ASCE)GT.1943-5606.0001951

Marasini, N. P., and Okamura, M. (2015). Numerical simulation of centrifuge tests to evaluate

the performance of desaturation by air injection on liquefiable foundation soil of light structures. Soils and Foundations, 55(6), 1388-1399. https://doi.org/10.1016/j.sandf.2015.10.005.

Mazzoni, S., McKenna, F., Scott, M. H., and Fenves, G. L. (2006). Open system for earthquake engineering simulation user command-language manual.

Mitchell, J. K., Baxter, C. D., and Munson, T. C. (1995, October). Performance of improved ground during earthquakes. In Soil improvement for earthquake hazard mitigation (pp. 1-36). ASCE.

Mitchell, J. K., (1981). Soil improvement-state of the art report. In Proc., 11th Int. Conf. on SMFE 4, 509-565.

Montgomery, J., and Boulanger, R. W. (2016). Effects of spatial variability on liquefaction-induced settlement and lateral spreading. Journal of Geotechnical and Geoenvironmental Engineering, 143 (1), 04016086. https://doi.org/10.1061/(ASCE)GT.1943-5606.0001584

Nakai, S., and Sekiguchi, T. (2011). Damage due to liquefaction during the 2011 Tohoku earthquake. In Proc. of the International Symposium for CSMID (pp. 1-8).

Okamura, M., Ishihara, M., and Oshita, T. (2003). Liquefaction resistance of sand deposit improved with sand compaction piles. Soils and foundations, 43(5), 175-187. https://doi.org/10.3208/sandf.43.5_175.

Okamura, M., and Soga, Y. (2006). Effects of pore fluid compressibility on liquefaction resistance of partially saturated sand. Soils and Foundations, 46(5), 695-700. https://doi.org/10.3208/sandf.46.695.

Olarte, J., Paramasivam, B., Dashti, S., Liel, A., and Zannin, J. (2017). Centrifuge modeling of mitigation-soil-foundation-structure interaction on liquefiable ground. Soil Dynamics and Earthquake Engineering, 97, 304-323. https://doi.org/10.1016/j.soildyn.2017.03.014

Olgun, C. G., and Martin, II, J. R. (2008). Numerical modeling of the seismic response of columnar reinforced ground. In Geotechnical earthquake engineering and soil dynamics IV (pp. 1-11).

Phoon, K. K., and Ching, J. (2014). Risk and reliability in geotechnical engineering. CRC Press.

Phoon, K. K., and Kulhawy, F. H. (1999). Characterization of geotechnical variability. Canadian geotechnical journal, 36 (4), 612-624. https://doi.org/10.1139/t99-038

Popescu, R., and Prevost, J. H. (1993). Centrifuge validation of a numerical model for dynamic soil liquefaction. Soil Dynamics and Earthquake Engineering, 12 (2), 73-90. https://doi.org/10.1016/0267-7261(93)90047-U

Popescu, R., and Prevost, J. H. (1995). Reliability assessment of centrifuge soil test results. Soil Dynamics and Earthquake Engineering, 14 (2), 93-101. https://doi.org/10.1016/0267-7261(94)00037-H

Popescu, R., Prevost, J. H., and Deodatis, G. (2004). 3D effects in seismic liquefaction of stochastically variable soil deposits. In Risk and variability in geotechnical engineering.

Priebe, H. J., (1989). The prevention of liquefaction by vibro replacement. In Proceedings of the 2nd International Conference on Earthquake Resistant Construction and Design, 211-219.

Rayamajhi, D., Ashford, S. A., Boulanger, R. W., and Elgamal, A. (2016). Dense granular columns in liquefiable ground. I: shear reinforcement and cyclic stress ratio reduction. Journal of Geotechnical and Geoenvironmental Engineering, 142(7), 04016023. https://doi.org/10.1061/(ASCE)GT.1943-5606.0001474

Rayamajhi, D., Nguyen, T. V., Ashford, S. A., Boulanger, R. W., Lu, J., Elgamal, A., and Shao, L. (2014). Numerical study of shear stress distribution for discrete columns in liquefiable soils. Journal of Geotechnical and Geoenvironmental Engineering, 140(3), 04013034. https://doi.org/10.1061/(ASCE)GT.1943-5606.0000970

Rayhani, M. H., and El Naggar, M. H. (2008). Numerical modeling of seismic response of rigid foundation on soft soil. International Journal of Geomechanics, 8 (6), 336-346. https://doi.org/10.1061/(ASCE)1532-3641(2008)8:6(336)

Sancio, R., Bray, J. D., Durgunoglu, T., and Onalp, A. (2004, August). Performance of buildings over liquefiable ground in Adapazari, Turkey. In Proc., 13th World Conf. on Earthquake Engineering. Vancouver, Canada: Canadian Association for Earthquake Engineering.

Schaefer, V. R., Abramson, L. W., Drumheller, J. C., and Sharp, K. D. (1997). Ground improvement, ground reinforcement and ground treatment: developments 1987-1997. ASCE.

Schofield, A. N. (1981). Dynamic and earthquake geotechnical centrifuge modelling. In:

Proceedings of International conference on recent advances in geotechnical earthquake engineering and soil dynamics, University of Missouri-Rolla. MO, USA 1981;1081–1100.

Schofield, A. N. (1980). Cambridge geotechnical centrifuge operations. Geotechnique, 30 (3), 227-268. https://doi.org/10.1680/geot.1980.30.3.227

Seed, R. B., Cetin, K. O., Moss, R. E. S., Kammerer, A. M., Wu, J., Pestana, J. M., and Reimer, M. F. (2001). Recent advances in soil liquefaction engineering and seismic site response evaluation.

Seed, R. B., Dickenson, S. E., Reimer, M. F., Bray, J. D., Sitar, N., Mitchell, J. K., ... and Power, M. S. (1990). Preliminary report on the principal Geotechnical aspects of the October 17, 1989 Loma Prieta earthquake. Berkeley, University of California. Earthquake Engineering Research Center, 137.

Seed, H. B., and Booker, J. R. (1977). Stabilization of potentially liquefiable sand deposits using gravel drains. Journal of Geotechnical and Geoenvironmental Engineering, 103(ASCE 13050).

Seed, H. B., and Idriss, I. M. (1971). Simplified procedure for evaluating soil liquefaction potential. Journal of Soil Mechanics and Foundations Div.

Shahir, H., Pak, A., Taiebat, M., and Jeremić, B. (2012). Evaluation of variation of permeability in liquefiable soil under earthquake loading. Computers and Geotechnics, 40, 74-88. https://doi.org/10.1016/j.compgeo.2011.10.003

Shamoto, Y., Zhang, J. M., and Tokimatsu, K. (1998). Methods for evaluating residual post-liquefaction ground settlement and horizontal displacement. Soils and Foundations, 38, 69-83. https://doi.org/10.3208/sandf.38.Special_69

Sonmez, H., and Gokceoglu, C. (2005). A liquefaction severity index suggested for engineering practice. Environmental Geology, 48 (1), 81-91. https://doi.org/10.1007/s00254-005-1263-9

Stewart, J. P. (2008). Benchmarking of nonlinear geotechnical ground response analysis procedures. Pacific Earthquake Engineering Research Center.

Sugito, M., Oka, F., Yashima, A., Furumoto, Y., and Yamada, K. (2000). Time-dependent ground motion amplification characteristics at reclaimed land after the 1995 Hyogoken Nambu Earthquake. In Developments in geotechnical engineering (Vol. 84, pp. 145-

158). Elsevier. https://doi.org/10.1016/S0013-7952(99)00139-8.

Taiebat, M., Shahir, H., and Pak, A. (2007). Study of pore pressure variation during liquefaction using two constitutive models for sand. Soil Dynamics and Earthquake Engineering, 27 (1), 60-72. https://doi.org/10.1016/j.soildyn.2006.03.004

Takemura, J., Okamura, M., Igarashi, R., Masuda, M., and Izawa, J. (2009). Centrifuge model tests on soil desaturation as a liquefaction countermeasure. Proc. 17 ICSMGE, Alexandria.

Takemura, J., Kondoh, M., Esaki, T., Kouda, M., and Kusakabe, O. (1999). Centrifuge model tests on double propped wall excavation in soft clay. Soils and Foundations, 39(3), 75-87. https://doi.org/10.3208/sandf.39.3_75.

Tsukamoto, Y., Ishihara, K., Umeda, K., and Enomoto, T. (2006). Cyclic resistance of clean sand improved by silicate-based permeation grouting. Soils and foundations, 46(2), 233-245. https://doi.org/10.3208/sandf.46.233

Tatsuoka, F., Muramatsu, M., and Sasaki, T. (1982). Cyclic undrained stress-strain behavior of dense sands by torsional simple shear test. Soils and Foundations, 22(2), 55-70. https://doi.org/10.3208/sandf1972.22.2_55

Thevanayagam, S., and Martin, G. R. (2002). Liquefaction in silty soils—screening and remediation issues. Soil Dynamics and Earthquake Engineering, 22(9-12), 1035-1042.

Tokimatsu, K., Tamura, S., Suzuki, H., and Katsumata, K. (2012). Building damage associated with geotechnical problems in the 2011 Tohoku Pacific Earthquake. Soils and Foundations, 52(5), 956-974. https://doi.org/10.1016/j.sandf.2012.11.014.

Tokimatsu, K., Yoshimi, Y., and Ariizumi, K. (1990). Evaluation of liquefaction resistance of sand improved by deep vibratory compaction. Soils and Foundations, 30(3), 153-158. https://doi.org/10.3208/sandf1972.30.3_153.

Tokimatsu, K., and Katsumata, K. (2012). Liquefaction-induced damage to buildings in Urayasu city during the 2011 Tohoku Pacific earthquake. In Proceedings of the International Symposium on Engineering Lessons Learned from the 2011 Great East Japan Earthquake, 665-674.

Tokimatsu, K., and Seed, H. B. (1987). Evaluation of settlements in sands due to earthquake shaking. Journal of geotechnical engineering, 113(8), 861-878. https://doi.org/10.1061/(ASCE)0733-9410(1987)113:8(861)

Tokimatsu, K., Yoshimi, Y., and Ariizumi, K. (1990). Evaluation of liquefaction resistance of sand improved by deep vibratory compaction. Soils and Foundations, 30(3), 153-158. https://doi.org/10.3208/sandf1972.30.3_153

Unno, T., Kazama, M., Uzuoka, R., and Sento, N. (2008). Liquefaction of unsaturated sand considering the pore air pressure and volume compressibility of the soil particle skeleton. Soils and Foundations, 48(1), 87-99. https://doi.org/10.3208/sandf.48.87.

Van Genuchten, M. T. (1980). A closed‐form equation for predicting the hydraulic conductivity of unsaturated soils. Soil science society of America journal, 44(5), 892-898.

Vanmarcke, E. (2010). Random fields: analysis and synthesis. World Scientific.

Wang, B., Zen, K., Chen, G. Q., Zhang, Y. B., and Kasama, K. (2013). Excess pore pressure dissipation and solidification after liquefaction of saturated sand deposits. Soil Dynamics and Earthquake Engineering, 49, 157-164.. https://doi.org/10.1016/j.soildyn.2013.02.018.

White, D. J., Take, W. A., and Bolton, M. D. (2003). Soil deformation measurement using particle image velocimetry (PIV) and photogrammetry. Geotechnique, 53 (7), 619-631. https://doi.org/10.1680/geot.2003.53.7.619

Yamaguchi, A., Mori, T., Kazama, M., and Yoshida, N. (2012). Liquefaction in Tohoku district during the 2011 off the Pacific Coast of Tohoku Earthquake. Soils and Foundations 52 (5), 811-829. https://doi.org/10.1016/j.sandf.2012.11.005

Yang Z. (2000). Numerical Modeling of Earthquake Site Response Including Dilation and Liquefaction, PhD Thesis, Dept. of Civil Engineering and Engineering Mechanics, Columbia University, NY, New York.

Yang, Z., Elgamal, A., and Parra, E. (2003). Computational model for cyclic mobility and associated shear deformation. Journal of Geotechnical and Geoenvironmental Engineering, 129(12), 1119-1127. https://doi.org/10.1061/(ASCE)1090-0241(2003)129:12(1119)

Yegian, M. K., Eseller-Bayat, E., Alshawabkeh, A., and Ali, S. (2007). Induced-partial saturation for liquefaction mitigation: experimental investigation. Journal of geotechnical and geoenvironmental engineering, 133(4), 372-380. https://doi.org/10.1061/(ASCE)1090-0241(2007)133:4(372).

Yoshimi, Y., Tanaka, K., and Tokimatsu, K. (1989). Liquefaction resistance of a partially saturated sand. Soils and foundations, 29(3), 157-162. https://doi.org/10.3208/sandf1972.29.3_157.

Yoshimi, Y., and Tokimatsu, K. (1977). Settlement of buildings on saturated sand during earthquakes. Soils and Foundations, 17(1), 23-38.

Yoshimi, Y., and Tokimatsu, K. (1977). Settlement of buildings on saturated sand during earthquakes. Soils Found., 17 (1), 23–38. https://doi.org/10.3208/sandf1972.17.23

Zeghal, M., Elgamal, A. W., Zeng, X., and Arulmoli, K. (1999). Mechanism of liquefaction response in sand–silt dynamic centrifuge tests. Soil Dynamics and Earthquake Engineering, 18(1), 71-85. https://doi.org/10.1016/S0267-7261(98)00029-3.

Zeybek, A., and Madabhushi, S. P. G. (2017). Influence of air injection on the liquefaction-induced deformation mechanisms beneath shallow foundations. Soil Dynamics and Earthquake Engineering, 97, 266-276. https://doi.org/10.1016/j.soildyn.2017.03.018.

Zhang, J. M., and Wang, G. (2012). Large post-liquefaction deformation of sand, part I: physical mechanism, constitutive description and numerical algorithm. Acta Geotechnica, 7(2), 69-113. https://doi.org/10.1007/s11440-011-0150-7

Zhang, J., Zhang, L. M., and Tang, W. H. (2009). Bayesian framework for characterizing geotechnical model uncertainty. Journal of Geotechnical and Geoenvironmental Engineering, 135(7), 932-940. https://doi.org/10.1061/(ASCE)GT.1943-5606.0000018

Zhang, L. L., Zhang, L. M., and Tang, W. H. (2008). Similarity of soil variability in centrifuge models. Canadian Geotechnical Journal, 45 (8), 1118-1129. https://doi.org/10.1139/T08-066